

# Modeling the Frequency Response of the Graphene/Electrolyte Interface in Electrochemical Systems

by

Mahdi Yavarian

A thesis  
presented to the University of Waterloo  
in fulfillment of the  
thesis requirement for the degree of  
Doctor of Philosophy  
in  
Applied Mathematics

Waterloo, Ontario, Canada, 2025

© Mahdi Yavarian 2025

## Examining Committee Membership

The following served on the Examining Committee for this thesis. The decision of the Examining Committee is by majority vote.

External Examiner: Björn Birnir  
Professor, Department of Mathematics  
University of California, Santa Barbara

Supervisor(s): Zoran Mišković  
Professor, Department of Applied Mathematics  
University of Waterloo

Roderick Melnik  
Professor, Department of Mathematics  
Wilfrid Laurier University

Internal Member: Brian Ingalls  
Professor, Department of Applied Mathematics  
University of Waterloo

Matthew Scott  
Associate Professor, Department of Applied Mathematics  
University of Waterloo

Internal-External Member: Michael Pope  
Associate Professor, Department of Chemical Engineering  
University of Waterloo

### **Author's Declaration**

I hereby declare that I am the sole author of this thesis. This is a true copy of the thesis, including any required final revisions, as accepted by my examiners.

I understand that my thesis may be made electronically available to the public.

## Abstract

The graphene/electrolyte interface plays a central role in applications such as supercapacitors and biosensors. Traditionally modeled as two capacitors in series—the Debye capacitance of the electrolyte and the quantum capacitance of graphene—the interface is predominantly governed by the latter. While prior studies have focused on graphene’s voltage-dependent capacitance, its frequency response remains underexplored theoretically. This thesis develops a rigorous mathematical framework to model and analyze the frequency response of the graphene/electrolyte interface under diverse conditions, including finite-conductivity neutral graphene, charged graphene with infinite conductivity, and systems with room-temperature ionic liquids (RTILs).

We first examine a graphene electrode in a dilute electrolyte under small AC voltages. By linearizing and normalizing the Poisson–Nernst–Planck (PNP) equations, we derive analytical impedance expressions for graphene-metal and metal-metal systems, elucidating the role of quantum capacitance across electrolyte concentrations. For finite-sized graphene disk electrodes, we incorporate graphene’s intrinsic conductivity to obtain explicit quantum impedance expressions. The results reveal a transition from Warburg-type behavior at high frequencies to RC-circuit behavior at low frequencies, governed by quantum capacitance and conductivity.

The analysis extends to charged graphene electrodes under DC bias, using matched asymptotic expansions in the thin double-layer limit. We derive an analytical impedance expression that highlights the dependence of frequency response on ion concentration and bias voltage. Finally, we explore concentrated electrolytes with RTILs, introducing a new length scale to capture electrostatic correlations and characterizing their impact on low-frequency impedance.

## Acknowledgements

*“If I have seen further than others, it is by standing on the shoulders of giants”* — Isaac Newton in a letter to Robert Hooke, 1675.

I would like to borrow this timeless quote and say to my supervisors,  
**Dr. Zoran Mišković** and **Dr. Roderick Melnik**:

*“If I have seen further than others, it is by standing on YOUR shoulders.”*  
Thank you for guiding me through an enjoyable and memorable academic journey—one that is truly beyond words to express.

I am sincerely grateful to my committee members, **Dr. Brian Ingalls** and **Dr. Matthew Scott**, for generously taking time out of their busy schedules to support my PhD program. I especially appreciate their thoughtful attention during my comprehensive exam and their continued encouragement throughout the process. I would also like to extend my special thanks to Dr. Brian Ingalls for kindly sharing his lecture notes during my PhD lecturing.

I would also like to thank **Dr. Björn Birnir** and **Dr. Michael Pope** for kindly agreeing to serve on my PhD committee and for taking the time to read this thesis given their demanding schedules. In particular, I am grateful to Dr. Pope for his insightful experimental perspectives, which helped shape this thesis into a stronger and more balanced work. I am also deeply thankful to Dr. Birnir for the considerable time he invested in carefully reviewing my thesis that improved its clarity and presentation.

My heartfelt thanks go to my family for their unwavering support, patience, and encouragement during my PhD journey. Their presence—even from afar—has meant the world to me, and I am deeply grateful for the strength and reassurance they have always provided. I am also thankful to my friends, whose companionship and encouragement helped me navigate the most challenging phases of this journey. Their kindness, humor, and presence brought balance and joy, and I feel fortunate to have shared this experience with them.

I am thankful to Canada for fostering an inspiring academic environment, where I have had the privilege to pursue my research. I gratefully acknowledge the financial support from the Natural Sciences and Engineering Research Council of Canada (NSERC), as well as the continued support from the Department of Applied Mathematics at the University of Waterloo through teaching assistantships and, most notably, the opportunity to engage as a lecturer—an experience that was deeply played a pivotal role in shaping my academic career.

Finally, I would like to express my deep appreciation to the broader research community working at the intersection of mathematical physics and electrochemistry. Their insightful contributions have shaped my understanding and guided the development of this thesis. This work would not have been possible without the solid foundation they have laid.

## **Dedication**

*To the lovers of mathematical physics, may your curiosity never wane*

# Table of Contents

Examining Committee	ii
Author's Declaration	iii
Abstract	iv
Acknowledgements	v
Dedication	vii
List of Figures	xi
List of Abbreviations	xvi
List of Symbols	xvii
<b>1 Introduction</b>	<b>1</b>
1.1 Motivation . . . . .	1
1.2 Outline of Thesis . . . . .	3
<b>2 Theoretical Background</b>	<b>4</b>
2.1 Introduction . . . . .	4
2.2 Quantum Capacitance of Graphene . . . . .	4

2.3	Boundary Modeling of the Graphene/Electrolyte Interface . . . . .	6
2.4	Poisson-Nernst-Planck (PNP) Systems . . . . .	7
2.4.1	PNP Model in Dilute Electrolytes . . . . .	8
2.4.2	PNP Model in Ionic Liquids . . . . .	9
2.4.3	PNP Model in Linear Regime . . . . .	13
2.5	Method of Matched Asymptotic Expansions . . . . .	15
2.6	Fundamentals of the EIS . . . . .	18
<b>3</b>	<b>Neutral Graphene in Dilute Electrolytes</b>	<b>21</b>
3.1	Introduction . . . . .	21
3.2	Graphene with an Infinite Conductivity* . . . . .	22
3.2.1	PNP Model . . . . .	22
3.2.2	Impedance I . . . . .	25
3.3	Results and Discussion I . . . . .	26
3.4	Graphene with a Finite Conductivity* . . . . .	30
3.4.1	Model Description . . . . .	30
3.4.2	Graphene Disk Electrode . . . . .	32
3.4.3	Electrolyte Region . . . . .	38
3.4.4	Graphene/Electrolyte Interface . . . . .	41
3.4.5	Impedance II . . . . .	43
3.5	Results and Discussion II . . . . .	45
3.5.1	Frequency Response of the Graphene Disk Electrode . . . . .	45
3.5.2	Frequency Response of the Graphene/Electrolyte Interface . . . . .	48
3.6	Concluding Remarks . . . . .	56
<b>4</b>	<b>Charged Graphene in Dilute Electrolytes*</b>	<b>58</b>
4.1	Introduction . . . . .	58
4.2	Theory . . . . .	59

4.2.1	PNP Model . . . . .	61
4.2.2	Equilibrium Solution . . . . .	65
4.2.3	Linear dynamics . . . . .	71
4.2.4	Impedance . . . . .	80
4.3	Results and Discussion . . . . .	81
4.3.1	Equilibrium Analysis . . . . .	81
4.3.2	Frequency Response Analysis . . . . .	83
4.4	Concluding Remarks . . . . .	89
<b>5</b>	<b>Neutral Graphene in Ionic Liquids*</b>	<b>90</b>
5.1	Introduction . . . . .	90
5.2	Theory . . . . .	91
5.2.1	Asymptotic Matching . . . . .	95
5.2.2	Impedance . . . . .	101
5.3	Results and Discussion . . . . .	103
5.4	Concluding Remarks . . . . .	107
<b>6</b>	<b>Summary and Future Directions</b>	<b>108</b>
6.1	Summary . . . . .	108
6.2	Future Directions . . . . .	110
	<b>References</b>	<b>113</b>

# List of Figures

2.1	Illustration of Gauss's regions for the graphene/electrolyte interface. The EDL structure near the GE consists of the Stern layer and the diffuse layer, with constant permittivities $\epsilon_S$ and $\epsilon_b$ , respectively. Gaussian regions are shown at two locations: a pillbox enclosing the interface of the graphene electrode (GE) at $X = 0$ , with electric field $E_g$ ; and the other as a semi-infinite column (or very long slab) extending from $X = d$ into the bulk region of the diffuse layer, where the electrolyte is neutral and the electric field vanishes. . . . .	6
2.2	Schematic illustration of an ionic liquid confined between two electrodes, used to depict the concept of the packing parameter $\gamma$ . Red and blue spheres represent anions and cations, respectively, while unoccupied sites indicate voids in the lattice. In these 2D representations, the left panel corresponds to a fully packed configuration with $\gamma = 1$ , whereas the right panel shows a less densely packed state with $\gamma = 3/4$ . Picture adapted from [65]. . . . .	11
2.3	Circuit equivalence of a typical electrochemical process at the electrode/electrolyte interface. The faradiac reactions and heterogeneous effects are represented by the circuit elements $Z_f$ and CPE. The bulk resistance is shown by $\mathcal{R}_b$ . . . . .	19

3.1	Schematic diagram depicting the electrostatic potential $\Phi(X, \tau)$ as a function of the spatial coordinate $X$ , alongside electron energy levels and their corresponding equivalent capacitors. The quantities $\varepsilon_F(\tau)$ and $\varepsilon_D(\tau) = -e\Phi(0, \tau) = -e\Phi_0(\tau)$ represent the time-dependent Fermi energy and the Dirac point of graphene, respectively. Also illustrated are the potential differences occurring within the graphene layer at $X = 0$ , which are responsible for its doping, expressed as $V_q(\tau) = \Phi_0(\tau) + \varepsilon_F(\tau)/e$ , as well as the potential drop $V_d(\tau)$ across the diffuse layers adjacent to both the graphene and metal electrodes. The term $\mathcal{C}_q$ denotes the quantum capacitance of graphene at equilibrium located at $X = 0$ , while $\mathcal{C}_D$ refers to the Debye capacitance. . .	23
3.2	Illustration of the Nyquist Plot for different ion concentrations with the electrolyte thickness of $L = 1 \mu\text{m}$ . The solid lines refer to the GM electrode pair, and the dashed lines refer to the MM electrode pair. . . . .	27
3.3	Bode. (a) Illustration of the Bode phase plot for different concentrations with the electrolyte thickness of $L = 1 \mu\text{m}$ . The solid lines refer to the GM electrode pair, and the dashed lines refer to the MM electrode pair. (b) Illustration of Bode magnitude plot for different concentrations with the electrolyte thickness of $L = 1 \mu\text{m}$ . The solid lines refer to the GM electrode pair, and the dashed lines refer to the MM electrode pair. . . . .	28
3.4	Illustration of the capacitive Nyquist Plot for different concentrations with the electrolyte thickness of $L = 1 \mu\text{m}$ . The solid lines refer to the GM electrode pair, and the dashed lines refer to the MM electrode pair. The inset magnifies the capacitive behavior in high-frequency regime. . . . .	29
3.5	A schematic diagram of the proposed electrochemical cell flanked by the GE at $X = 0$ and the grounded ME at $X = L$ . The dependence on the position $X$ of the surface average of the electrostatic potential in the electrolyte, $\bar{\Phi}(X, \tau)$ , when the system is subject to a time-dependent voltage, $V_a(\tau)$ , is shown with $V_c(\tau)$ being the potential drop around the edge of the GE and $V_d(\tau)$ denoting the potential drop across the diffuse layer in the electrolyte. The external circuitry is represented by the contact resistance, $\mathcal{R}_c$ , and the contact current $I_c(\tau)$ passing through $\mathcal{R}_c$ . . . . .	31
3.6	Schematic of the graphene disk electrode. The Al wire provides electrical contact, while an insulating film limits electrolyte access to a defined central window. The exposed graphene (ungated area) serves as the electrochemically active surface. Picture adapted from [93]. . . . .	32

3.7	Frequency response of the graphene disk electrode. (a) Impedance Nyquist plot. The dashed curve corresponds to the low-frequency limit, representing capacitive (RC) behavior, while the dotted curve illustrates the high-frequency Warburg response. (b) Phase angle of the graphene disk impedance as a function of frequency. (c) Nyquist plot of the normalized complex capacitance. The dashed semicircle denotes the RC-like response in the low-frequency regime, as characterized by Bueno <i>et al.</i> , while the dotted line represents the high-frequency Warburg behavior. (d) Time-domain response of the surface-averaged potential drop across graphene to a step-like input. The dashed curve captures the long-time dynamics consistent with low-frequency RC-circuit behavior, whereas the dotted curve depicts the early-time response associated with high-frequency Warburg behavior. . . .	47
3.8	Effects of ion concentration on the frequency response of the GE/electrolyte interface when $a = 1$ mm and $R_c = 0$ . Solid curves represent finite graphene conductivity, while dashed curves indicate infinite conductivity. (a) Impedance Nyquist plot. (b, c) Bode plots. (d) Capacitive Nyquist plot. The bullet points in (a) and (d), together with the shaded areas in (b) and (c), indicate the cut-off frequency $\hat{\omega}_c$ below which EIS and ECS are applicable. . . . .	51
3.9	Effects of electrode area on the frequency response of the GE/electrolyte interface when $c_b = 10^{-2}$ M and $R_c = 0$ . Solid curves represent finite graphene conductivity, while dashed curves indicate infinite conductivity. (a) Impedance Nyquist plot. (b, c) Bode plots. (d) Capacitive Nyquist plot. The bullet points in (a) and (d) along with the shaded area in (b, c) refer to the cut-off frequency $\hat{\omega}_c$ below which the EIS and ECS are applicable. .	53
3.10	Effects of contact resistance on the frequency response of the GE/electrolyte interface when $c_b = 10^{-2}$ M and $a = 1$ mm. Solid curves represent finite graphene conductivity, while dashed curves indicate infinite conductivity. (a) Impedance Nyquist plot. (b, c) Bode plots. (d) Capacitive Nyquist plot. The bullet points in (a) and (d) along with the shaded area in (b, c) refer to the cut-off frequency $\hat{\omega}_c$ below which the EIS and ECS are applicable. .	55

4.1	Schematic representation of the electrochemical cell comprising the graphene electrode (GE) and the metal electrode (ME), with the electrolyte confined between two outer Helmholtz planes (OHPs) positioned near each electrode. In response to a time-dependent applied voltage $V(\tau)$ , the resulting electrostatic potential distribution $\Phi(X, \tau)$ is shown, including the internal potential drop $V_q(\tau)$ associated with the doping of graphene. The potential decreases linearly across the Stern layers, which extend from each electrode surface to its respective OHP, producing the potential drops labeled as $V_S^g(\tau)$ and $V_S^m(\tau)$ for the GE and ME sides, respectively. Beyond the Stern layers, the potential continues to decay through the neighboring diffuse layers until it reaches a uniform value in the bulk electrolyte. The potential drops across these diffuse regions are denoted by $V_d^g(\tau)$ and $V_d^m(\tau)$ . . . . .	60
4.2	The equilibrium behavior of the system's total capacitance as a function of voltage, for varying ion concentrations $c_b$ and scaled Stern layer thicknesses $\hat{\alpha}$ .	82
4.3	Frequency response of the graphene-based electrochemical cell. Left panels: (a) magnitude and (b) phase angle as functions of frequency for various ion concentrations $c_b$ and Stern layer thicknesses $\hat{\alpha}$ , with the applied voltage fixed at $V = 0.2$ V. Right panels: (c) magnitude and (d) phase angle plotted against frequency for different applied voltages and Stern layer thicknesses $\hat{\alpha}$ , with the ion concentration set to $c_b = 10^{-3}$ M. . . . .	85
4.4	The phase sensitivity of the proposed graphene-based electrochemical cell <i>vs</i> ion concentration. (a) The variations of the phase sensitivity for different values of the bias voltage and the Stern thickness when the reference ion concentration and the operating frequency are set to $c_{\text{ref}} = 10^{-3}$ M and $\hat{\omega} = 10^{-3}$ . (b) The variations of the phase sensitivity for different values of the reference ion concentration and the Stern thickness, when $V = 0.2$ V and $\hat{\omega} = 10^{-3}$ . (c) The variations of the phase sensitivity for different values of the operating frequency and the Stern thickness when $c_{\text{ref}} = 10^{-3}$ M and $V = 0.2$ V. . . . .	88

5.1	Impact of the electrostatic correlation length $\delta_c$ on the structure of the electric double layer (EDL). (a) Variations of the normalized leading-order inner potential drop, $\tilde{\Psi}_0$ , as a function of the rescaled inner coordinate $\zeta = (L + X)/\lambda_D$ for the GM electrode pair. (b) Variations of the normalized leading-order inner potential drop, $\tilde{\Psi}_0$ , as a function of the rescaled inner coordinate $\zeta = (L + X)/\lambda_D$ for the MM electrode pair. (c) Variations of the total scaled capacitance, $C(\delta_c)$ , and the scaled EDL capacitance, $C_d(\delta_c)$ (inset), as functions of $\delta_c$ . . . . .	105
5.2	Impact of the electrostatic correlation length $\delta_c$ on the frequency response. (a) Variations of the phase response for different values of $\delta_c$ . (b) Variations of the magnitude response for different values of $\delta_c$ . . . . .	106

# List of Abbreviations

AC	Alternating current
DC	Direct current
EIS	electrochemical impedance spectroscopy
ECS	electrochemical capacitive spectroscopy
EDL	Electric double-layer
PNP	Poisson–Nernst–Planck
GE	Graphene electrode
ME	Metal electrode
GM	Graphene–metal
MM	Metal–metal
CPE	Constant phase element
IL	Ionic liquid
BSK	Bazant–Storey–Kornyshev
OHP	Outer Helmholtz plane
QRT	Quantum rate theory

# List of Symbols

$k_B$	Boltzmann constant	J/K
$T$	temperature	K
$\hbar$	reduced Planck's constant	J.sec
$u_F$	Fermi velocity	m/sec
$C_{\pm}$	concentration of positive and negative ions	M
$c_b$	bulk concentration	M
$F_{\pm}$	flux density	mol cm <sup>-2</sup> sec <sup>-1</sup>
$D$	diffusion coefficient	cm <sup>2</sup> /sec
$D_q$	diffusion coefficient of graphene	cm <sup>2</sup> /sec
$z$	valency	none
$e$	electron charge	C
$n$	surface number density of graphene	nm <sup>-2</sup>
$n_g$	characteristic density of graphene	nm <sup>-2</sup>
$n_d$	characteristic density in a semi-infinite diffuse layer	nm <sup>-2</sup>
$\mu_q$	chemical potential inside graphene	eV
$\mu$	ion mobility	cm <sup>2</sup> V <sup>-1</sup> sec <sup>-1</sup>
$V_q$	potential drop inside graphene	V
$V_d$	potential drop inside the diffuse layer	V
$V_a$	total applied potential	V
$V_c$	potential at the circumference of graphene	V
$V_S^g$	potential drop across the Stern layer adjacent to the GE	V
$V_S^m$	potential drop across the Stern layer adjacent to the ME	V
$V_{el}$	potential drop across the electrolyte region occupied by the ions	V
$v_q$	normalized potential drop inside graphene	none
$v_d$	normalized potential drop inside the diffuse layer	none
$v_a$	normalized total applied potential	none
$v_g$	normalized potential drop across the EDL adjacent to the GE	none

$v_m$	normalized potential drop across the EDL adjacent to the ME	none
$\Phi$	electrostatic potential	V
$\phi$	normalized electrostatic potential	none
$\phi_g$	normalized potential distribution across the GE	none
$\phi_m$	normalized potential distribution across the ME	none
$\psi_g$	normalized excess potential of the GE relative to the bulk	none
$\psi_m$	normalized excess potential of the ME relative to the bulk	none
$C_q$	quantum capacitance of graphene	$\mu\text{F}/\text{cm}^2$
$C_D$	Debye capacitance	$\mu\text{F}/\text{cm}^2$
$C_{DL}$	double-layer capacitance	$\mu\text{F}/\text{cm}^2$
$C_Q$	total quantum capacitance of a neutral GE	$\mu\text{F}$
$C_q$	normalized quantum capacitance of graphene	none
$C_{DL}$	normalized double-layer capacitance	none
$\Gamma$	Debye capacitance to quantum capacitance ratio	none
$\tau$	time	sec
$\tau_D$	Debye time	sec
$\tau_H$	diffusion time scale	sec
$\tau_c$	charging time	sec
$\tau_q$	quantum time scale	sec
$t$	normalized time	none
$\Omega$	angular frequency	$\text{sec}^{-1}$
$\Omega_c$	cut-off frequency	$\text{sec}^{-1}$
$\omega$	normalized frequency	none
$\omega_c$	normalized cut-off frequency	none
$\omega_q$	dimensionless quantum frequency	none
$s$	frequency variable	none
$S$	Laplace frequency variable	$\text{sec}^{-1}$
$\epsilon_b$	bulk permittivity	F/m
$\epsilon_0$	vacuum permittivity	F/m
$\epsilon_S$	dielectric permittivity in the Stern layer	F/m
$\varepsilon$	small parameter	none
$L$	electrolyte thickness	$\mu\text{m}$ , mm
$\ell$	normalized electrolyte thickness	none
$L_c$	electrostatic correlation length	nm
$l_c$	dimensionless electrostatic correlation length	none
$\delta_c$	electrostatic correlation length ratio	none
$\lambda_D$	Debye length	nm
$\lambda_{1M}$	Debye length at $c_b = 1\text{M}$	

$l_D$	normalized Debye length	none
$\lambda_B$	Bjerrum length	nm
$\lambda_s$	effective Stern thickness	Å
$\alpha$	normalized Stern thickness	none
$\hat{\alpha}$	scaled Stern thickness	none
$\varrho$	charge density	C/m <sup>3</sup>
$\rho$	normalized charge density	none
$J$	total surface current	A/cm <sup>2</sup>
$J_c$	surface conduction current	A/cm <sup>2</sup>
$J_d$	surface displacement current	A/cm <sup>2</sup>
$J_{\text{lim}}$	diffusion-limiting current	A/cm <sup>2</sup>
$J_g$	diffusive current density of graphene	A/cm
$j$	normalized total surface current	none
$j_c$	normalized surface conduction current	none
$j_d$	normalized surface displacement current	none
$I_c$	total current at the edge of the graphene disk	A
$\mathcal{Z}_q$	quantum impedance	Ω
$\mathcal{R}_q$	quantum sheet resistance	Ω
$\mathcal{R}_c$	contact resistance	kΩ
$\mathcal{R}_b$	bulk resistance	Ω/cm <sup>2</sup>
$\sigma_0$	universal conductivity	μS, m/sec
$Z_q$	dimensionless quantum impedance	none
$\zeta$	characteristic frequency of surface impedance	nm <sup>-1</sup>
$K_q(S)$	response function	none
$\mathcal{K}_q$	quantum complex capacitance	μF/cm <sup>2</sup>
$\hat{K}_q$	normalized quantum complex capacitance	none
$K$	Hankel variable	nm <sup>-1</sup>
$k$	dimensionless Hankel variable	none
$Q_g$	total charge on the GE	C
$\eta$	quantum time scale to Debye time scale ratio	none
$S_{\hat{\phi}}$	angular phase sensitivity	none

# Chapter 1

## Introduction

### 1.1 Motivation

A central aspect of optimizing electrochemical systems lies in understanding the behavior of electrode/electrolyte interfaces [1, 2]. While traditional metal electrodes have long served as the default choice, their limitations in both biological and energy-related applications have motivated the exploration of alternative materials. Among these, graphene-based electrodes have garnered considerable attention due to their unique two-dimensional structure and exceptional electronic properties. Notably, the quantum capacitance of graphene plays a pivotal role in determining the total interfacial capacitance [1, 3], in sharp contrast to metal electrodes, where the electronic contribution to capacitance is typically negligible compared to the classical double-layer capacitance [3, 4].

Despite its growing prominence, the alternating current (AC) response of graphene/electrolyte interfaces remains largely underexplored, even though such information is vital for applications including biosensing and charge storage. To address this gap, techniques such as electrochemical impedance spectroscopy (EIS) and electrochemical capacitive spectroscopy (ECS) have become indispensable for analyzing interfacial dynamics in the frequency domain across a wide range of electrochemical systems [5, 6]. These techniques serve as powerful tools for probing frequency-dependent behaviors at interfaces [7, 8, 9, 10, 11].

By employing small-signal excitation [12, 13], EIS enables the decomposition of interfacial processes—such as double-layer charging, charge transfer, mass transport, and adsorption dynamics—across a broad frequency spectrum [5, 6]. This spectral resolution

provides key insights into underlying mechanisms and serves as a foundation for the design of high-performance sensors and diagnostic devices [5].

In biological applications, the need for minimally invasive and high-resolution probing has further highlighted the drawbacks of conventional metal electrodes. Electrodes made from materials like gold and platinum often exhibit poor impedance resolution, delayed signal response, and reduced sensitivity in biosensing contexts [14, 15, 16, 17, 18, 19, 20]. In contrast, graphene-based impedimetric biosensors demonstrate significantly enhanced signal strength. For instance, Wang *et al.* [21] reported a twofold improvement in signal intensity for cancer cell detection, while Song *et al.* [22] observed a sixfold increase in impedance sensitivity compared to gold electrodes.

Nevertheless, direct impedance measurements frequently suffer from low sensitivity and poor signal-to-noise ratios, especially when detecting weak biochemical interactions such as antigen–antibody binding. Efforts to improve sensitivity have focused on advanced surface functionalization and the integration of nanostructured materials. Among these, carbon-based materials—particularly graphene—have shown great promise due to their large surface area, excellent electrical conductivity, and inherent biocompatibility [23, 24]. These attributes make graphene an ideal candidate for label-free biosensing platforms and a valuable model system for studying capacitive electrochemical phenomena [2, 25].

Impedance characterization is also crucial in therapeutic and physiological modeling applications. In neural stimulation and electrophysiological monitoring, the impedance at the electrode–tissue interface must be carefully regulated to avoid localized heating and tissue damage. Conventional electrodes often suffer from high edge current densities, resulting in undesirable physiological effects [26]. Graphene electrodes offer a compelling alternative, thanks to their superior conductivity and effective current-spreading capabilities. Their mechanical flexibility and chemical stability further support long-term bioelectronic integration [27, 28, 29].

Beyond dilute electrolytes, recent research has expanded into highly concentrated systems such as ionic liquids (ILs), which possess distinctive properties including high ionic strength, negligible volatility, and broad electrochemical stability windows. These features make ILs promising for next-generation energy storage and sensing technologies [30, 31, 32, 33, 34, 35, 36]. The integration of ILs with carbon-based electrodes—particularly graphene—has become a focal point in supercapacitor development and ion-conductive membranes [37, 38, 39, 40]. However, charge transport at the IL/electrode interface remains poorly understood due to the rich interplay of electrostatic correlations, ion crowding, and structural ordering in these dense media [41].

EIS has again proven invaluable for probing such complexities, especially at the graphene/IL interface [42, 43, 44]. Under static (DC) conditions, mean-field models describe the electric double layer in ILs via phenomena such as overscreening—arising from electrostatic correlations—and crowding—due to finite ion sizes [45]. These models often assume semi-infinite domains and thereby fail to account for essential finite-size effects in practical devices [46, 47, 48, 49, 50]. A rigorous investigation of the dynamic charge response in finite-length electrochemical cells containing ILs thus remains a pressing challenge with significant theoretical and technological implications.

## 1.2 Outline of Thesis

The thesis is structured as follows:

Chapter 2 presents the theoretical background underlying the mathematical models developed throughout the thesis. This includes the derivation of the quantum capacitance of graphene with a brief discussion on how graphene/electrolyte interface is mathematically modeled. The chapter then discusses the Poisson–Nernst–Planck (PNP) systems for both dilute electrolytes and ionic liquids, along with their linearized forms. The chapter also introduces the method of matched asymptotic expansions, detailing the procedures employed in subsequent analyses.

Chapter 3 focuses on the frequency response of neutral graphene in dilute electrolytes, studied under two conditions: graphene with infinite conductivity and graphene with finite conductivity. In both cases, the system is subjected to a small AC voltage, and the analysis is based on the linearized PNP framework.

Chapter 4 investigates the frequency response of charged graphene in dilute electrolytes, where the system is subjected to a DC voltage superimposed with a small AC perturbation. The analysis is based on the full nonlinear PNP system and is approached using the method of matched asymptotic expansions.

Chapter 5, explores the frequency response of neutral graphene interfaced with an ionic liquid under a small AC voltage modulation. The governing equations are given by the linearized PNP model for ionic liquids where the Poisson equation is generalized to the Bazant, Storey and Kornyshev equation [45], and the analysis is carried out via matched asymptotic expansions.

Chapter 6, provides the summary of the thesis together with the possible future directions.

# Chapter 2

## Theoretical Background

### 2.1 Introduction

The theoretical foundations of this thesis are structured as follows. In the first section, the quantum capacitance of graphene, as one of its intrinsic electronic properties, is derived. Then, as a common theoretical ingredient to all subsequent chapters, we discuss how a graphene electrode is modeled when interfaced with an electrolyte through the application of the Gauss' law. Given that graphene is in contact with an electrolyte, the charge transport within the electrolyte plays a pivotal role. This motivates to introduce the Poisson–Nernst–Planck (PNP) model as the governing framework for ionic dynamics. The chapter concludes with the motivation of the method of matched asymptotic expansions—an essential asymptotic technique employed for analytical treatment of time-dependent problems involving diffuse-charge dynamics in finite electrochemical systems.

### 2.2 Quantum Capacitance of Graphene

The number density of charge carriers in doped monolayer graphene is given by [51]

$$n(\mu_q) = \int_{-\infty}^{\infty} d\varepsilon \mathcal{D}(\varepsilon) \left[ \frac{1}{1 + e^{\beta(\varepsilon - \mu_q)}} - \frac{1}{1 + e^{\beta\varepsilon}} \right], \quad (2.1)$$

where  $\varepsilon$  denotes the electron energy,  $\mathcal{D}(\varepsilon)$  is the density of states (DOS) in the  $\pi$  electronic bands of graphene, and  $\mu_q = eV_q$  represents the chemical potential across graphene which

controls the number density  $n$  with  $V_q$  being the potential drop inside graphene and  $e > 0$  is the elementary charge. Also,  $\beta = 1/(k_B T)$ , with  $k_B$  being the Boltzmann constant and  $T$  the temperature. For typical doping levels encountered in graphene-based devices, the chemical potential satisfies  $|\mu_q| \lesssim 1$  eV. In this regime, a linear approximation for the DOS is valid, and we adopt  $\mathcal{D}(\varepsilon) \approx 2|\varepsilon|/[\pi(\hbar u_F)^2]$  where  $u_F \approx 10^6$  m/s is the Fermi velocity in graphene and  $\varepsilon = 0$  corresponds to the Dirac point in the  $\pi$ -electron band structure [51]. The surface charge density of graphene,  $\sigma_g$ , is related to the carrier density via  $\sigma_g = -en(\mu_q)$ . The quantum capacitance is then defined by the differential relation  $\mathcal{C}_q = -\frac{d\sigma_g}{dV_q} = e^2 \frac{dn}{d\mu_q}$ . Alternatively, the quantum capacitance can be interpreted through the Thomas–Fermi screening length as  $\mathcal{C}_q = k_{\text{TF}}/2\pi$  where  $k_{\text{TF}}$  denotes the inverse Thomas–Fermi length, characterizing the screening due to the polarizability of the electron–hole system in graphene [52].

Introducing the Fermi–Dirac distribution,  $f(\varepsilon, \mu_q, \beta) = 1/(1 + e^{\beta(\varepsilon - \mu_q)})$  and using  $\partial f/\partial \mu_q = -\partial f/\partial \varepsilon$ , we can write the quantum capacitance as

$$\mathcal{C}_q = e^2 \int_{-\infty}^{\infty} \mathcal{D}(\varepsilon) \left( -\frac{\partial f(\varepsilon, \mu_q, \beta)}{\partial \varepsilon} \right) d\varepsilon. \quad (2.2)$$

Integrating by parts, we obtain

$$\mathcal{C}_q = e^2 \int_{-\infty}^{\infty} f(\varepsilon, \mu_q, \beta) \frac{d\mathcal{D}(\varepsilon)}{d\varepsilon} d\varepsilon, \quad (2.3)$$

which, after substituting the linear DOS, evaluates to

$$\mathcal{C}_q = \frac{2e^2}{\pi\beta(\hbar u_F)^2} [\ln(1 + e^{\beta\mu_q}) + \ln(1 + e^{-\beta\mu_q})]. \quad (2.4)$$

Substituting back  $\beta = 1/(k_B T)$ , the final expression becomes

$$\mathcal{C}_q = \frac{4e^2 k_B T}{\pi(\hbar u_F)^2} \ln \left[ 2 \cosh \left( \frac{eV_q}{2k_B T} \right) \right], \quad (2.5)$$

which describes the quantum capacitance of a spatially homogeneous, monolayer graphene sheet. It is worth mentioning that when  $V_q = 0$ , Eq. (2.5) reduces to  $\mathcal{C}_q = 4e^2 k_B T \ln 2 / [\pi(\hbar u_F)^2]$  which is the quantum capacitance of the neutral graphene at finite temperature. At room temperature, this capacitance takes the value  $\mathcal{C}_q \approx 0.8 \mu\text{F}/\text{cm}^2$  [51].

The above expressions are also applicable under quasi-equilibrium conditions, i.e., for processes occurring at the time scales that are much slower than the electronic relaxation time scale due to electron–electron interactions in graphene.

## 2.3 Boundary Modeling of the Graphene/Electrolyte Interface

When immersed in an electrolyte, the graphene electrode is modeled by its surface charge density, which is governed by its intrinsic electronic properties. Given that graphene is chemically inert and hydrophobic, we shall neglect any specific ion adsorption on its surface<sup>1</sup> and thereby neglect any electron transfer to/from graphene. In that respect, graphene is described as an ideally polarizable electrode that blocks any Faradaic current on its surface. A fundamental component common to all subsequent chapters of this thesis is the relationship between the surface charge density of the graphene electrode and the electrostatic potential within the electrolyte. This relation enables us to formulate the electrostatic boundary condition imposed at the graphene surface.

Figure 2.1 is a one-dimensional zoom-in schematic view of the graphene/electrolyte interface with graphene located at  $X = 0$ . Upon applying an external voltage, the graphene electrode (GE) becomes charged. This excess charge causes the counterions in the electrolyte to migrate toward the surface of the GE to neutralize it. Upon approaching the GE, the counterions are separated from the GE by a layer of solvent molecules and are subsequently distributed into the region known as the *diffuse layer*, which extends far enough from the GE where the electrostatic effects are negligible. The region closest to the GE contains no net charge and is referred to as the *Stern layer* which, according to

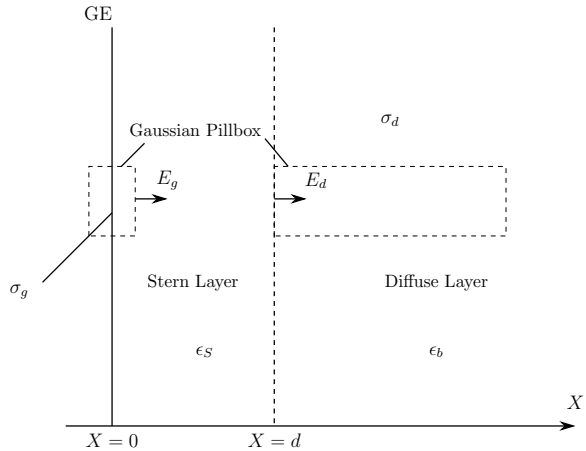


**Figure 2.1:** Illustration of Gauss’s regions for the graphene/electrolyte interface. The EDL structure near the GE consists of the Stern layer and the diffuse layer, with constant permittivities  $\epsilon_S$  and  $\epsilon_b$ , respectively. Gaussian regions are shown at two locations: a pillbox enclosing the interface of the graphene electrode (GE) at  $X = 0$ , with electric field  $E_g$ ; and the other as a semi-infinite column (or very long slab) extending from  $X = d$  into the bulk region of the diffuse layer, where the electrolyte is neutral and the electric field vanishes.

<sup>1</sup>In this model, we idealize graphene as pristine and defect-free, and consider a neutral equilibrium system with only bulk properties included, while interfacial effects are neglected under the assumption of small, weakly interacting ions.

Figure 2.1, is separated from the diffuse layer at  $X = d$ . Together, the Stern layer and the diffuse layer constitute a layer of electrolyte called the *electric double layer* (EDL).

Referring to Fig. 2.1, let the dielectric permittivities of the Stern layer and diffuse layer be denoted by  $\epsilon_S$  and  $\epsilon_b$ , respectively. The electric field induced at the GE is represented by  $E_g$  and the electric field at  $X = d$  is shown by  $E_d$ . Assuming no ion adsorption occurs at  $X = d$ , Gauss's law can be applied to a pillbox-shaped Gaussian surface around the GE at  $X = 0$  and the column of the electrolyte extending from  $X = d$  into the bulk, where electrolyte is neutral and the electric field is zero, yielding the following relations

$$\begin{aligned}\epsilon_S E_g &= \sigma_g, \\ -\epsilon_b E_d &= \sigma_d.\end{aligned}\tag{2.6}$$

In Eq. (2.6),  $\sigma_g$  is the surface charge density of GE and  $\sigma_d$  is the effective surface charge density in the diffuse layer. Recalling that the Stern layer is free of charge, so that electric field is constant in the region  $X \in (0, d)$  and invoking the continuity of the electric displacement field across the interface at  $X = d$ , i.e.,  $\epsilon_S E_g = \epsilon_b E_d$ , we may add both sides of equations in Eq. (2.6), which gives the charge neutrality adjacent to the GE as

$$\sigma_g + \sigma_d = 0.\tag{2.7}$$

## 2.4 Poisson-Nernst-Planck (PNP) Systems

The general description of ion transport is based on the Nernst–Planck (NP) equation describing the mass conservation of ionic species which incorporates the effects of both concentration gradients and electric fields on ionic flux. For a symmetric monovalent binary solution containing two ion species, the NP equation is [53]

$$\frac{\partial C_{\pm}}{\partial \tau} + u \nabla C_{\pm} = -\nabla \cdot \mathbf{F}_{\pm},\tag{2.8}$$

where  $C_{\pm}$  is the concentration of positive and negative ions,  $\mathbf{F}_{\pm}$  is the vector flux density of ions, and  $u$  is the drift velocity in the convection term  $u \nabla C_{\pm}$ . The ionic flux density, assuming equal mobilities,  $M_+ = M_- = M$ , is given by [53]

$$\mathbf{F}_{\pm} = -MC_{\pm} \nabla \mu_{\pm},\tag{2.9}$$

where  $\mu_{\pm}$  is the electrochemical potential of each ion species obtained by taking the functional derivative of the free energy  $G$  with respect to the ion concentrations, i.e., [53]

$$\mu_{\pm} = \frac{\delta G}{\delta C_{\pm}}.\tag{2.10}$$

The mobility of ions assuming equal diffusion coefficients,  $D_+ = D_- = D$ , is obtained by Einstein's relation [53]

$$M = \frac{eD}{k_B T}. \quad (2.11)$$

### 2.4.1 PNP Model in Dilute Electrolytes

The free energy functional for a dilute electrolyte is given by [54]

$$G[C_{\pm}, \Phi] = \int_V d\mathbf{r} \left( g(C_+, C_-) + \varrho(C_+, C_-) \Phi - \frac{\epsilon_b}{2} |\nabla \Phi|^2 \right), \quad (2.12)$$

where  $\varrho(C_+, C_-) = e(C_+ - C_-)$  is the charge density,  $\Phi$  is the electrostatic potential,  $\epsilon_b$  is the permittivity of the electrolyte, and  $g(C_+, C_-)$  is the entropic contribution of the mobile ions given by [54]

$$g(C_+, C_-) = k_B T (C_+ \ln C_+ - C_+ + C_- \ln C_- - C_-). \quad (2.13)$$

Taking the functional derivative of  $G$  with respect to  $C_{\pm}$ , yields the electrochemical potential for a dilute solution

$$\mu_{\pm}^{\text{dilute}} = \frac{\delta G}{\delta C_{\pm}} = k_B T \ln C_{\pm} \pm e\Phi. \quad (2.14)$$

By taking the gradient from Eq. (2.14) and then substituting into Eq. (2.9), using Eq. (2.11), gives the ionic flux in dilute solutions as

$$\mathbf{F}_{\pm} = -D \left( \nabla C_{\pm} \pm \frac{e}{k_B T} C_{\pm} \nabla \Phi \right). \quad (2.15)$$

In Eq. (2.15), the first term represents the ion diffusion and the second term represents the electromigration of the ions under the influence of the electrostatic field  $\Phi$ . Neglecting the ionic drift by setting  $u = 0$  in Eq. (2.8), substituting Eq. (2.15) into Eq. (2.8), we obtain the NP equation for dilute solutions

$$\frac{\partial C_{\pm}}{\partial \tau} = -\nabla \cdot \mathbf{F}_{\pm} = D \nabla \cdot \left( \nabla C_{\pm} \pm \frac{e}{k_B T} C_{\pm} \nabla \Phi \right). \quad (2.16)$$

In Eq. (2.16), the number of equations and variables do not match owing to the presence of the electric potential  $\Phi$  as an additional unknown. Hence, Eq. (2.16) does not form a

closed system of equations. The additional equation is introduced by finding the extremum of the free energy with respect to variations in the electrostatic potential, i.e.,  $\delta G/\delta\Phi = 0$ . This yields to the Poisson equation as

$$-\epsilon_b \nabla^2 \Phi = \varrho. \quad (2.17)$$

By coupling Eq. (2.16) with Eq. (2.17), the Poisson–Nernst–Planck (PNP) system is constituted as

$$\begin{aligned} \frac{\partial C_{\pm}}{\partial \tau} &= D \nabla \cdot \left( \nabla C_{\pm} \pm \frac{e}{k_B T} C_{\pm} \nabla \Phi \right), \\ -\epsilon_b \nabla^2 \Phi &= e (C_+ - C_-), \end{aligned} \quad (2.18)$$

which provides a self-consistent description of charge transport in dilute electrolytes. However, to fully characterize the system, Eq. (2.18) must be supplemented with appropriate boundary conditions, which govern both the ion fluxes and the electrostatic potential at the system boundaries. These boundary conditions, which encode the electrochemical interactions at the electrode/electrolyte interface, will be presented in the following chapters.

## 2.4.2 PNP Model in Ionic Liquids

### Bazant, Storey, and Kornyshev (BSK) Theory

The PNP system described in Eq. (2.18) can satisfactorily describe ion transport in dilute electrolyte solutions near weakly charged surfaces. However, it fails to capture key features of electrochemical systems with concentrated electrolytes such as ionic liquids where the finite size of ions and the electrostatic interaction (electrostatic correlations) become significant. Speaking of electrostatic correlations, they can significantly affect the structure and thermodynamic properties of the electrical double layer [55, 56], resulting in qualitative differences from the standard PNP model in Eq. (2.18), such as like-charge attraction [57, 58], or overscreening of surface charge [45]. Critical applications in biology, colloids, separations, or electrochemistry rely on or operate in the regime where correlation effects are critical. Numerous models have been proposed to capture electrostatic correlations, typically with a complicated mathematical structure [59, 60, 61, 62]. A simpler mathematical structure could help with the application and interpretation of electrostatic correlations to a wider class of problems in physics, including electrokinetics, colloidal interactions, and electrochemical transport/reactions. Bazant, Storey, and Kornyshev (BSK) [63] proposed a continuum framework to account for the nonlocal dielectric permittivity of ionic liquids resulting from ion-ion correlations [45] with a simple mathematical structure. The model

captures correlations based on expansions in terms of electric field, rather than ion density, in the free-energy functional which leads to a higher-order Poisson equation. In so doing, the electrostatic correlations are included self-consistently in the definition of the electrostatic potential whose gradient determines the electrostatic force on an ion in the diffuse layer. The BSK theory provides a simple framework to predict charge density oscillations and overscreening phenomena in a variety of electrokinetic, electrochemical, biophysical, and colloidal phenomena in electrolytes and ionic liquids. The equations require a similar level of complexity to solve compared to the standard PNP model in Eq. (2.18) which allows them to be applied to a broad group of applications.

The free energy functional for ionic liquids follows the same general structure as in Eq. (2.12), but includes additional terms to capture ion–ion correlations and steric (crowding) effects. Specifically, the electrostatic energy density is augmented with higher-order gradients of the potential, while the entropic contribution  $g(C_+, C_-)$  is replaced by an excess free energy density derived from a lattice-gas model. The resulting functional, known as the BSK model [63], takes the form

$$G[C_{\pm}, \Phi] = \int_V d\mathbf{r} \left( g(C_+, C_-) + \varrho(C_+, C_-) \Phi - \frac{\epsilon_b}{2} [(\nabla\Phi)^2 + L_c^2(\nabla^2\Phi)^2 + \dots] \right) \quad (2.19)$$

where  $L_c$  denotes the electrostatic correlation length. The additional term  $-\frac{\epsilon_b}{2}L_c^2(\nabla^2\Phi)^2$  represents the leading-order correction beyond the dilute limit, accounting for nonlocal electrostatic interactions. For simplicity, the expansion is truncated at this term, although higher-order corrections can be included in more refined models. The presence of higher-order derivatives in the energy functional (e.g.,  $(\nabla^2\Phi)^2$ ) leads to field equations of higher order, which in turn require additional boundary conditions.

In the context of ionic liquids, crowding (steric) effects are often incorporated using a lattice-based formulation of the free energy. Following [46, 64], the excess free energy density is given by

$$g = \frac{k_B T}{\gamma} \left[ \gamma C_+ \ln(\gamma C_+) + \gamma C_- \ln(\gamma C_-) + [1 - \gamma(C_+ + C_-)] \ln[1 - \gamma(C_+ + C_-)] \right], \quad (2.20)$$

where  $\gamma$  is defined as the minimum volume occupied by a single ion, also called the ion size, or more precisely the *effective molecular volume per lattice site*. Therefore,  $\gamma C_{\pm}$  represents the volume fraction occupied by cations and anions so that  $1 - \gamma(C_+ + C_-)$  is the free (unoccupied) volume fraction that can potentially accommodate extra ions. The term  $1/\gamma$  can be interpreted as the maximum possible ion concentration  $C_{\max}$  in the system due to

finite-size constraints, i.e.,  $C_{\max} = 1/\gamma$ . This formulation comes from lattice-gas models, where each site of volume  $\gamma$  can be occupied by one ion or left empty, thereby introducing a crowding constraint that prevents concentrations from exceeding  $1/\gamma$  (see Fig. 2.2). The value of  $\gamma$  should vary for different room-temperature ILs, but for many of them is expected to lie around or above  $1/2$ ; however, in the case of the room-temperature ILs with solvent additives it can be substantially lower [65]. We also note that the entropic contribution of the dilute electrolyte, Eq. (2.13), is recovered from Eq. (2.20) in the limit  $\gamma \rightarrow 0$ .

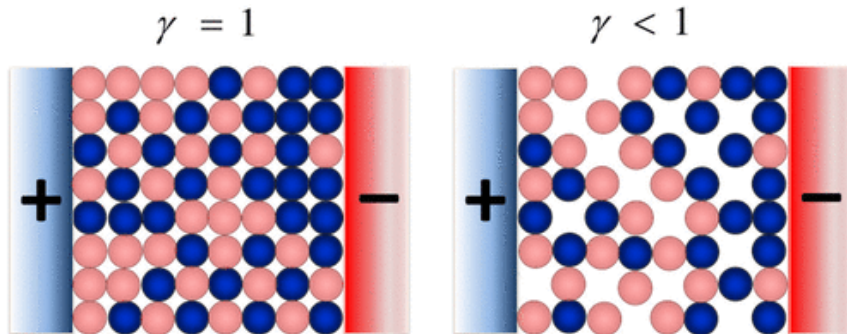


**Figure 2.2:** Schematic illustration of an ionic liquid confined between two electrodes, used to depict the concept of the packing parameter  $\gamma$ . Red and blue spheres represent anions and cations, respectively, while unoccupied sites indicate voids in the lattice. In these 2D representations, the left panel corresponds to a fully packed configuration with  $\gamma = 1$ , whereas the right panel shows a less densely packed state with  $\gamma = 3/4$ . Picture adapted from [65].

Taking the functional derivative of the free energy with respect to the ion concentrations,  $\delta G/\delta C_{\pm}$ , gives the corresponding electrochemical potential [45]

$$\mu_{\pm} = \frac{\delta G}{\delta C_{\pm}} = k_B T \ln \left[ \frac{C_{\pm}}{1 - \gamma(C_+ + C_-)} \right] \pm e\Phi. \quad (2.21)$$

Note that by setting  $\gamma = 0$  in Eq. (2.21), the electrochemical potential in dilute solution, i.e., Eq. (2.14), is recovered. Substituting Eq. (2.10) into the flux expression in Eq. (2.9) using (2.11), the modified flux density is expressed as

$$\mathbf{F}_{\pm} = -D \left[ \nabla C_{\pm} \pm \frac{e}{k_B T} C_{\pm} \nabla \Phi + \frac{\gamma C_{\pm} \nabla (C_+ + C_-)}{1 - \gamma(C_+ + C_-)} \right]. \quad (2.22)$$

We again note that by setting  $\gamma = 0$  in Eq. (2.22), the classical flux density, i.e., Eq. (2.15), is recovered.

The overscreening effects are evaluated by finding the extremum of the functional ( $\delta G/\delta\Phi = 0$ ) to derive the modified Poisson equation as

$$\epsilon_b (L_c^2 \nabla^2 - 1) \nabla^2 \Phi = \rho, \quad (2.23)$$

where  $\rho = e(C_+ - C_-)$ . Equation (2.23) represents a modified form of Maxwell's equation,  $\nabla \cdot \mathbf{D} = \rho$ , where the displacement field is defined as  $\mathbf{D} = \hat{\epsilon} \mathbf{E}$ . Here, the permittivity operator  $\hat{\epsilon} = \epsilon_b(L_c^2 \nabla^2 - 1)$  introduces nonlocal electrostatic correlations, and the electric field remains  $\mathbf{E} = -\nabla\Phi$ , within a medium of constant permittivity  $\epsilon_b$ . The classical PNP model, given by Eq. (2.18), is recovered in the limit  $L_c = 0$ . Importantly, the definition of the electrostatic potential  $\Phi$  is now modified to incorporate higher-order correlation effects, without violating the form of Maxwell's equation. Specifically, the governing equation for  $\Phi$  becomes  $\nabla \cdot (\hat{\epsilon} \mathbf{E}) = \rho$ , rather than the classical  $\nabla \cdot (\epsilon_b \mathbf{E}) = \rho$ . This reformulation enables a self-consistent inclusion of electrostatic correlation energy directly within the electrostatic framework, rather than as an external correction to the excess chemical potential. One key advantage is that the electrostatic force per unit charge acting on an ion is still captured directly by  $\mathbf{E}$ , making the diffuse potential  $\Phi$  experimentally accessible—for instance, through electrode measurements<sup>2</sup>.

Together with the modified Poisson equation, Eq. (2.23), the modified PNP system in ionic liquid is expressed as

$$\begin{aligned} \frac{\partial C_{\pm}}{\partial \tau} &= D \nabla \cdot \left[ \nabla C_{\pm} \pm \frac{e}{k_B T} C_{\pm} \nabla \Phi + \frac{\gamma C_{\pm} \nabla (C_+ + C_-)}{1 - \gamma(C_+ + C_-)} \right], \\ \epsilon_b (L_c^2 \nabla^2 - 1) \nabla^2 \Phi &= e (C_+ - C_-). \end{aligned} \quad (2.24)$$

Compared to the PNP model in dilute electrolyte case, Eq. (2.18), the modified PNP system in Eq. (2.24) requires additional and more sophisticated boundary conditions to fully describe the charge dynamics at the electrode/electrolyte interface. In particular, the presence of higher-order spatial derivatives in the potential necessitates additional boundary

---

<sup>2</sup>A defining feature of the BSK model is its incorporation of electrostatic correlations directly into the field equation, rather than through thermodynamic corrections. In many conventional approaches, such as density functional theory [66, 61, 67, 68], correlation effects are introduced via modifications to the free energy or chemical potential. As a result, the total force acting on ions includes both the electrostatic component and an additional thermodynamic contribution. In such models, the electrostatic potential  $\Phi$  still satisfies the classical Poisson equation, but the electric field  $\mathbf{E} = -\nabla\Phi$  no longer fully captures the actual force experienced by the ions. This weakens the physical interpretation of  $\Phi$  as the generator of measurable electrostatic quantities like surface charge or impedance. The BSK model, on the other hand, modifies the Poisson equation itself by introducing a nonlocal permittivity operator  $\hat{\epsilon} = \epsilon_b(L_c^2 \nabla^2 - 1)$ , so that  $\Phi$  continues to determine the electric field while incorporating correlation effects directly, thereby preserving consistency with measurable electrostatic forces.

constraints which reflect microscopic interfacial physics such as electrostatic correlations and structured charge layers. We will discuss the associated boundary conditions in Chapter 5.

### 2.4.3 PNP Model in Linear Regime

In many time-dependent applications of dilute electrolytes, especially in EIS, the PNP equations, Eq. (2.18), are linearized about the ground state where  $C_+ = C_- = c_b$  and  $\Phi = 0$  (neutral electrolyte). This is achieved by writing  $C_\pm = c_b + \delta C_\pm$  and  $\Phi = \delta\Phi$  and treating  $\delta C_\pm$  and  $\delta\Phi$  as the first-order perturbations. By subtracting Eq. (2.16) for  $C_+$  and  $C_-$ , noting that  $\delta\rho = e(\delta C_+ - \delta C_-)$ , we obtain the *Debye-Falkenhagen equation* for charge density

$$\frac{\partial\delta\varrho}{\partial\tau} = D \left( \nabla^2 - \frac{1}{\lambda_D^2} \right) \delta\varrho, \quad (2.25)$$

where

$$\lambda_D = \sqrt{\frac{\epsilon_b k_B T}{2e^2 c_b}}, \quad (2.26)$$

is recognized as the Debye screening length.

Eq. (2.25) can also be written as the continuity equation

$$\frac{\partial\delta\varrho}{\partial\tau} + \nabla \cdot \delta\mathbf{J}_c = 0, \quad (2.27)$$

where  $\delta\mathbf{J}_c = e(\delta\mathbf{F}_+ - \delta\mathbf{F}_-)$  is the linearized conduction current obtained as

$$\delta\mathbf{J}_c = -D \nabla \left( \delta\varrho + \frac{\epsilon_b}{\lambda_D^2} \delta\Phi \right), \quad (2.28)$$

where in Eq. (2.15), the ion fluxes are subtracted for positive and negative ions. Therefore, the system of PNP equation in linear regime for dilute electrolytes is

$$\begin{aligned} \frac{\partial\delta\varrho}{\partial\tau} + \nabla \cdot \delta\mathbf{J}_c &= 0, \\ -\epsilon_b \nabla^2 \delta\Phi &= \delta\varrho. \end{aligned} \quad (2.29)$$

To complete the description of the above linear system, Eq. (2.29) requires suitable boundary conditions that determine the behavior of ion fluxes and electrostatic potential at the system's boundaries, which will be introduced in the upcoming chapters.

In the case of ionic liquids, following the same process of linearization, the total ion concentration satisfies  $C_+ + C_- \approx 2c_b$  in the linear regime, and its gradient becomes negligible, i.e.,  $\nabla(C_+ + C_-) \approx 0$ . This renders the steric correction term involving  $\nabla(C_+ + C_-)$  in Eq. (2.22) negligible. As such, the linearized conduction current retains the same structure as in Eq. (2.28), while the electrostatic potential is governed by the modified Poisson equation, Eq. (2.23), which in the linear regime takes the form  $\epsilon_b (L_c^2 \nabla^2 - 1) \nabla^2 \delta\Phi = \delta\rho$ . Therefore, the linearized PNP system for ionic liquids becomes

$$\begin{aligned} \frac{\partial \delta\rho}{\partial \tau} + \nabla \cdot \delta \mathbf{J}_c &= 0, \\ \epsilon_b (L_c^2 \nabla^2 - 1) \nabla^2 \delta\Phi &= \delta\rho. \end{aligned} \tag{2.30}$$

The linear PNP model in Eq. (2.30) reveals that the electrostatic correlation length  $L_c$ , a signature of the overscreening phenomenon, plays the dominant role over the crowding phenomenon in ionic liquids. Also, in this linearized system, the presence of higher-order spatial derivatives in the potential necessitates the specification of additional boundary conditions, which account for microscopic interfacial phenomena such as electrostatic correlations and the formation of structured charge layers. These boundary conditions will be discussed in Chapter 5.

## 2.5 Method of Matched Asymptotic Expansions

Consider a one-dimensional (in the  $X$  direction) simple electrochemical cell containing a dilute, symmetric, binary electrolyte confined between parallel-plate blocking electrodes separated by  $2L$  and driven by a time-dependent external voltage. In preparation for analysis of the full, one-dimensional nonlinear PNP problem in Eq. (2.18), we cast it in a dimensionless form<sup>3</sup> using  $L$  as the reference length scale and  $\tau_c = \lambda_D L/D$  as the reference time scale. Time and space are then represented by  $t = \tau/\tau_c$  and  $x = X/L$ , and the problem is reformulated through reduced variables:  $c = (C_+ + C_-)/2c_b$  for the local salt concentration,  $\rho = (C_+ - C_-)/2c_b$  for the charge density,  $\phi = e\Phi/(k_B T)$  for the electrostatic potential. With these definitions, the dimensionless equations for the PNP problem in Eq. (2.18) are

$$\begin{aligned}\frac{\partial c}{\partial t} &= \varepsilon \frac{\partial}{\partial x} \left( \frac{\partial c}{\partial x} + \rho \frac{\partial \phi}{\partial x} \right), \\ \frac{\partial \rho}{\partial t} &= \varepsilon \frac{\partial}{\partial x} \left( \frac{\partial \rho}{\partial x} + c \frac{\partial \phi}{\partial x} \right), \\ -\varepsilon^2 \frac{\partial^2 \phi}{\partial x^2} &= \rho,\end{aligned}\tag{2.31}$$

subjected to some appropriate boundary conditions at the electrode surfaces<sup>4</sup>. In Eq. (2.31), the parameter  $\varepsilon = \lambda_D/L$ , the ratio of Debye length to the system size,  $L$ , can be viewed as the thickness of the electric double layer. Since the Debye length is much smaller than the electrolyte thickness for most electrolytes, i.e.,  $\lambda_D \ll L$ , or equivalently  $\varepsilon \ll 1$ , the  $\varepsilon$  is a small parameter in Eq. (2.31).

In the limit  $\varepsilon \rightarrow 0$ , the Poisson equation in Eq. (2.31) simplifies to  $\rho = 0$  suggesting that the system tends toward electroneutrality in the bulk. This would seem to imply that charge separation is negligible, and the electrostatic potential plays no role in the bulk dynamics. Also, setting  $\rho = 0$  eliminates one of the dependent variables from the system, thereby reducing the number of independent degrees of freedom. While the independent variables  $x$  (space) and  $t$  (time) remain unchanged, the system loses one of its dynamic fields, as the charge density no longer evolves according to its own differential equation

---

<sup>3</sup>The dimensionless formulation presented in this section is because of introducing the method of matched asymptotic expansions and the motivation for adopting such normalizations will be discussed in Chapter 4.

<sup>4</sup>For clarity and to maintain focus on the method of matched asymptotic expansions, boundary conditions are not presented in this section. A complete formulation, including boundary conditions and their role in the analysis, will be discussed in Chapter 4.

but instead becomes a constraint. As a result, the mathematical structure of the problem changes: there are fewer available dependent variables to satisfy the original set of governing equations and physical conditions. In particular, the system becomes undetermined and loses the ability to impose all boundary conditions consistently. This loss highlights the singular nature of the limit  $\varepsilon \rightarrow 0$  and motivates the need for a more careful treatment.

It is also tempting to assume that the potential must satisfy Laplace’s equation,  $\partial^2\phi/\partial x^2 = 0$ , in a neutral electrolyte. But this too is generally incorrect, especially when the ion concentrations are nonuniform. The question then arises: *how can the system be globally electroneutral while still satisfying the Poisson equation?* The resolution lies in recognizing that electroneutrality holds only *in the bulk*, away from regions where rapid variations occur. Near charged surfaces or narrow regions with large concentration gradients, the assumption of electroneutrality breaks down. In these thin regions (*thin double layers*)—whose spatial extent is proportional to  $\varepsilon$ —the full structure of the Poisson equation must be retained. Mathematically, this leads to a *singular perturbation problem*, where the small parameter  $\varepsilon$  multiplies the highest-order derivative in the governing equations, and different physical balances emerge in different regions of the domain. To handle such problems, we apply the *method of matched asymptotic expansions*, a hallmark of the boundary-layer theory.

To implement the method of matched asymptotic expansions in electrochemical systems, the domain is conceptually divided into two distinct regions: an *outer region*, corresponding to the bulk of the electrolyte where  $\varepsilon \rightarrow 0$  provides a valid leading-order approximation, and *inner regions* corresponding to the diffuse layers developed at each electrode, where rapid variation of the fields occurs over a spatial scale of order  $\varepsilon$ . The solutions in each region can be constructed through the following step-by-step procedure:

1. **Outer expansion.** In the outer region, the coordinate  $x$  remains unchanged, and the governing equations are expanded in powers of  $\varepsilon$  to form a regular perturbation series. Assuming the electrostatic potential is the quantity of interest, this means

$$\bar{\phi}(x) \sim \bar{\phi}_0(x) + \varepsilon \bar{\phi}_1(x) + \varepsilon^2 \bar{\phi}_2(x) + \dots \quad (2.32)$$

where the bar sign denotes the outer solution and the subscript “0” refers to the leading order term, “1” refers to the first correction term, “2” refers to the second correction term, etc.

2. **Inner expansion.** In the inner region, a rescaled, or *stretched* coordinate is introduced to resolve steep gradients near the boundary. This is typically done by defining<sup>5</sup>

$$y = \frac{x - x_0}{\varepsilon^\alpha}, \quad (2.33)$$

where  $x_0$  denotes the location of the boundary layer (electrodes) and  $\alpha > 0$  represents the scaling exponent that characterizes the thickness of the boundary layer (diffuse layer). The governing equations are then reformulated in terms of the inner variable  $y$ , and an independent asymptotic expansion is performed. For example, for the electrostatic potential, this means

$$\tilde{\phi}(y) \sim \tilde{\phi}_0(y) + \varepsilon^\beta \tilde{\phi}_1(y) + \varepsilon^{2\beta} \tilde{\phi}_2(y) + \dots \quad (2.34)$$

where the tilde sign denotes the inner solution. The exponent  $\beta$  in the inner expansion depends on the structure of the rescaled equation. For the inner expansion to yield a physically meaningful solution, the resulting fields must remain bounded as  $y \rightarrow \infty$ . This condition ensures that the original solution does not diverge within a finite distance in the physical variable  $x$ .

3. **Matching.** The inner and outer expansions are approximations of the same physical quantity, valid in different regions. Therefore, in an intermediate region where both expansions are valid, they must agree asymptotically. This requirement leads to the *Van Dyke matching condition*<sup>6</sup>, expressed as

$$\lim_{y \rightarrow \infty} \tilde{\phi}(y) \sim \lim_{x \rightarrow x_0} \bar{\phi}(x), \quad (2.35)$$

which states that “*the limit of the inner solution in the outer limit must equal the limit of the outer solution in the inner limit*”.

4. **Common part.** To construct a uniformly valid approximation, a *common part*, denoted by  $\phi_c(x)$ , is defined as the overlapping asymptotic behavior of both solutions

$$\phi_c(x) = \lim_{x \rightarrow x_0} \bar{\phi}(x) \sim \lim_{y \rightarrow \infty} \tilde{\phi}(y). \quad (2.36)$$

This common part is subtracted to avoid double-counting in the composite solution.

---

<sup>5</sup>In general, the choice of stretched coordinate is not unique and constitutes one of the main challenges in boundary-layer theory. However, for the asymptotic analysis presented in this thesis, the transformation given in Eq. (2.33) is consistently applicable. A broader discussion of appropriate stretching transformations can be found in [69, 70, 71].

<sup>6</sup>While the van Dyke matching principle is widely used due to its simplicity and clarity, it has limitations in more complex problems, where alternative or more sophisticated matching strategies may be required [69, 70, 71].

5. **Composite solution.** Finally, a *composite solution* is formed that is valid across the entire domain. It is constructed by adding the inner and outer solutions and subtracting their common part, i.e.,

$$\phi(x) \sim \bar{\phi}(x) + \tilde{\phi}(y) - \phi_c(x), \quad (2.37)$$

where  $y$  is given in Eq. (2.33). The composite approximation often provides excellent accuracy, even when only leading-order terms are retained in the expansions.

## 2.6 Fundamentals of the EIS

In a real electrochemical system, measurement involves various electrical, electrochemical, and physical processes taking place at the electrode/electrolyte interface. This task is very challenging as all these different processes exhibit different (from very fast to very slow) time behaviors. The resistance of a liquid electrolyte, the charging/discharging of the EDL at the electrode/electrolyte interface, the dependence of the capacitive behavior of the EDL on the morphology of the electrode surface and the composition of the electrolyte, the kinetics of an electrode charge-transfer reaction, homogeneous reactions and adsorption/desorption phenomena coupled with the electrode charge-transfer reaction, mass transfer phenomena (diffusion of species to the electrode surface), etc., exhibit different time constants as a measure of the time behavior of a process [72, 6]. These processes are widely observed in corrosion studies, semiconductor science, energy conversion and storage technologies, chemical sensing and biosensing, noninvasive diagnostics, etc. Among the available electrochemical techniques such as cyclic voltammetry, chronoamperometry and chronopotentiometry, and scanning electrochemical microscopy, EIS proves to be a promising measurement technique involving the complex processes just has been addressed [72, 6].

EIS is based on the perturbation of an electrochemical system in equilibrium or in steady-state, via the application of a sinusoidal signal (AC voltage or AC current) usually superimposed on a DC signal (voltage or current) over a wide range of frequencies and the monitoring of the sinusoidal response (current or voltage, respectively) of the system toward the applied perturbation. Considering that the electrochemical system under study is a linear time-invariant system (that is, the output signal is linearly related to the input signal and the behavior of the system is not changed over time), EIS is a *transfer function* technique that models the output signal (AC current or AC voltage) to the input signal (AC voltage or AC current) over a wide range of frequencies. Therefore, if we assume

that an AC voltage  $V(t)$  with low amplitude  $V_0$  at a particular frequency  $\omega$  is applied as  $V(t) = V_0 \sin(\omega t)$ , the resulting AC current,  $I(t)$ , with the amplitude  $I_0$  and the same frequency but at the different phase,  $\phi$  is measured according to  $I(t) = I_0 \sin(\omega t + \phi)$ . The impedance of the electrochemical cell at this frequency  $Z(\omega)$ , is then

$$Z(\omega) = |Z| e^{i\phi} = |Z| (\cos \phi + i \sin \phi) = Z_r + i Z_i, \quad (2.38)$$

where  $i = \sqrt{-1}$  is the imaginary number and  $Z_r$  and  $Z_i$  are the real part and imaginary part of the impedance which are linked to  $|Z| = \sqrt{Z_r^2 + Z_i^2}$  and  $\phi = \arctan(Z_i/Z_r)$  as the magnitude and phase, respectively. Complementary to EIS, electrochemical capacitance spectroscopy (ECS) has also been investigated to characterize the interfacial capacitive properties of graphene electrodes, as highlighted in the recent works of Bueno [10, 73, 74, 75]. In ECS, the complex impedance is converted into a complex capacitance using the relation  $C = 1/(i\omega Z) \equiv C_r + iC_i$  which places greater emphasis on the low-frequency regime, where the capacitive response of the graphene electrode becomes most significant.

The advantage of working in frequency domain over the time domain as with one of the commonly used voltammetric techniques (cyclic voltammetry, a chrono technique, etc.), is that EIS simplifies a complex electrochemical system by deconvoluting it in individual processes with different time constants, which then can be easily analyzed such that (very) slow processes can be probed in (very) low frequencies, while (very) fast processes can be probed in (very) high frequencies. Practically, the frequency range is dictated by limitations associated with the available instrumentation, the wiring of the electrochemical system with the instrument (high frequency limit), and the stability of the electrochemical system itself over time (low frequency limit). The frequency range in most of the commercially available electrochemical analyzers spans from 10  $\mu\text{Hz}$  to 1 MHz [72].

Notably, EIS measurements at an electrochemical system can be simulated to an equivalent electrical circuit, which consists of common passive components (such as resistances, capacitors) and others, more complicated elements referred to as constant phase element (CPE), connected each other in different ways. In other words, each of electrochemical processes mentioned above can consequently be deemed analog to an equivalent electrical

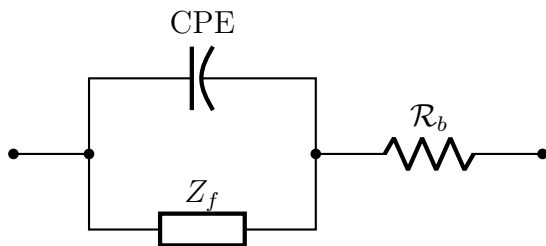


**Figure 2.3:** Circuit equivalence of a typical electrochemical process at the electrode/electrolyte interface. The faradiac reactions and heterogeneous effects are represented by the circuit elements  $Z_f$  and CPE. The bulk resistance is shown by  $R_b$ .

circuit that is characterized by a different time constant. For example, the electric circuit representation corresponding to the EIS study of a typical electrochemical process governed by three processes is shown in Fig. 2.3. The first process is the charging/discharging of the electric double layer at the electrode/electrolyte interface represented by the CPE arising from the heterogeneity of the electrode. The second process, shown as  $Z_f$ , refers to the kinetics of the faradaic reaction at the electrode/electrolyte interface and the third process, diffusion of the redox species from the bulk solution to the electrode surface, is modeled by the bulk resistance  $\mathcal{R}_b$ .

In this thesis, the electrodes are assumed to be blocking and ideally polarizable, implying that no faradaic reactions occur at the electrode surfaces. Furthermore, the electrode surfaces are considered smooth, thereby eliminating any CPE effects associated with surface roughness or heterogeneity.

# Chapter 3

## Neutral Graphene in Dilute Electrolytes

### 3.1 Introduction

In this chapter, the frequency behavior of the graphene/electrolyte interface in simple (dilute) electrolytes is investigated for two cases; (1) graphene is modeled with an infinite conductivity, and (2) graphene possesses a finite conductivity. In both cases, graphene is taken nominally neutral at room temperature where it exhibits finite quantum capacitance, whereas the mathematical modeling of the electrolyte region is based on Debye-Hückel treatment (linearized PNP models). In the first case, we will show that the graphene/electrolyte interface acts as a simple capacitor (quantum capacitor), while in the second case, the modeling reveals an impedance behavior at the surface of the graphene/electrolyte.

## 3.2 Graphene with an Infinite Conductivity\*

### 3.2.1 PNP Model

We study a one-dimensional electrochemical cell aligned along the  $X$ -axis, composed of two planar, parallel, and dissimilar electrodes with large surface areas, separated by an electrolyte layer of thickness  $L$ . The system is subjected to a time-varying, harmonically oscillating electric potential, denoted by  $V_a(\tau)$ . The metal electrode is positioned at  $X = L$ , while the graphene electrode lies at  $X = 0$ . A mathematical model for this setup is developed based on the following set of assumptions: (1) the electrolyte is binary, containing only two ionic species with equal and opposite valencies,  $z_+ = z_- = 1$ , and sharing identical diffusion coefficients  $D_+ = D_- = D$ , mobilities  $\mu_+ = \mu_- = \mu$ , and equilibrium bulk concentrations  $c_b$ ; (2) the formation of the Stern layer, representing the outer Helmholtz plane, is neglected at both electrode interfaces consistent with the classical Gouy–Chapman description that applies in the limit of dilute electrolytes, where ion–electrode specific interactions and finite-size effects are negligible; (3) ion adsorption or desorption phenomena near the electrodes are not considered; (4) both electrodes act as blocking (non-Faradaic), meaning that no charge transfer or Faradaic currents occur between the electrolyte and the electrodes [76]; and (5) the cell remains in a globally neutral equilibrium state, which is then slightly perturbed by the application of a small external potential  $V_a(\tau)$ .

A schematic representation illustrating the doping of graphene through the potential drop across the electrochemical cell is presented in Fig. 3.1, along with its associated equivalent circuit composed of capacitors [52]. In this figure,  $\varepsilon_F(\tau)$  denotes the Fermi level of graphene at  $X = 0$ ,  $V_q(\tau)$  refers to the potential inside the graphene linked to its doping level, and  $V_d(\tau)$  represents the potential drop across the diffuse layer within the electrolyte. The two cones correspond to the low-energy segments of the  $\pi$ -electron bands of graphene, modeled under the rigid band approximation [77], where the Dirac point is placed at the local electric potential at the graphene interface, leading to the relation  $\varepsilon_D(\tau) = -e\Phi_0(\tau)$ , with  $\Phi_0(\tau) \equiv \Phi(0, \tau)$ . Since the electronic response in graphene to electrical perturbations occurs on a timescale much shorter than that of ionic dynamics in the electrolyte, it is reasonable to assume that  $\varepsilon_F(\tau)$ ,  $\varepsilon_D(\tau)$ , and  $V_q(\tau) \equiv [\varepsilon_F(\tau) - \varepsilon_D(\tau)]/e$  adjust instantaneously to changes in the applied potential. Furthermore, by taking the potential at the metal electrode to be zero, i.e.,  $\Phi_L(\tau) \equiv \Phi(L, t) = 0$ , the potential drop across the diffuse layer becomes  $V_d(\tau) = -\Phi_0(\tau)$ , as depicted in Fig. 3.1. The equivalent

---

<sup>2\*</sup>The material presented in this section has been published in the *Journal of Electroanalytical Chemistry* (M. Yavarian et al., 2023) [51].

circuit also includes the quantum capacitance of graphene at equilibrium, labeled as  $\mathcal{C}_q$ , and the Debye capacitances  $\mathcal{C}_D = \epsilon_b/\lambda_D$  associated with the diffuse layers adjacent to both electrodes (definitions for these capacitances are provided below), where  $\epsilon_b$  is the permittivity of the electrolyte and  $\lambda_D = \sqrt{\epsilon_b k_B T / (2e^2 c_b)}$  is the Debye screening length.

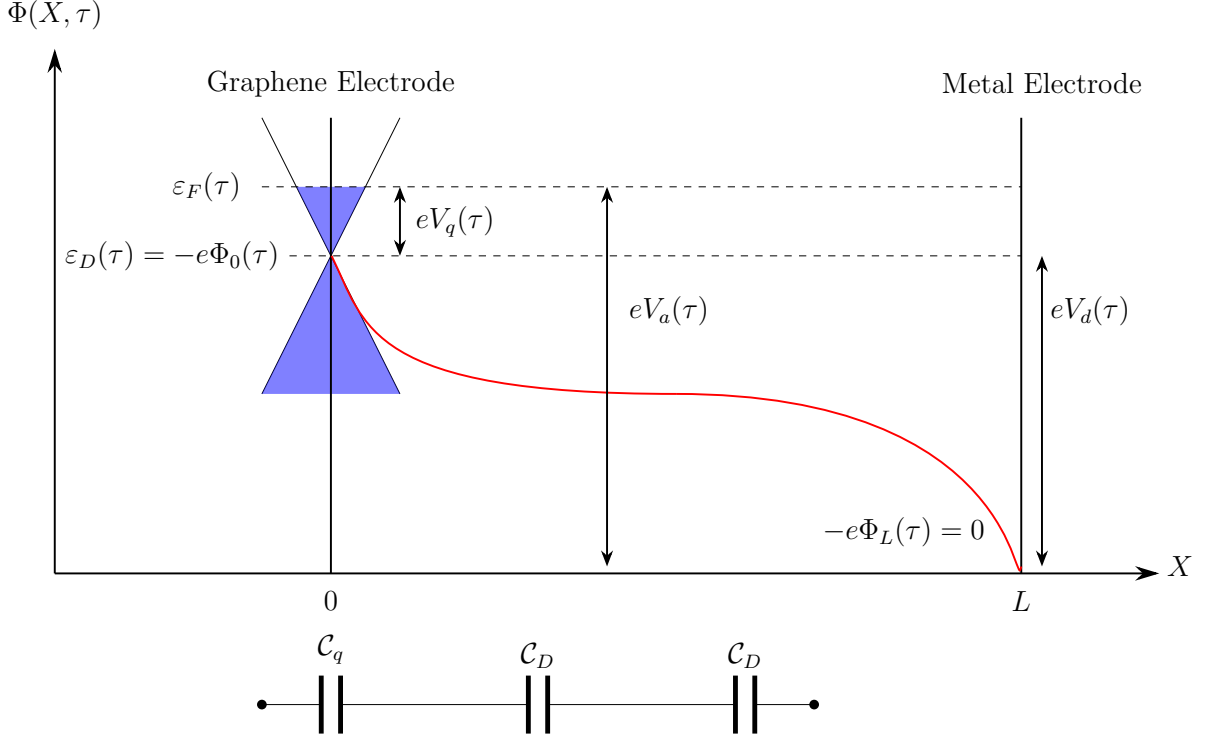


**Figure 3.1:** Schematic diagram depicting the electrostatic potential  $\Phi(X, \tau)$  as a function of the spatial coordinate  $X$ , alongside electron energy levels and their corresponding equivalent capacitors. The quantities  $\epsilon_F(\tau)$  and  $\epsilon_D(\tau) = -e\Phi_0(\tau) = -e\Phi_0(\tau)$  represent the time-dependent Fermi energy and the Dirac point of graphene, respectively. Also illustrated are the potential differences occurring within the graphene layer at  $X = 0$ , which are responsible for its doping, expressed as  $V_q(\tau) = \Phi_0(\tau) + \epsilon_F(\tau)/e$ , as well as the potential drop  $V_d(\tau)$  across the diffuse layers adjacent to both the graphene and metal electrodes. The term  $\mathcal{C}_q$  denotes the quantum capacitance of graphene at equilibrium located at  $X = 0$ , while  $\mathcal{C}_D$  refers to the Debye capacitance.

Introducing a small AC perturbation to the applied voltage,  $V_a(\tau)$ , allows us to model the problem with the linearized form of the PNP equations derived in Chapter 2 (Eq. 2.29) subject to appropriate boundary conditions. In the following, we drop the  $\delta$  sign, as the perturbed part, to simply the notations.

To solve Eq. 2.29, we first introduce the set of boundary conditions stemming from the assumption that the electrodes are blocking, meaning no Faradaic current is present at their surfaces, i.e,  $J_c(0, \tau) = J_c(L, \tau) = 0$ , leading to

$$\left[ \frac{\partial^3 \Phi(X, \tau)}{\partial X^3} - \frac{1}{\lambda_D^2} \frac{\partial \Phi(X, \tau)}{\partial X} \right] \Big|_{X=0,L} = 0, \quad (3.1)$$

in which the Poisson equation, Eq. (2.17), is substituted into the expression of the conduction current in Eq. (2.28). Concerning the potential, we assume the metal electrode is grounded, giving the boundary condition  $\Phi(L, \tau) = 0$ . Furthermore, applying both the continuity of the electrostatic potential and Gauss's law at the graphene surface leads to the following conditions at  $X = 0^+$

$$\Phi(0, \tau) = -V_d(\tau), \quad (3.2)$$

$$-\epsilon_b \frac{\partial \Phi(X, \tau)}{\partial X} \Big|_{X=0} = \varsigma_g(\tau), \quad (3.3)$$

where  $\varsigma_g(\tau) \approx -\mathcal{C}_q V_q(\tau)$  denotes the linearized surface charge density of graphene with  $\mathcal{C}_q$  being the quantum capacitance of neutral graphene introduced in Section 2.2. Knowing the relation  $V_a(\tau) = V_d(\tau) + V_q(\tau)$  from Fig. 3.1, we can substitute  $V_d(\tau)$  and  $V_q(\tau)$  into Eq. (3.2) and Eq. (3.3) to arrive at a Robin-type inhomogeneous boundary condition for the potential at  $X = 0^+$ :

$$\epsilon_b \frac{\partial \Phi(X, \tau)}{\partial X} \Big|_{X=0} - \mathcal{C}_q \Phi(0, \tau) = \mathcal{C}_q V_a(\tau). \quad (3.4)$$

This boundary condition, characterizing the graphene electrode, constitutes one of the principal modeling contributions of this work.

## Frequency Domain

Given that the governing equations have been linearized, we can now apply the Laplace transform, which replaces the time dependence with a new variable  $s = i\Omega\tau_D$ , where  $\Omega$  is the frequency of the applied voltage  $V_a(\tau)$  and  $\tau_D = \lambda_D^2/D$  is the Debye time. Time is normalized according to  $t = \tau/\tau_D$  with the normalized frequency introduced as  $\omega = \Omega\tau_D$ . To proceed, we introduce normalized forms of the independent variables as follows:  $x = X/\lambda_D$ ,  $\ell = L/\lambda_D$ ,  $c = (C_+ + C_-)/2c_b$ ,  $\rho = (C_+ - C_-)/2c_b$ , and  $\{\phi, v\} = e/(k_B T)\{\Phi, V\}$ .

The perturbed electric current density is normalized via  $j = J/J_{\text{lim}}$ , where the limiting current is given by  $J_{\text{lim}} = 2eDc_b/\lambda_D$  [78].

With these scalings, by substituting the Poisson equation, Eq. (2.17), into the continuity equation, Eq. (2.29), taking into account Eq. (2.28), we obtain a fourth-order ordinary differential equation with constant coefficients for the potential

$$\frac{\partial^4 \phi(x, s)}{\partial x^4} - (1 + s) \frac{\partial^2 \phi(x, s)}{\partial x^2} = 0. \quad (3.5)$$

The above governing equation is associated the blocking electrode boundary conditions, Eq. (3.1), being normalized as

$$\left[ \frac{\partial^3 \phi(x, s)}{\partial x^3} - \frac{\partial \phi(x, s)}{\partial x} \right] \Big|_{x=0, \ell} = 0, \quad (3.6)$$

and the grounded metal electrode

$$\phi(\ell, s) = 0, \quad (3.7)$$

along with the graphene boundary condition, Eq. (3.4), normalized as

$$\Gamma \frac{\partial \phi(x, s)}{\partial x} \Big|_{x=0} - \phi(0, s) = v_a(s), \quad (3.8)$$

where we introduce the dimensionless parameter  $\Gamma = \mathcal{C}_D/\mathcal{C}_q$ . This parameter is central to assessing the influence of the graphene electrode on the overall impedance response of the system across a wide range of equilibrium salt concentrations  $c_b$ .

### 3.2.2 Impedance I

To determine the impedance of the system, we must first evaluate the total current flowing through the electrochemical cell. The total current is spatially uniform and does not depend on the coordinate  $X$  [79]. It can be expressed as the sum  $J(\tau) = J_c(X, \tau) + J_d(X, \tau)$ , where  $J_d(X, \tau) = -\epsilon_b \frac{\partial^2 \Phi(X, \tau)}{\partial X \partial \tau}$  is the displacement current [80]. Given that the conductive current vanishes at the surface of the graphene due to the blocking electrode boundary condition, i.e.,  $j_c(0, s) = 0$ , the total current can be evaluated using the displacement current evaluated at  $x = 0^+$  as

$$j(s) = -s \frac{\partial \phi(x, s)}{\partial x} \Big|_{x=0}. \quad (3.9)$$

The impedance of the electrochemical cell is defined through the relation  $Z(s) = u(s)/j(s)$ , where  $u(s) = -v_a(s)$  denotes the applied potential at the graphene with respect to the grounded metal electrode (with current flowing in the positive  $x$ -direction), and  $j(s)$  is obtained by solving the governing equation, Eq. (3.5), using the boundary conditions mentioned in Eqs. (3.6) - (3.8). Consequently, the normalized impedance of the electrochemical cell comprising a GM electrode configuration is given by

$$Z(s) = \frac{\Gamma}{s} + \frac{2 \tanh\left(\frac{\ell}{2} \sqrt{1+s}\right)}{s(1+s)^{3/2}} + \frac{\ell}{1+s}. \quad (3.10)$$

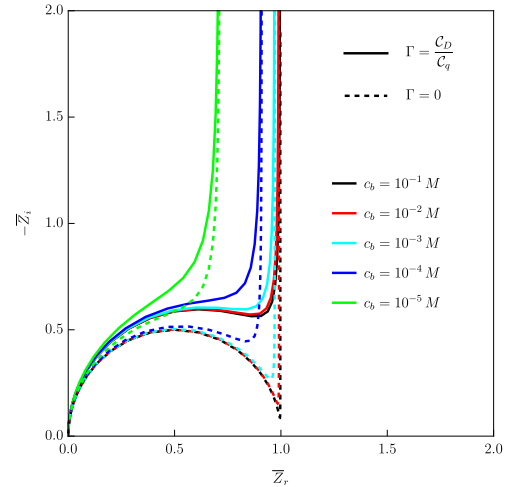
To understand the role of graphene's finite quantum capacitance, it is helpful to recall that the quantum capacitance of an ideal metallic bulk electrode is commonly taken to be infinite [81, 4, 82, 83, 84, 85]. This reflects the assumption that the density of states (DOS) in a metal is so high that adding or removing charge from the surface does not significantly alter its Fermi energy level. Referring to Fig. 3.1, this would imply  $V_q(\tau) = 0$ , which is clearly not suitable for graphene due to its low DOS near the Dirac point. Nonetheless, for the purpose of a *formal* substitution of a graphene electrode with an ideal metal electrode at  $X = 0$ , it is sufficient to take the limit  $\mathcal{C}_q \rightarrow \infty$ , which enforces  $V_q(\tau) = 0$  and simplifies Eq. (3.4) to  $\Phi(0, \tau) = -V_a(\tau)$ , thereby replacing Eq. (3.2). In this scenario, Eq. (3.3) becomes unnecessary, as the electrode charge in an ideal metal is entirely governed by the potential drop throughout the electrolyte. As a result, the impedance of a symmetric cell with two ideal metal electrodes is recovered by taking  $\Gamma = 0$  in Eq. (3.10) [86]. Under this limiting case, the boundary condition in Eq. (3.8) simply becomes  $\phi(0, s) = u(s)$ , as expected.

### 3.3 Results and Discussion I

The parameters used in the calculations throughout this section are chosen to represent an aqueous electrolyte solution at room temperature, characterized by a permittivity  $\epsilon_b = 80 \epsilon_0$ , where  $\epsilon_0 \approx 8.85 \times 10^{-12}$  F/m denotes the vacuum permittivity. The equilibrium ion concentration  $c_b$ , corresponding to the neutral bulk region, is treated as a variable parameter within the system. We express  $c_b$  in units of moles per litre (M) [87], representative of a monovalent ionic aqueous solution at room temperature. Under these conditions, the inverse Debye screening length is given by  $\lambda_D \approx 0.3/\sqrt{c_b}$  nm, and the Debye capacitance is estimated as  $\mathcal{C}_D \approx 299\sqrt{c_b}$   $\mu\text{F}/\text{cm}^2$ . For graphene, the quantum capacitance

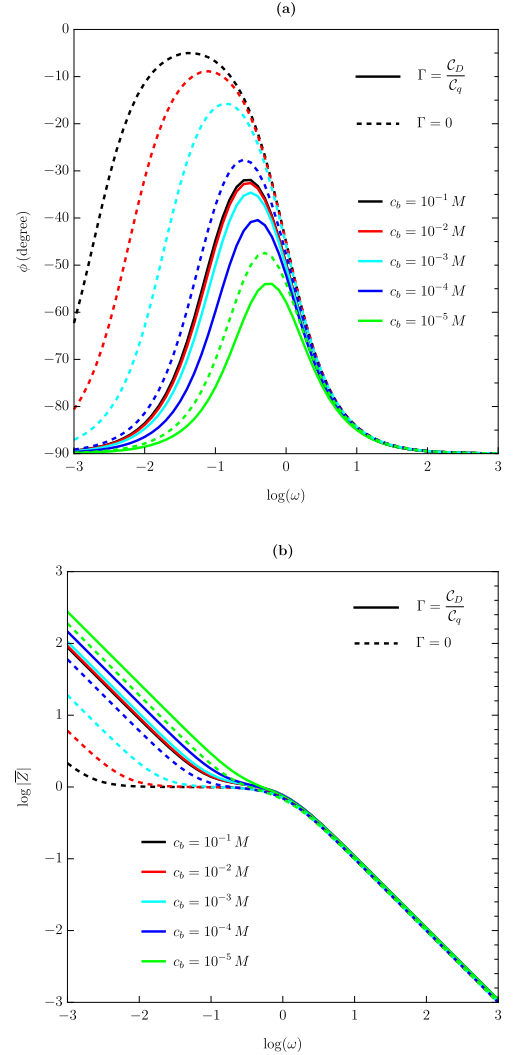
at room temperature is approximately  $\mathcal{C}_q \approx 0.8 \mu\text{F}/\text{cm}^2$ , yielding a dimensionless ratio  $\Gamma \approx 287.5\sqrt{c_b}$ . In alignment with the experimental data referenced in [76, 88], both the impedance spectroscopy and capacitive spectroscopy presented in this work are evaluated for a range of bulk ion concentrations, from  $c_b = 10^{-1} \text{ M}$  to  $c_b = 10^{-5} \text{ M}$ , while the electrolyte thickness is fixed at  $L = 1 \mu\text{m}$ . Our analysis will particularly emphasize behavior in the low-frequency regime.

Fig. 3.2 illustrates how the ion concentration influences the impedance response, presented in the form of a Nyquist plot. To isolate the effect of ion concentration alone, the impedance is further normalized by the electrolyte thickness, resulting in  $\bar{Z} = Z/\ell = \bar{Z}_r + i\bar{Z}_i$ . Starting from the origin, which corresponds to the high-frequency limit, the plot shows no noticeable offset near the origin. This indicates the absence of ohmic resistance, such as that introduced by the solution, connectors, or wiring [89, 90], for both electrode configurations (GM and MM). In the mid-frequency range, a semicircular feature appears in the Nyquist plot for both types of electrode pairs, reflecting the impact of electrolyte thickness and the charging behavior within the bulk electrolyte. This portion of the curve is associated with electrolyte polarization, which involves ion motion through the electrolyte medium. As the frequency decreases further, entering the low-frequency regime, Fig. 3.2 displays an upward deflection of the curves with reduced curvature. In this regime, ions begin to accumulate in the double-layer region, initiating the charging process. According to the figure, at very low frequencies, the Nyquist curves for both electrode types and all ion concentrations exhibit nearly vertical slopes. This behavior indicates that the charging dynamics are predominantly controlled by the electric double layer and occur in the absence of Faradaic reactions. The sharp rise at low frequencies stems from the assumption that both electrodes are blocking or ideally polarized [90], meaning that only displacement (capacitive) current contributes at the electrode surfaces.



**Figure 3.2:** Illustration of the Nyquist Plot for different ion concentrations with the electrolyte thickness of  $L = 1 \mu\text{m}$ . The solid lines refer to the GM electrode pair, and the dashed lines refer to the MM electrode pair.

One of the limitations of Nyquist plots is their inability to clearly illustrate how impedance varies with frequency. To address this issue, the Bode phase plot and Bode magnitude plot are commonly employed and are shown in Fig. 3.3. The Bode phase plot, Fig. 3.3(a), is defined as  $\phi = \arctan(\bar{Z}_i/\bar{Z}_r)$  and is plotted against frequency for different ion concentrations, with the phase angle expressed in degrees. As frequency decreases, the phase angle for both GM and MM systems approaches  $\phi = -90^\circ$  across all concentration values, highlighting the capacitive behavior. At higher ion concentrations, the impedance behavior of the MM electrode pair in the low-frequency regime increasingly deviates from capacitive characteristics, eventually approaching resistive behavior as indicated by  $\phi \rightarrow 0$ . Also noticeable is the effect of ion concentration on the peak positions in the Bode phase plot. As seen in the figure, the MM electrode pair exhibits a more pronounced peak shift with increasing concentration than the GM pair. The Bode magnitude plot which shows  $|\bar{Z}| = \sqrt{(\bar{Z}_r)^2 + (\bar{Z}_i)^2}$ , is presented in Fig. 3.3(b). According to the figure, the impedance decreases as frequency increases. Furthermore, the slopes near -1 are characteristic of capacitive behavior, while those with slopes close to 0 indicate resistive behavior [89]. From the figure, we observe that at low frequencies, the slope of the GM electrode pair curves for all concentrations approaches -1, indicating predominantly capacitive behavior. In comparison, the MM electrode pair curves attain a slope of -1 only at much lower frequencies, implying a more resistive nature at intermediate frequencies. This observation is consistent with the trends seen in the Bode phase plot. In the intermediate frequency range, the slopes of both types of electrode pairs flatten toward zero, demonstrating resistive behavior.



**Figure 3.3:** Bode. (a) Illustration of the Bode phase plot for different concentrations with the electrolyte thickness of  $L = 1 \mu\text{m}$ . The solid lines refer to the GM electrode pair, and the dashed lines refer to the MM electrode pair. (b) Illustration of Bode magnitude plot for different concentrations with the electrolyte thickness of  $L = 1 \mu\text{m}$ . The solid lines refer to the GM electrode pair, and the dashed lines refer to the MM electrode pair.

As an alternative to EIS, in ECS, the complex impedance is transformed into a complex capacitance via the relation  $C = 1/(sZ) \equiv C_r + iC_i$ . In terms of dimensional quantities, the normalized complex capacitance  $C$  is related to the physical capacitance  $\mathcal{C}(s)$  through the expression  $C = \mathcal{C}(s)/\mathcal{C}_D$ .

Fig. 3.4 presents the capacitive Nyquist plots for both GM and MM electrode pairs across various ion concentration levels. As illustrated, each Nyquist capacitive curve forms a semicircle, where the intercepts of  $C_r$  with the horizontal axis provide key insights into the capacitive structure of the system in both the high- and low-frequency regimes. In the low-frequency limit ( $\omega \ll 1$ ), under the assumption that  $\ell \gg 1$ —an approximation applicable to most practical scenarios [91]—the capacitance evaluates to  $C_r(s=0) = (\Gamma + 2)^{-1}$ . Given that  $\Gamma = \mathcal{C}_D/\mathcal{C}_q$ , this can be expressed in physical units as  $\mathcal{C}_r(\Omega=0) = (\mathcal{C}_q^{-1} + 2\mathcal{C}_D^{-1})^{-1}$ . This result corresponds to the equivalent circuit representation illustrated in Fig. 3.1. A clearer understanding of the low-frequency behavior can be achieved by expanding the impedance expression, Eq. (3.10), in a power series with respect to the normalized frequency  $\omega$ , assuming a finite value of  $\ell$ . The leading two terms in this expansion provide an approximate form of the impedance given by  $Z_{\text{LF}} \approx \frac{1}{i\omega C_{\text{LF}}} + R$ , where the first term represents the capacitive response in the low-frequency limit with  $C_{\text{LF}} = [\Gamma + 2 \tanh(\ell/2)]^{-1}$ , and the second term corresponds to a normalized resistance at low-frequency limit, expressed as  $R = \ell + (\ell/2) \text{sech}^2(\ell/2) - 3 \tanh(\ell/2)$ . In contrast, for large frequencies where  $\ell\sqrt{\omega} \gg 1$ , the impedance approximates to  $Z_{\text{HF}} \approx \frac{1}{i\omega}(\Gamma + \ell)$ . This reflects the high-frequency limit of the real part of the capacitance as  $C_r(s \rightarrow i\infty) = (\Gamma + \ell)^{-1}$ , which translates to the physical units as  $\mathcal{C}_r(\Omega \rightarrow \infty) = (\mathcal{C}_q^{-1} + \mathcal{C}_G^{-1})^{-1}$ , where  $\mathcal{C}_G = \epsilon_b/L$  represents the geometric capacitance of the cell. By introducing a characteristic graphene length scale  $\lambda_g = \epsilon_b/\mathcal{C}_q$ , which evaluates to  $\lambda_g \approx 89$  nm at room temperature, we conclude that the high-frequency

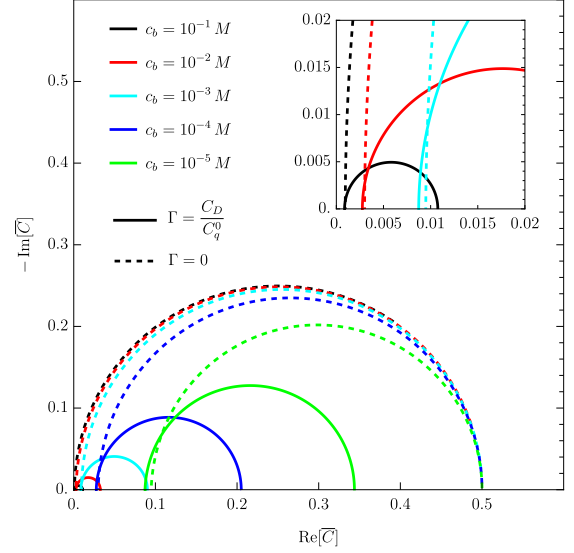


**Figure 3.4:** Illustration of the capacitive Nyquist Plot for different concentrations with the electrolyte thickness of  $L = 1\mu\text{m}$ . The solid lines refer to the GM electrode pair, and the dashed lines refer to the MM electrode pair. The inset magnifies the capacitive behavior in high-frequency regime.

intercept of the capacitive Nyquist plot with the real axis satisfies  $\mathcal{C}_r(\Omega \rightarrow \infty) \approx \mathcal{C}_G$  when the condition  $L \gg \lambda_g$  holds true. This result is valid for both electrode types and is independent of the ion concentration. This trend is observed in Fig. 3.4, including its inset which highlights the behavior at higher ion concentrations. Consequently, we deduce that the quantum capacitance of graphene is most effectively detected through the low-frequency intercept of the capacitive Nyquist plot with the real axis. This is particularly evident at low ion concentrations, where the condition  $\mathcal{C}_q \ll \mathcal{C}_D$  leads to  $\mathcal{C}_r(\Omega = 0) \approx \mathcal{C}_q \approx 0.8 \mu\text{F}/\text{cm}^2$ . In this section, we demonstrated the capacitive behavior of the graphene electrode arising from its assumed infinite conductivity. In the next section, we will make the model more realistic by accounting for the finite conductivity of graphene, which leads to a generalized boundary condition in Eq. (3.4) and a corresponding modification of the electrochemical impedance expression in Eq. (3.10). This generalization explicitly captures the electrodynamic response of the graphene electrode, providing a more comprehensive framework for modeling the graphene/electrolyte interface.

## 3.4 Graphene with a Finite Conductivity\*

### 3.4.1 Model Description

We examine an electrochemical cell with a cylindrical shape, having radius  $a$  and length  $L$ . The spatial domain inside the cell is described by  $(\mathbf{R}, X)$ , where  $\mathbf{R} = (R, \theta)$  denotes the polar coordinates and  $X$  is the axial coordinate. Graphene is electrostatically doped via an ideal metallic contact shaped as a narrow ring electrode surrounding the GE [92, 93]. A time-dependent potential  $V_a(\tau)$  is applied to this contact and assumed to be uniformly distributed along the circumference of the GE, thereby ensuring axial symmetry of the system and eliminating any dependence on the polar angle  $\theta$ . The potential  $V_a(\tau)$  is considered to vary slowly enough in time to maintain a quasi-equilibrium electrochemical potential (or Fermi level)  $\varepsilon_F(\tau)$  across the graphene surface. Under the assumption that the electrostatic potential throughout the cell,  $\Phi(R, X, \tau)$ , shifts the Dirac point of graphene's  $\pi$  electronic bands to the energy level  $-e\Phi(R, 0, \tau)$  relative to the grounded ME (where  $e > 0$  is the elementary charge), a spatially varying chemical potential develops along the graphene, given by  $\mu_q(R, \tau) = \varepsilon_F(\tau) + e\Phi(R, 0, \tau)$ . This chemical potential determines the local surface number density of electrons,  $n(R, \tau)$ .

---

<sup>2\*</sup>The material presented in this section has been published in *The Journal of Physical Chemistry C* (M. Yavarian et al., 2025).

In Fig. 3.5, we schematically illustrate the potential drop within the doped graphene, represented as  $V_q(R, \tau) \equiv \mu_q(R, \tau)/e$ , together with the externally applied potential  $V_a(\tau)$  and the average potential drop across the electrolyte resulting from the diffuse layers near the two electrodes, denoted by  $V_d(\tau)$ . To align with relevant experimental setups and practical considerations [93], the model also incorporates the contact resistance  $\mathcal{R}_c$ , which captures contributions from electrode connections, wiring, and the external measurement circuitry.

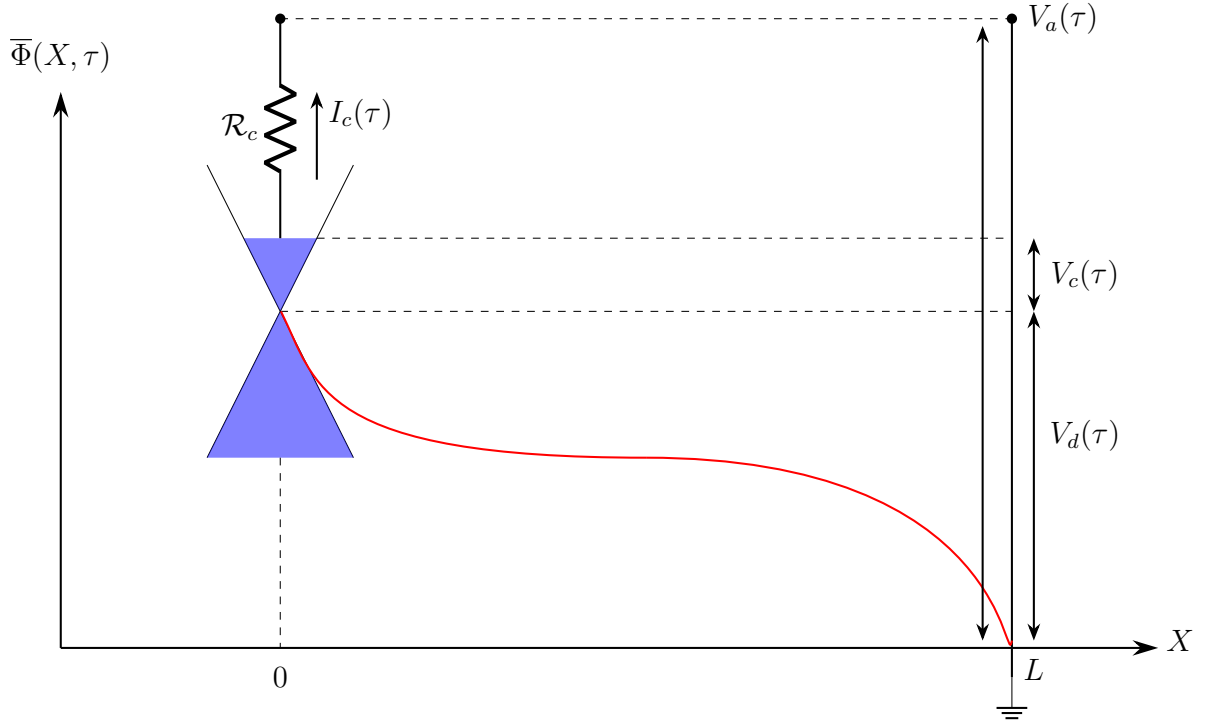


**Figure 3.5:** A schematic diagram of the proposed electrochemical cell flanked by the GE at  $X = 0$  and the grounded ME at  $X = L$ . The dependence on the position  $X$  of the surface average of the electrostatic potential in the electrolyte,  $\bar{\Phi}(X, \tau)$ , when the system is subject to a time-dependent voltage,  $V_a(\tau)$ , is shown with  $V_c(\tau)$  being the potential drop around the edge of the GE and  $V_d(\tau)$  denoting the potential drop across the diffuse layer in the electrolyte. The external circuitry is represented by the contact resistance,  $\mathcal{R}_c$ , and the contact current  $I_c(\tau)$  passing through  $\mathcal{R}_c$ .

### 3.4.2 Graphene Disk Electrode

The schematic view of the graphene disk electrode is shown in Fig. 3.6. The central region is graphene, which is the electrochemically active material. *Al wire contact*: The graphene needs to be electrically contacted so its potential can be controlled and its current measured. An Al (aluminum) wire is attached as the back-end electrical lead. *Insulating film*: The graphene electrode is partially covered with an insulating material (often a polymer or oxide). This prevents the electrolyte from wetting or shorting the contact area and ensures that only a defined window of graphene is exposed to the electrolyte. *Exposed graphene (ungated area)*: The central region left uncovered by the insulator is the active electrode surface where the electrolyte interacts directly with graphene.

In Refs. [94, 95], it was demonstrated that the relaxation of excess charge in graphene is primarily controlled by its compressibility, which originates from the quantum-mechanical properties of the resident two-dimensional electron gas (2DEG) in equilibrium, as well as Coulombic interactions among the electrons. These studies showed that in a regime near the charge-neutral state of graphene (i.e., for undoped or intrinsic graphene), and under strong dielectric screening from the surrounding environment (as is the case when graphene is in contact with an aqueous solution), Coulomb interactions can be neglected. As a result, the relaxation of charge carriers with surface number density  $n(\mathbf{R}, \tau)$  follows a two-dimensional diffusion process,

$$\frac{\partial n}{\partial \tau} = D_q \nabla_{\mathbf{R}}^2 n, \quad (3.11)$$

where  $\nabla_{\mathbf{R}}$  denotes the gradient operator with respect to the in-plane coordinates  $\mathbf{R}$ , and  $n$  is positive in electron-doped regions and negative in hole-doped regions of graphene. The diffusion coefficient  $D_q$  for graphene satisfies a generalized Einstein relation for the 2DEG [95, 94],

$$D_q = \frac{\sigma}{e^2} \frac{\partial \mu_q}{\partial n}, \quad (3.12)$$

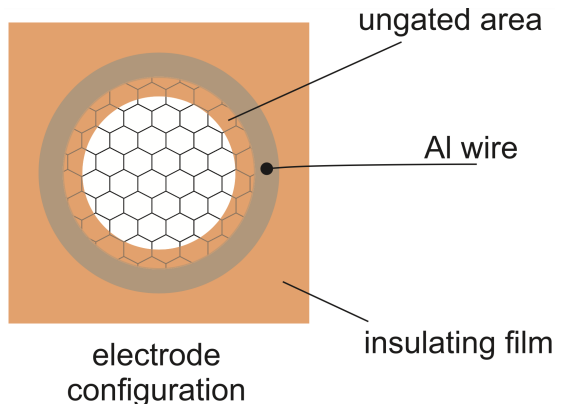


**Figure 3.6:** Schematic of the graphene disk electrode. The Al wire provides electrical contact, while an insulating film limits electrolyte access to a defined central window. The exposed graphene (ungated area) serves as the electrochemically active surface. Picture adapted from [93].

where  $\sigma$  is the in-plane DC electrical conductivity (more precisely, conductance, measured in Siemens), and  $\mu_q$  is the chemical potential of the graphene charge carriers. We focus on the regime near intrinsic graphene, where  $\mu_q(n)$  can be approximated by a linear expansion around the neutrality point  $n = 0$  (also called the Dirac point), leading to  $\mu_q \approx \left. \frac{\partial \mu_q}{\partial n} \right|_0 n$ . This approximation remains accurate within a few percent as long as  $|\mu_q| \lesssim k_B T$  (see Section 2.2). Accordingly, the compressibility (or density of states) in Eq. (3.12) may be evaluated at  $n = 0$ , yielding  $\left. \frac{\partial \mu_q}{\partial n} \right|_0 = \frac{e^2}{\mathcal{C}_q}$ .

At the same time, determining the electrical conductivity  $\sigma$  of graphene near the neutrality point at finite temperature is considerably more challenging, primarily due to the influence of disorder. This disorder gives rise to a landscape of electron-hole puddles, which contributes to the well-known—though still not fully understood—concept of minimum conductivity in graphene at the Dirac point [96]. Experimental measurements of this minimum conductivity vary widely, typically clustering around the so-called universal conductivity,  $\sigma_0 = e^2/(4\hbar) \approx 61.2 \mu\text{S}$ . From a theoretical standpoint, different scattering mechanisms responsible for disorder-induced momentum relaxation of thermally excited carriers in nearly neutral graphene suggest a power-law temperature dependence of the form  $\sigma \propto T^\alpha$ , where  $\alpha$  can take on values of 0, 1, or 2 [97]. Based on this, we take  $\sigma_0$  as a lower bound for the conductivity of neutral graphene, which is broadly supported by the experimental data reported in Ref. [98] (see Fig. 4), Ref. [99] (see Fig. 3b), and Ref. [100] (see Fig. 6a). This choice also enables us to estimate the diffusion constant in Eq. (3.12) as  $D_q = \frac{\sigma_0}{\mathcal{C}_q} \approx 74.5 \text{ cm}^2/\text{sec}$  at room temperature. While a more refined treatment of  $\sigma$  at finite temperatures may yield a higher value for  $D_q$ , it will nonetheless remain finite. This confirms that graphene behaves quite differently from an idealized metallic electrode with infinite conductivity (zero resistance) when operating in electrolyte environments.

Equation (3.11) can be reformulated as a diffusion equation for the potential drop in graphene,  $V_q(R, \tau)$ , by applying the previously mentioned linear approximation of the chemical potential near the neutrality point,  $\mu_q = eV_q \approx \left. \frac{\partial \mu_q}{\partial n} \right|_0 n = \frac{e^2}{\mathcal{C}_q} n$ . This expression can then be rewritten in the form of a continuity equation for the charge induced in graphene,

$$\frac{\partial \varsigma_g(R, \tau)}{\partial \tau} + \nabla_{\mathbf{R}} \cdot \mathbf{J}_g(R, \tau) = 0, \quad (3.13)$$

where  $\varsigma_g = -en \approx -\mathcal{C}_q V_q$  denotes the surface charge density. This allows us to identify the corresponding diffusive current density as  $\mathbf{J}_g = eD_q \nabla_{\mathbf{R}} n \approx \sigma_0 \nabla_{\mathbf{R}} V_q$ .

We may apply the Laplace transform to Eq. (3.13), thereby replacing  $\partial/\partial\tau \mapsto S$ , and further substituting  $S = i\Omega$  to address the steady-state regime under periodic excitation at angular frequency  $\Omega$ . By rearranging Eq. (3.13) and carrying out the spatial derivatives, we obtain the modified Bessel differential equation [101] governing the transformed potential  $V_q(R, \Omega)$  in graphene,

$$\left[ \frac{\partial^2}{\partial R^2} + \frac{1}{R} \frac{\partial}{\partial R} - \zeta^2(\Omega) \right] V_q(R, \Omega) = 0, \quad (3.14)$$

where the frequency-dependent parameter  $\zeta(\Omega)$  is defined as

$$\zeta(\Omega) = \sqrt{i\Omega \frac{\mathcal{C}_q}{\sigma_0}}, \quad (3.15)$$

whose complex form plays a central role in modeling the surface impedance of the graphene layer, as will be elaborated in the next sections.

Equation (3.14) must be solved over the interval  $0 \leq R \leq a$  (see Fig. 3.6), subject to the boundary conditions  $\partial V_q/\partial R = 0$  at  $R = 0$ , and  $V_q(a, \Omega) = V_c(\Omega)$ , where  $V_c(\Omega)$  is the transformed potential at the circumference of graphene, set by the surrounding metal ring electrode. It is assumed here that the radius of the GE is sufficiently large so that edge effects related to graphene's screening at the contact with the metal ring can be neglected [102]. The general solution to the second-order differential equation (3.14) can be written in terms of modified Bessel functions of the first and second kinds [101] as

$$V_q(R, \Omega) = A_1(\Omega) I_0[R\zeta(\Omega)] + A_2(\Omega) K_0[R\zeta(\Omega)], \quad (3.16)$$

where  $I_0[R\zeta(\Omega)]$  and  $K_0[R\zeta(\Omega)]$  are the zero-order modified Bessel functions of the first and second kinds, respectively. The coefficients  $A_1(\Omega)$  and  $A_2(\Omega)$  are determined by the boundary conditions. To ensure that the potential drop inside graphene remains finite at the center ( $R = 0$ ), we invoke the known limiting behaviors of modified Bessel functions [101], where  $I_0[R\zeta(\Omega)] \rightarrow 1$  and  $K_0[R\zeta(\Omega)] \rightarrow \infty$  as  $R \rightarrow 0$ . Since  $K_0[R\zeta(\Omega)]$  diverges at the origin, we must set  $A_2(\Omega) = 0$  to maintain a physically acceptable solution. Applying the boundary condition at the disk edge  $R = a$ , where the potential is fixed at  $V_c(\Omega)$ , gives  $A_1(\Omega) = V_c(\Omega)/I_0[a\zeta(\Omega)]$ . Therefore, the in-plane potential drop in graphene is given by

$$V_q(R, \Omega) = V_c(\Omega) \frac{I_0[R\zeta(\Omega)]}{I_0[a\zeta(\Omega)]}. \quad (3.17)$$

Next, we evaluate the total current at the graphene disk edge ( $R = a$ ), flowing into the surrounding metal ring electrode (via the Al wire in Fig. 3.6), expressed as a line integral,

$$I_c(\Omega) = \oint dl \hat{\mathbf{n}} \cdot \mathbf{J}_g(R, \Omega) = 2\pi a \sigma_0 \left. \frac{\partial V_q(R, \Omega)}{\partial R} \right|_{R=a}. \quad (3.18)$$

By considering Eq. (3.17), the result obtained in Eq. (3.18) leads to

$$I_c(\Omega) = 2\pi\sigma_0 V_c(\Omega) a\zeta(\Omega) \frac{I_1[a\zeta(\Omega)]}{I_0[a\zeta(\Omega)]}. \quad (3.19)$$

From this, we define the *quantum impedance* of the graphene disk electrode according to

$$\mathcal{Z}_q(\Omega) = \frac{V_c(\Omega)}{I_c(\Omega)} = \frac{\mathcal{R}_q}{2a\zeta(\Omega)} \frac{I_0[a\zeta(\Omega)]}{I_1[a\zeta(\Omega)]}. \quad (3.20)$$

where  $\mathcal{R}_q = 1/(\pi\sigma_0)$  is recognized as the *quantum sheet resistance* of the graphene disk electrode. We can further write the variable appearing in Eq. (3.20) as  $a\zeta(\Omega) = \sqrt{i\Omega\mathcal{R}_q\mathcal{C}_Q}$ , where  $\mathcal{C}_Q = A\mathcal{C}_q$  is the *total* quantum capacitance of a neutral GE with  $A = \pi a^2$  being its area. This prompts us to introduce the dimensionless frequency as  $\omega_q = \Omega\tau_q$ , where we define the characteristic *quantum time scale* of GE as

$$\tau_q = \mathcal{R}_q\mathcal{C}_Q. \quad (3.21)$$

For practical applications, it may be worthwhile mentioning that the value of the quantum time scale per unit area of graphene is estimated as  $\tau_q/A = 1/(\pi D_q) \approx 4.3$  msec/cm<sup>2</sup> at room temperature.

With the dimensionless frequency of graphene defined as  $\omega_q = \Omega\tau_q$ , the quantum impedance obtained in Eq. (3.20) can be recast in normalized form as  $Z_q(\omega_q) = \mathcal{Z}_q(\Omega)/\mathcal{R}_q$ , yielding

$$Z_q(\omega_q) = \frac{1}{2\sqrt{i\omega_q}} \frac{I_0[\sqrt{i\omega_q}]}{I_1[\sqrt{i\omega_q}]}. \quad (3.22)$$

This expression for graphene's quantum impedance closely resembles the one derived in Ref. [93] for a circular GE, which was based on the distributed circuit element approach originally developed for semiconductor field-effect transistor films [103]. While such distributed models are typically phenomenological, our derivation offers an *ab initio* framework grounded in the microscopically well-defined quantum-mechanical properties of graphene. Additionally, it is worth noting that our description of charge relaxation in graphene is strongly connected to the concept of quantum-mechanical rate spectroscopy discussed in Ref. [74]. Notably, the inverse of the quantum time scale defined in Eq. (3.21) corresponds exactly to the quantum rate introduced in that work, which also employed the same physical interpretation for resistance and capacitance.

It is instructive to examine the limiting behaviors of Eq. (3.22) in the regimes of high and low dimensionless frequency  $\omega_q$ . The limit  $\omega_q \gg 1$  physically represents a regime of

“fast” charging and/or graphene exhibiting low conductivity and/or having a large total quantum capacitance. Using the asymptotic forms of the modified Bessel functions, we find that in the limit  $\omega_q \rightarrow \infty$ , Eq. (3.22) reduces to  $Z_q^W(\omega_q) = \frac{1}{2\sqrt{i\omega_q}}$ . This expression corresponds to a Warburg impedance [104], which describes one-dimensional diffusion along a long channel of length  $a$ . This result may also be recovered by neglecting the middle term in the left-hand side of Eq. (3.14) and proceeding with the same analytical steps outlined above.

In the opposite regime—corresponding to slow charging, and/or graphene possessing a small total quantum capacitance, and/or high conductivity—we consider the asymptotic behavior of the modified Bessel functions as  $\omega_q \rightarrow 0$ . From Eq. (3.22), this leads to the expression  $Z_q^{RC}(\omega_q) = \frac{1}{8} + \frac{1}{i\omega_q}$ . In physical units, Eq. (3.20) yields in this limit  $Z_q^{RC}(\Omega) = \frac{\mathcal{R}_q}{8} + \frac{1}{i\Omega\mathcal{C}_q}$ , indicating that the GE behaves as a series combination of a resistor with resistance  $\mathcal{R}_q/8 \approx 650\ \Omega$  and a capacitor with capacitance  $\mathcal{C}_q$ . This result supports the perspective of graphene acting as a purely capacitive element, consistent with earlier theoretical descriptions of graphene electrodes in the static regime, particularly when interfaced with liquid electrolytes [105] and ionic liquids [106].

Finally, to further clarify the relaxation behavior of charge carriers in a finite-sized graphene sheet—governed by the quantum time scale  $\tau_q$ —it is instructive to consider how the spatial average of the potential drop on graphene,  $\bar{V}_q(\tau)$  (or equivalently, the average surface charge density), evolves in real time in response to an applied step-like voltage from the surrounding ring electrode. Specifically, let  $V_c(\tau) = V_0 H(\tau)$ , where  $V_0$  is the (small) amplitude of the applied potential and  $H$  denotes the Heaviside unit step function. This question is most effectively addressed by revisiting the solution in Eq. (3.17) and transforming it into the Laplace domain via the substitution  $i\Omega \mapsto S$ . The area-averaged transformed potential drop in graphene is then given by

$$\begin{aligned} \bar{V}_q(S) &= \frac{1}{A} \iint V_q(R, S) dA \\ &= \frac{2\pi}{A} \int_0^a V_q(R, S) R dR \\ &= V_c(S) K_q(S), \end{aligned} \tag{3.23}$$

where the response function  $K_q(S)$  is derived from Eq. (3.17) and takes the form

$$K_q(S) = \frac{2}{\sqrt{S\tau_q}} \frac{I_1[\sqrt{S\tau_q}]}{I_0[\sqrt{S\tau_q}]}. \tag{3.24}$$

It is important to note that this expression is essentially a normalized version of the so-called complex capacitance [74, 107], which is typically obtained in the frequency domain from the impedance in Eq. (3.20) as

$$\mathcal{K}_q(\omega_q) \equiv \frac{1}{i\Omega \mathcal{Z}_q(\Omega)} = \frac{2\mathcal{C}_Q}{\sqrt{i\omega_q}} \frac{I_1[\sqrt{i\omega_q}]}{I_0[\sqrt{i\omega_q}]}.$$
 (3.25)

By defining the normalized complex capacitance as  $K_q = \mathcal{K}_q/\mathcal{C}_Q$  and making the substitution  $i\omega_q \mapsto S\tau_q$ , we recover the result in Eq. (3.24).

By substituting the Laplace transform of the step input,  $V_c(S) = V_0/S$ , into Eq. (3.23), the problem reduces to performing the inverse Laplace transform of  $\bar{V}_q(S)$  in order to answer the previously posed question. While the general inversion with  $K_q(S)$  from Eq. (3.24) typically requires numerical techniques, analytical expressions for the average potential in graphene,  $\bar{V}_q(\tau)$ , can be obtained in the limiting cases of high and low frequencies—corresponding to the Warburg and RC-circuit regimes of the GE, respectively. These results are discussed in more detail in Subsection 3.5.1.

### 3.4.3 Electrolyte Region

Since working with a finite-sized GE is essential to capture its charge inhomogeneity and dynamic behavior, determining the electrostatic potential  $\Phi(R, X, \tau)$  throughout the cell entails solving a fully 3D problem within a cylindrical domain—an effort simplified by the axial symmetry inherent in the design of the GE [108, 109]. However, this task lies beyond the scope of the present study, as our primary focus is on investigating the coupling between the GE’s charging dynamics and ion transport, under the assumption that the electrode area  $A = \pi a^2$  is sufficiently large such that the dominant variation of the potential  $\Phi(R, X, \tau)$  occurs along the axial direction  $X$ . This allows us to work with surface-averaged quantities over the base area of the cylinder. Leveraging the fact that the Debye length in the electrolyte,  $\lambda_D$ , is much smaller than the cell radius ( $\lambda_D \ll a$ ), we may neglect fringing fields near the lateral boundary of the cylinder as  $R \rightarrow a$ , thereby approximating the electrolyte as effectively one-dimensional. This approximation is supported by recent theoretical results for a metallic disk electrode in an electrolyte, where a full 3D analysis using the Hankel transform revealed that the electrostatic potential remains nearly uniform in the radial direction—both near the electrode surface (up to its edge) and throughout the bulk [108]. In this subsection, we employ the same theoretical framework as in Ref. [108] to transition the analysis to a 1D electrolyte domain, starting from the linearized PNP equations. Through appropriate non-dimensionalization, we identify key parameters that simplify the system into a one-dimensional Debye–Falkenhagen equation, which we formulate in terms of the surface-averaged electrostatic potential in the electrolyte. Given that the surface averages of both the potential drop and charge density in the GE have already been established in the previous subsection, the approximations introduced here allow us to extend the formalism previously developed in Section 3.2, where the GE was modeled as a uniformly charged capacitor.

In the electrolyte domain defined by  $0 \leq R \leq a$  and  $0 \leq X \leq L$ , we begin with the continuity equation,

$$\frac{\partial \varrho(R, X, \tau)}{\partial \tau} + \nabla \cdot \mathbf{J}_c(R, X, \tau) = 0, \quad (3.26)$$

where  $\varrho(R, X, \tau)$  denotes the total ionic charge density, which is related to the electrostatic potential through Poisson’s equation,

$$\epsilon_b \nabla^2 \Phi(R, X, \tau) = -\varrho(R, X, \tau), \quad (3.27)$$

The linearized expression for the conduction current density is given by

$$\mathbf{J}_c(R, X, \tau) = -D \nabla \left[ \varrho(R, X, \tau) + \frac{\epsilon_b}{\lambda_D^2} \Phi(R, X, \tau) \right]. \quad (3.28)$$

Substituting Eq. (3.28) into Eq. (3.26) and applying Poisson's equation, Eq. (3.27), leads to the following governing equation for the electrostatic potential

$$\left[ \nabla^4 - \left( \frac{1}{\lambda_D^2} + \frac{1}{D} \frac{\partial}{\partial \tau} \right) \nabla^2 \right] \Phi(R, X, \tau) = 0, \quad (3.29)$$

where  $\nabla^4 \equiv (\nabla^2)^2$  represents the biharmonic (or bilaplacian) operator. This equation is subject to boundary conditions that reflect the assumption of blocking electrodes, meaning the normal component of the conduction current must vanish at the electrode surfaces

$$\begin{aligned} \hat{\mathbf{X}} \cdot \mathbf{J}_c(R, 0, \tau) &= 0, & 0 \leq R \leq a, \\ -\hat{\mathbf{X}} \cdot \mathbf{J}_c(R, L, \tau) &= 0, & 0 \leq R \leq a. \end{aligned} \quad (3.30)$$

where  $\pm \hat{\mathbf{X}}$  denotes the unit normal vector pointing into the electrolyte. In addition, the metal disk electrode is grounded

$$\Phi(R, L, \tau) = 0, \quad 0 \leq R \leq a. \quad (3.31)$$

We also assume that electrostatic influences outside the cylindrical region are negligible, i.e.,

$$\Phi(R, X, \tau) = 0, \quad R > a, \quad 0 \leq X \leq L. \quad (3.32)$$

To simplify the problem, we proceed by applying the zero-order Hankel transform, defined as [110]

$$\begin{aligned} \mathcal{H}_0 \left\{ \Phi(R, X, \tau) \right\} &= \hat{\Phi}(K, X, \tau) = 2\pi \int_0^\infty \Phi(R, X, \tau) J_0(2\pi RK) R dR, \\ \mathcal{H}_0^{-1} \left\{ \hat{\Phi}(K, X, \tau) \right\} &= \Phi(R, X, \tau) = 2\pi \int_0^\infty \hat{\Phi}(K, X, \tau) J_0(2\pi RK) K dK, \end{aligned} \quad (3.33)$$

where  $J_0$  is the Bessel function of the first kind of order zero. Applying this transform to Eq. (3.29) and using the identities  $\mathcal{H}_0\{\nabla^2\} = -K^2 + \partial^2/\partial X^2$  and  $\mathcal{H}_0\{\nabla^4\} = (-K^2 + \partial^2/\partial X^2)^2$  [111], the governing equation in the Hankel domain becomes

$$\left[ \left( -K^2 + \frac{\partial^2}{\partial X^2} \right)^2 - \left( \frac{1}{\lambda_D^2} + \frac{1}{D} \frac{\partial}{\partial \tau} \right) \left( -K^2 + \frac{\partial^2}{\partial X^2} \right) \right] \hat{\Phi}(K, X, \tau) = 0. \quad (3.34)$$

Next, we non-dimensionalize the variables by defining  $x = X/\lambda_D$  for the spatial coordinate, which gives the dimensionless electrolyte thickness  $\ell = L/\lambda_D$ ;  $k = aK$  for the Hankel

variable; and  $t = \tau/\tau_D$  for time, where  $\tau_D = \lambda_D^2/D$  is the Debye time scale. Applying the Laplace transform then corresponds to the substitution  $\partial/\partial t \mapsto s = i\omega$ , where we define the dimensionless frequency in the electrolyte as  $\omega = \Omega\tau_D$ . As a result, the governing equation in Eq. (3.34) becomes, in terms of non-dimensional variables

$$\left[ \left( -\delta^2 k^2 + \frac{\partial^2}{\partial x^2} \right)^2 - (1+s) \left( -\delta^2 k^2 + \frac{\partial^2}{\partial x^2} \right) \right] \widehat{\Phi}(k, x, s) = 0, \quad (3.35)$$

where  $\delta = \lambda_D/a$  is introduced as a key parameter in the analysis.

In practical situations, the area of a GE can be on the order of  $1 \text{ cm}^2$  [93], while the Debye length in very dilute electrolytes is typically no more than  $\sim 1 \text{ }\mu\text{m}$ . Thus, the condition  $\lambda_D \ll a$  is well satisfied, allowing us to take the limit  $\delta \ll 1$ . In this regime, the dependence on  $k$  becomes negligible, as the coefficients in Eq. (3.35) involve only the product  $\delta^2 k^2 = (\lambda_D K)^2$ . Neglecting these terms provides a very accurate approximation, affecting the solution only at small radial distances  $R \lesssim \lambda_D$ , which are negligible compared to the cell radius  $a$ . Accordingly, the Hankel-transformed potential  $\widehat{\Phi}(k, x, s)$  can be approximated by solving Eq. (3.35) with  $k = 0$ . This solution can then be used in Eq. (3.33), along with the boundary condition in Eq. (3.32), to define the surface-averaged potential in the electrolyte as

$$\overline{\Phi}(x, s) \equiv \frac{\widehat{\Phi}(0, x, s)}{A}. \quad (3.36)$$

By setting  $k = 0$  in Eq. (3.35) and dividing through by  $A$ , we obtain a fourth-order ordinary differential equation with constant coefficients for the surface-averaged potential

$$\frac{\partial^4 \overline{\Phi}(x, s)}{\partial x^4} - (1+s) \frac{\partial^2 \overline{\Phi}(x, s)}{\partial x^2} = 0. \quad (3.37)$$

The corresponding boundary conditions can be derived by applying the same reasoning to the original ones. For the blocking electrodes (from Eq. (3.30)), we obtain:

$$\begin{aligned} \left[ \frac{\partial^3 \overline{\Phi}(x, s)}{\partial x^3} - \frac{\partial \overline{\Phi}(x, s)}{\partial x} \right] \Big|_{x=0} &= 0, \\ \left[ \frac{\partial^3 \overline{\Phi}(x, s)}{\partial x^3} - \frac{\partial \overline{\Phi}(x, s)}{\partial x} \right] \Big|_{x=\ell} &= 0, \end{aligned} \quad (3.38)$$

and for the grounded metal electrode (from Eq. (3.31)), we have:

$$\overline{\Phi}(\ell, s) = 0. \quad (3.39)$$

### 3.4.4 Graphene/Electrolyte Interface

In this subsection, we derive a boundary condition for the surface-averaged potential in the electrolyte,  $\bar{\Phi}(X, \Omega)$ , at the location of the graphene electrode (GE), i.e., at  $X = 0$ . This additional condition, together with the boundary conditions given in Eqs. (3.38) and (3.39), are required to uniquely determine the solution of the one-dimensional governing equation in Eq. (3.37). The desired boundary condition is obtained by applying Gauss' law to a pillbox-shaped region that encloses the entire GE, thereby relating the surface-averaged normal electric field in the electrolyte at  $X = 0$  to the total charge on the GE, which is regulated by the external circuit. This analysis leads to the derivation of a non-homogeneous Robin-type boundary condition involving both the value of  $\bar{\Phi}(X, \Omega)$  and its spatial derivative at  $X = 0$ .

We begin by applying the Hankel transform to Eq. (3.17) using the definition in Eq. (3.33) and assuming that  $V_q(R, \Omega) = 0$  for  $R > a$ , which is consistent with the boundary condition in Eq. (3.32) at  $X = 0$ . This yields

$$\begin{aligned}\widehat{V}_q(K, \Omega) &= 2\pi \int_0^a V_q(R, \Omega) J_0(2\pi RK) R dR \\ &= \frac{V_c(\Omega)}{I_0[a\zeta(\Omega)]} \frac{2\pi a}{\zeta^2(\Omega) + 4\pi^2 K^2} \\ &\quad \times \left[ \zeta(\Omega) I_1[a\zeta(\Omega)] J_0(2\pi aK) + 2\pi K I_0[a\zeta(\Omega)] J_1(2\pi aK) \right],\end{aligned}\tag{3.40}$$

with  $\zeta(\Omega)$  defined in Eq. (3.15). Meanwhile, the total charge on the GE,  $Q_g(\Omega)$ , is obtained by integrating the surface charge density  $\varsigma_g(R, \Omega) \approx -\mathcal{C}_q V_q(R, \Omega)$  over the disk

$$Q_g(\Omega) \approx -2\pi \mathcal{C}_q \int_0^a V_q(R, \Omega) R dR = -\mathcal{C}_q \widehat{V}_q(0, \Omega),\tag{3.41}$$

where the second equality follows by evaluating Eq. (3.40) at  $K = 0$ . In parallel with Eq. (3.36), we define the surface-averaged potential drop in graphene in terms of its Hankel transform at  $K = 0$

$$\bar{V}_q(\Omega) = \frac{\widehat{V}_q(0, \Omega)}{A}.\tag{3.42}$$

Substituting the  $K \rightarrow 0$  limit of Eq. (3.40) into Eq. (3.42), we obtain the following relation between the surface-averaged potential drop in graphene and the edge potential  $V_c(\Omega)$

$$\bar{V}_q(\Omega) = V_c(\Omega) \frac{2}{a\zeta(\Omega)} \frac{I_1[a\zeta(\Omega)]}{I_0[a\zeta(\Omega)]}.\tag{3.43}$$

As expected, this expression is equivalent to the result obtained earlier in Eqs. (3.23) and (3.24), upon noting that  $a\zeta(\Omega) = \sqrt{i\Omega\tau_q}$  from Eqs. (3.15) and (3.21), and substituting  $i\Omega \mapsto S$ .

Next, by dividing Eq. (3.41) by the electrode area  $A$  and using Eq. (3.42), we arrive at an expression for the surface average charge density on graphene:  $\bar{\sigma}_g(\Omega) = Q_g(\Omega)/A = -\mathcal{C}_q \bar{V}_q(\Omega)$ . Substituting Eq. (3.43) into this relation yields

$$\bar{\sigma}_g(\Omega) = -V_c(\Omega) \frac{2\mathcal{C}_q}{a\zeta(\Omega)} \frac{\text{I}_1[a\zeta(\Omega)]}{\text{I}_0[a\zeta(\Omega)]}. \quad (3.44)$$

This expression can be coupled with Gauss's law (in the frequency domain), which relates the surface-averaged electric field at the GE interface to the average surface charge

$$-\epsilon_b \left. \frac{\partial \bar{\Phi}(X, \Omega)}{\partial X} \right|_{X=0} = \bar{\sigma}_g(\Omega). \quad (3.45)$$

This relation serves as the foundation for the required boundary condition at  $X = 0$ . By substituting Eq. (3.44) into Eq. (3.45), one can eliminate  $\bar{\sigma}_g(\Omega)$  and express the boundary condition entirely in terms of  $V_c(\Omega)$  and the derivative of  $\bar{\Phi}(X, \Omega)$ .

In the final step of deriving the boundary condition, we express the edge potential  $V_c(\Omega)$  which governs the charging dynamics of graphene in the frequency domain—as (see Fig. 3.5):

$$V_c(\Omega) = V_g(\Omega) - V_d(\Omega), \quad (3.46)$$

where  $V_g(\Omega) = E_F(\Omega)/e$ , with  $E_F(\Omega)$  representing the electrochemical potential (Fermi level) in graphene, assumed to be known and controlled by the external circuit. The term  $V_d(\Omega) = -\bar{\Phi}(0, \Omega)$  denotes the surface-averaged total potential drop across the electrolyte, measured from the ME to the Dirac point of graphene. Substituting Eq. (3.44) into Eq. (3.45), and replacing  $V_c(\Omega)$  using Eq. (3.46) as  $V_c(\Omega) = V_g(\Omega) + \bar{\Phi}(0, \Omega)$ , we rearrange the resulting expression and switch to non-dimensional variables using  $x = X/\lambda_D$  and  $s = i\omega$ , where  $\omega = \Omega\tau_D$ . This yields a Robin-type boundary condition for the surface-averaged electrolyte potential at  $x = 0$

$$\Gamma(s) \left. \frac{\partial \bar{\Phi}(x, s)}{\partial x} \right|_{x=0} - \bar{\Phi}(0, s) = V_g(s). \quad (3.47)$$

Here,  $\Gamma(s)$  is introduced as a dimensionless function generalizing the parameter  $\Gamma = \mathcal{C}_D/\mathcal{C}_q$  that was introduced in Eq. (3.8), and which is

$$\Gamma(s) = \frac{\gamma(s)}{2\mathcal{C}_q} \frac{\text{I}_0[\gamma(s)]}{\text{I}_1[\gamma(s)]}, \quad (3.48)$$

where  $C_q = \mathcal{C}_q/\mathcal{C}_D$  is the normalized quantum capacitance of neutral graphene, and  $\mathcal{C}_D = \epsilon_b/\lambda_D$  is the Debye capacitance per unit area of the electrolyte. The dimensionless variable  $\gamma(s)$  is defined as

$$\gamma(s) = a\zeta(\Omega) = \sqrt{s\eta}, \quad (3.49)$$

where  $\eta = \tau_q/\tau_D$  is the ratio of the quantum and Debye time scales. Alternatively, the function in Eq. (3.48) can be written as  $\Gamma(s) = 1/[C_q K_q(s)]$ , where  $K_q(s)$  is defined in Eq. (3.24) with the substitution  $S\tau_q = s\eta$ .

We emphasize that Eq. (3.48) plays a central role in this study, as it characterizes the surface impedance of the graphene/electrolyte interface by linking the graphene electrode (GE) and the electrolyte subsystems through two distinct mechanisms: first, via the parameter  $C_q = \mathcal{C}_q/\mathcal{C}_D$ , which governs the amplitude of  $\Gamma(s)$  by reflecting the ratio of their respective capacitances; and second, via  $\eta = \tau_q/\tau_D$ , which determines the frequency dependence in  $\gamma(s)$  by capturing the ratio of their characteristic time scales. In the absence of external circuitry ( $V_c(\Omega) = 0$ ), it is also worth highlighting that the boundary condition in Eq. (3.47), when expressed in physical units, represents a generalized form of the condition previously derived as Eq. (3.4) which stems from involving of graphene's finite conductivity into the model—an effect that is captured through the functional dependence of  $\Gamma(s)$  as given in Eq. (3.48).

### 3.4.5 Impedance II

To evaluate the total impedance of the coupled GE/electrolyte system, we first note that the total current in the electrolyte is independent of the axial coordinate  $X$ . Since the electrodes are blocking, the total current is effectively governed by the displacement current at the electrode interfaces. This total current can be derived by integrating the local displacement current density over the surface of the GE

$$I(\tau) = -2\pi\epsilon_b \int_0^a \frac{\partial}{\partial\tau} \frac{\partial\Phi(R, X, \tau)}{\partial X} \Big|_{X=0} R dR. \quad (3.50)$$

In the frequency domain, the above expression becomes

$$I(\Omega) = -i\Omega A\epsilon_b \frac{\partial\bar{\Phi}(X, \Omega)}{\partial X} \Big|_{X=0} = i\Omega A \bar{\sigma}_g(\Omega), \quad (3.51)$$

where we have used Gauss's law from Eq. (3.45) to relate the surface-averaged electric field to the average surface charge. Substituting Eq. (3.44) and comparing with Eq. (3.19)

shows that  $I(\Omega) = -I_c(\Omega)$ , indicating that current is conserved across the system. In other words, the total displacement current  $I$  that flows out of the GE surface into the electrolyte is equal in magnitude and opposite in direction to the current  $I_c$  that flows from the graphene sheet into the surrounding metal ring electrode.

From this point forward, we proceed exactly as in Section 3.2 to derive the total impedance of the system,  $\mathcal{Z}(\Omega)$ , with the only modification being the form of the total externally applied potential (see Fig. 3.5):

$$V_a(\tau) = -\mathcal{R}_c I_c(\tau) - V_g(\tau), \quad (3.52)$$

where the term  $\mathcal{R}_c I_c(\tau)$  represents the potential drop across the contact resistance, accounting for contributions external to the GE/electrolyte system, while the second term,  $V_g(\tau) = V_c(\tau) + V_d(\tau)$ , corresponds to the electrochemical potential of the GE relative to the grounded metal electrode (ME), and governs the internal potential distribution within the GE/electrolyte domain. We now non-dimensionalize the variables in the frequency domain using  $x = X/\lambda_D$  and  $s = i\omega = i\Omega\tau_D$ . The governing equation (3.37) is solved subject to the boundary conditions in Eqs. (3.38), (3.39), and (3.47), where the right-hand side of the latter is replaced by  $V_g(s) = -V_a(s) + \mathcal{R}_c I(s)$ . Once  $\bar{\Phi}(x, s)$  is determined, the current is evaluated using Eq. (3.51), which in dimensionless variables becomes

$$I(s) = -A \frac{s}{\tau_D} \frac{\epsilon_b}{\lambda_D} \frac{\partial \bar{\Phi}(x, s)}{\partial x} \Big|_{x=0}. \quad (3.53)$$

We conclude by defining the total electrochemical impedance of the graphene/electrolyte interface in the frequency domain as  $\mathcal{Z}(s) = V_a(s)/I(s)$ . To express this result in dimensionless form, we normalize  $\mathcal{Z}$  by the bulk resistance of the electrolyte,  $\mathcal{R}_b = L\lambda_D^2/(\epsilon_b DA)$ , introducing the scaled impedance  $Z = \mathcal{Z}/\mathcal{R}_b$ . This yields the final expression:

$$Z(s) = R_c + \frac{1}{\ell} \left[ \frac{\Gamma(s)}{s} + \frac{2 \tanh\left(\frac{\ell}{2} \sqrt{1+s}\right)}{s(1+s)^{3/2}} + \frac{\ell}{1+s} \right], \quad (3.54)$$

where  $R_c = \mathcal{R}_c/\mathcal{R}_b$  denotes the contact resistance normalized by the bulk resistance. The result encapsulates the combined dynamical response of the graphene electrode and the electrolyte medium, with distinct contributions arising from quantum capacitance, finite ionic relaxation, and circuit coupling.

The impedance formulation presented in Eq. (3.54) extends the theoretical model developed in Section 3.2 as Eq. (3.10), which treated graphene as a perfect conductor. In contrast, the present expression incorporates the finite conductivity of graphene via the frequency-dependent function  $\Gamma(s)$  defined in Eq. (3.48). This refinement enables the model to more accurately capture the dynamic electrochemical behavior of the graphene electrode, thereby providing a more complete and physically consistent description of the GE/electrolyte interface.

## 3.5 Results and Discussion II

In this section, we begin by presenting the results of the frequency-domain analysis for the graphene disk electrode, as developed in Subsection 3.4.2. We then broaden the discussion to include the full frequency response characteristics of the coupled graphene/electrolyte interface.

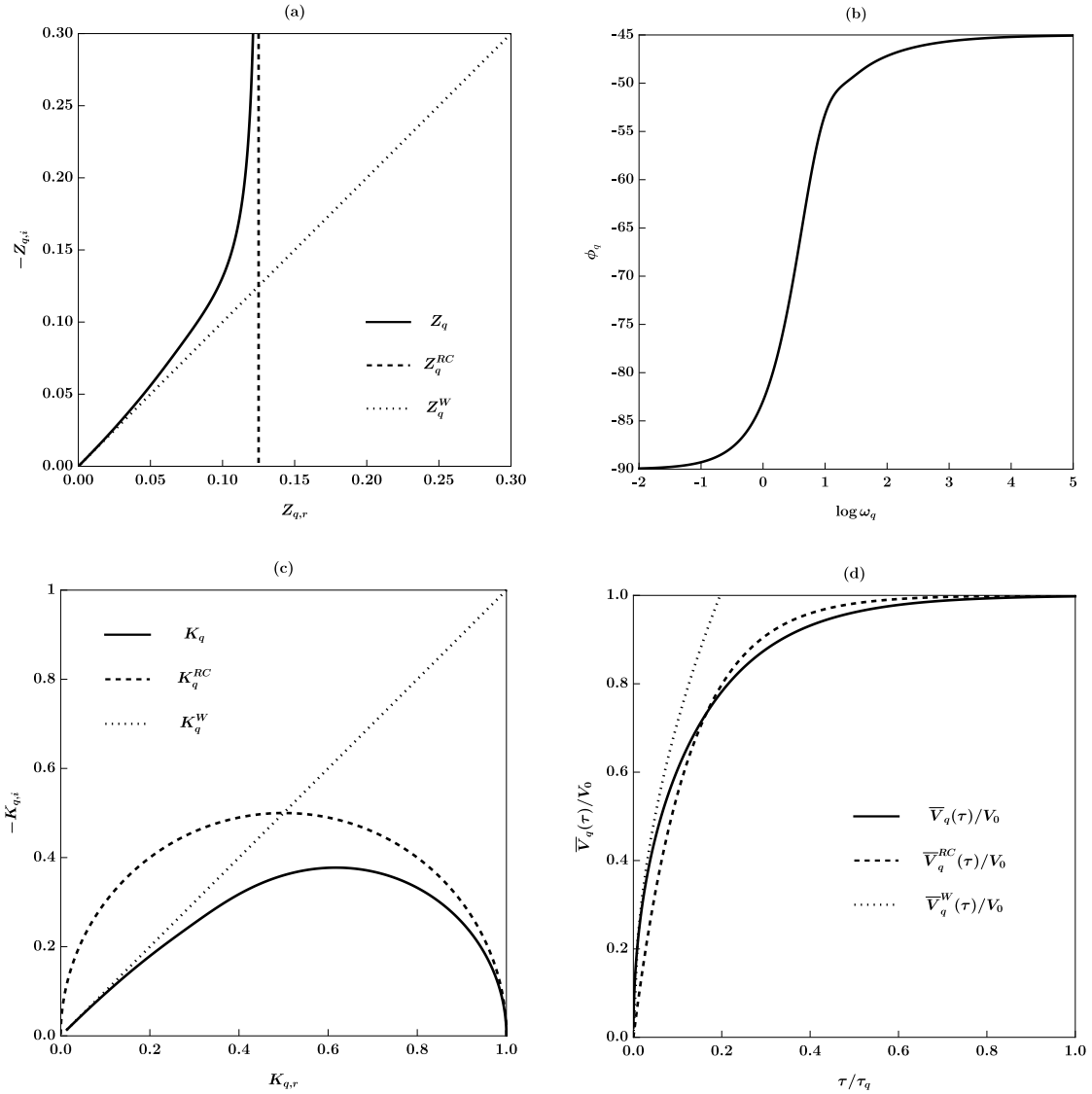
### 3.5.1 Frequency Response of the Graphene Disk Electrode

Fig. 3.7 illustrates the frequency-dependent impedance characteristics of the graphene disk electrode, as described by Eq. (3.22), where the normalized impedance is expressed as  $Z_q(\omega_q) \equiv Z_{q,r}(\omega_q) + iZ_{q,i}(\omega_q)$ , with  $Z_{q,r}$  and  $Z_{q,i}$  denoting the real and imaginary parts, respectively. The Nyquist plot in Fig. 3.7(a), shown with solid lines, depicts the impedance response obtained from spectroscopy, while the corresponding phase angle, defined as  $\phi_q = \arctan(Z_{q,i}/Z_{q,r})$ , is presented in Fig. 3.7(b).

In addition to the full impedance response  $Z_q(\omega_q)$ , the plots in Fig. 3.7 also include the two asymptotic forms corresponding to the limiting cases of the graphene electrode. Specifically, the high-frequency limit is represented by  $Z_q^W(\omega_q) = \frac{1}{2\sqrt{i\omega_q}}$ , and the low-frequency limit by  $Z_q^{RC}(\omega_q) = \frac{1}{8} + \frac{1}{i\omega_q}$ . The former exhibits characteristic Warburg behavior at high frequencies and is indicated by the dotted curve in Fig. 3.7(a). As shown in the corresponding phase plot in Fig. 3.7(b), the phase angle approaches  $\phi_q \rightarrow -45^\circ$  in this regime, consistent with the expected Warburg response. At low frequencies, the impedance behaves as that of a simple RC circuit—i.e., a resistor and capacitor in series—represented by the dashed curve in Fig. 3.7(a). This interpretation is further supported by the phase plot in Fig. 3.7(b), where the phase angle tends toward  $\phi_q \rightarrow -90^\circ$ , indicating dominant capacitive behavior.

The quantum time scale  $\tau_q = \mathcal{R}_q \mathcal{C}_q$ , introduced in Eq. (3.21), serves as a key parameter for analyzing time-dependent quantum electrodynamic effects within the framework of quantum rate theory (QRT), as highlighted in recent studies by Bueno *et al.* [73, 75, 74]. Within this theoretical context, the resistive ( $\mathcal{R}_q$ ) and capacitive ( $\mathcal{C}_q$ ) components of graphene, connected in series, effectively constitute a low-frequency RC circuit whose behavior is governed by quantum mechanical principles. To explore this further, we consider the complex capacitance of the graphene electrode,  $K_q(\omega_q)$ , expressed in dimensionless form in Eq. (3.24), where the substitution  $S\tau_q \mapsto i\omega_q$  is made with  $\omega_q = \Omega\tau_q$ . Fig. 3.7(c) presents the Nyquist plot for  $K_q(\omega_q) \equiv K_{q,r}(\omega_q) + iK_{q,i}(\omega_q)$ , shown with solid lines. In addition to the full expression for  $K_q(\omega_q)$ , the figure also includes the asymptotic behaviors in the high- and low-frequency regimes. The high-frequency limit,  $K_q^W(\omega_q) = 2/\sqrt{i\omega_q}$ , is represented by the dotted line in Fig. 3.7(c), which appears as a straight line with a 45° slope, indicative of Warburg-type behavior. Conversely, the low-frequency limit,  $K_q^{RC}(\omega_q) = 1/(1 + i\omega_q/8)$ , gives rise to a semicircular arc in the Nyquist plane, shown as a dashed line, reflecting the classical RC response. This low-frequency signature corroborates the RC interpretation emphasized by Bueno *et al.*

The time-dependent response of the surface-averaged potential drop across graphene,  $\bar{V}_q(\tau)$ , to a step-like voltage input  $V_c(\tau) = V_0 H(\tau)$  is obtained by performing the inverse Laplace transform of Eq. (3.23), where  $V_c(S) = V_0/S$ . The results are shown in Fig. 3.7(d) as a function of the dimensionless time variable  $t_q = \tau/\tau_q$ . In this plot, the solid curve represents the general solution computed using the full expression for  $K_q(S)$  from Eq. (3.24), and is compared to the asymptotic behaviors associated with the high- and low-frequency limits of the GE response—namely, the Warburg and RC-circuit regimes. In the Warburg limit, the normalized complex capacitance reduces to  $K_q^W(S) = 2/\sqrt{S\tau_q}$ , whose inverse Laplace transform yields the early-time response  $\bar{V}_q^W(\tau) = 4V_0\sqrt{t_q/\pi}$ . This approximation effectively captures the short-time dynamics ( $t_q \ll 1$ ), as indicated by the dotted curve. In contrast, the RC-circuit regime corresponds to the low-frequency limit where  $K_q^{RC}(S) = 1/(1 + S\tau_q/8)$ , which transforms to the time-domain expression  $\bar{V}_q^{RC}(\tau) = V_0 [1 - \exp(-8t_q)]$ . This result describes the long-time behavior ( $t_q \gtrsim 1$ ) with good accuracy, as illustrated by the dashed curve.



**Figure 3.7:** Frequency response of the graphene disk electrode. (a) Impedance Nyquist plot. The dashed curve corresponds to the low-frequency limit, representing capacitive (RC) behavior, while the dotted curve illustrates the high-frequency Warburg response. (b) Phase angle of the graphene disk impedance as a function of frequency. (c) Nyquist plot of the normalized complex capacitance. The dashed semicircle denotes the RC-like response in the low-frequency regime, as characterized by Bueno *et al.*, while the dotted line represents the high-frequency Warburg behavior. (d) Time-domain response of the surface-averaged potential drop across graphene to a step-like input. The dashed curve captures the long-time dynamics consistent with low-frequency RC-circuit behavior, whereas the dotted curve depicts the early-time response associated with high-frequency Warburg behavior.

### 3.5.2 Frequency Response of the Graphene/Electrolyte Interface

The parameters adopted for the calculations in this section correspond to an aqueous electrolyte at room temperature. The dielectric constant of the bulk electrolyte is taken as  $\epsilon_b \approx 80 \epsilon_0$ , where  $\epsilon_0 \approx 8.85 \times 10^{-12}$  F/m denotes the vacuum permittivity. The bulk ionic concentration,  $c_b$ , is given in molarity ( $M \equiv \text{mol/L}$ ). To explicitly reveal the dependence on concentration, the Debye length is defined as  $\lambda_D = \lambda_{1M}/\sqrt{c_b}$ , where  $\lambda_{1M} \approx 0.3$  nm denotes the Debye length at  $c_b = 1M$ . The corresponding Debye capacitance is given by  $C_D \approx 229\sqrt{c_b} \mu\text{F}/\text{cm}^2$ , while the quantum capacitance of neutral graphene at room temperature is approximated as  $C_q \approx 0.8 \mu\text{F}/\text{cm}^2$ , yielding  $C_q^{-1} \approx 287.5\sqrt{c_b}$ . The length of the electrochemical cell is set to  $L = 0.1$  mm. For a representative aqueous solution, the diffusion coefficient is taken as  $D = 10^{-6}$  cm<sup>2</sup>/sec. This leads to a scaled frequency  $\omega = \hat{\omega}/c_b$ , where  $\hat{\omega} = (\lambda_{1M}^2/D)\Omega$  and  $\lambda_{1M}^2/D \approx 0.9$  nsec defines the characteristic Debye time. Consequently, the dimensionless frequency is expressed as  $s = i\hat{\omega}/c_b$ . Additionally, the DC resistance of the bulk electrolyte is given by  $\mathcal{R}_b = \mathcal{R}_{1M}/c_b$ , with  $\mathcal{R}_{1M} = L \lambda_{1M}^2 / (\epsilon_b DA)$ .

#### Effects of the Ion Concentrations

Fig. 3.8 presents the frequency-dependent impedance behavior of the graphene disk electrode across a range of ionic concentrations, spanning from  $10^{-5}$  M to  $10^{-1}$  M. Two distinct cases are examined: (1) graphene possessing finite conductivity, illustrated by solid lines, and (2) the idealized case of infinite graphene conductivity, represented by dashed lines. In the latter scenario, the impedance simplifies to  $\mathcal{Z}_q(\Omega) = 1/(i\Omega C_q)$ , implying that the complex capacitance function in Eq. (3.24) reduces to  $K_q(S) = 1$ , and consequently, the function  $\Gamma(s)$  in Eq. (3.48) becomes a constant,  $\Gamma = 1/C_q$ , consistent with the model used in Section 3.2. To mitigate edge-related artifacts, the radius of the electrode is set to 1 mm for all calculations. Additionally, the contact resistance is neglected by setting  $R_c = 0$  in Eq. (3.54), since the impact of the external circuitry will be analyzed separately in the subsequent discussion.

Fig. 3.8(a) displays the Nyquist plots for the specified range of ion concentrations. For the case of infinite graphene conductivity (dashed curves shown in the inset), the impedance response shows negligible sensitivity to changes in ion concentration. In contrast, when finite conductivity is considered (solid curves), the impedance exhibits a marked dependence on the ion concentration, particularly as it increases. In both scenarios, a capacitive response is evident at low frequencies. However, in the high-frequency regime—near the origin—the behavior diverges: while the infinite conductivity case remains essentially

unchanged, the finite conductivity case shows noticeable variation with increasing ion concentration. To expose compatibility with experimental and practical observations, we also adopt a cut-off frequency of  $\Omega_c/(2\pi) = 1$  MHz, below which EIS is applicable, giving the corresponding scaled cut-off frequency of  $\hat{\omega}_c \approx 5.65 \times 10^{-3}$ . The bullets on the Nyquist curves in Fig. 3.8(a) indicate the values of the real and imaginary parts of the impedance at the cut-off frequency, such that only the parts of those curves that lie to the right of the bullets should be accessible in EIS. One sees in this figure a large spread of the bullets, indicating that the range of the observable impedance values in EIS can be severely reduced at high ion concentrations.

Fig. 3.8(b) and Fig. 3.8(c) present the phase angle  $\phi = \arctan(Z_i/Z_r)$  and magnitude  $|Z| = \sqrt{Z_r^2 + Z_i^2}$  of the impedance, respectively, for varying ion concentrations. In the low-frequency regime, both conductivity scenarios exhibit a phase angle approaching  $\phi \rightarrow -90^\circ$ , consistent with dominant capacitive behavior. This observation is supported by the magnitude plot in Fig. 3.8(c), where the slope tends toward unity, a characteristic feature of capacitive impedance. At high frequencies, the cases diverge: for finite graphene conductivity (solid curves), the phase transitions to  $\phi \rightarrow -45^\circ$ , reflecting Warburg-like behavior, which is further corroborated by the slope of  $-1/2$  in the magnitude plot. In contrast, assuming infinite conductivity (dashed curves), the phase flattens to  $\phi \rightarrow 0$ , indicating a transition to resistive behavior that is largely insensitive to ion concentration. Across both conductivity assumptions, the response consistently shifts toward capacitive characteristics (i.e.,  $\phi \rightarrow -90^\circ$ ) as the frequency and ion concentration decrease. The shaded vertical bars in both figures indicate a region around the cut-off frequency below which EIS is applicable.

The preceding analysis can be further elucidated by exploring asymptotic limits. In the low-frequency regime, taking the limit  $s \rightarrow 0$ , Eq. (3.48) simplifies to  $\Gamma(s) \rightarrow C_q^{-1}$ . Inserting this into the impedance expression in Eq. (3.54) and expanding in powers of  $s$  yields the low-frequency approximation  $Z_{\text{LF}} \sim R + 1/(s C_{\text{LF}})$ , which corresponds to the classical form of a series RC circuit. Here, the effective resistance is given by  $R = \ell + (\ell/2) \text{sech}^2(\ell/2) - 3 \tanh(\ell/2)$ , while the low-frequency capacitance is  $C_{\text{LF}} = [C_q^{-1} + 2 \tanh(\ell/2)]^{-1}$ . In the asymptotic limit  $\ell \gg 1$ , these expressions simplify to  $R \approx \ell$  and  $C_{\text{LF}} \approx (C_q^{-1} + 2)^{-1}$ . When translated into dimensional units, the low-frequency capacitance becomes  $C_{\text{LF}} = (C_q^{-1} + 2C_D^{-1})^{-1}$ , reflecting the effective series combination of the quantum capacitance of graphene,  $C_q$ , with two Debye layers of capacitance  $C_D$ , one at each electrode interface.

In the high-frequency regime, taking the limit  $s \rightarrow i\infty$ , the expression in Eq. (3.48) asymptotically approaches  $\Gamma(s) \rightarrow \frac{\gamma(s)}{2C_q}$ . Substituting this into Eq. (3.54) gives the leading-

order impedance behavior as  $Z_{\text{HF}} \sim 1/(s C_{\text{HF}})$ , where the effective high-frequency capacitance is  $C_{\text{HF}}(s) = \left(\frac{\gamma(s)}{2C_q} + \ell\right)^{-1}$ . In the asymptotic limit  $s \rightarrow i\infty$  or equivalently  $\gamma(s) \rightarrow \infty$ , the high-frequency capacitance is approximated by  $C_{\text{HF}}(s) \approx 2C_q/\gamma(s)$ . Expressed in physical units, this corresponds to a high-frequency capacitance of  $\mathcal{C}_{\text{HF}}(\Omega) \approx 2\mathcal{C}_q/(a\zeta(\Omega))$ .

To complete the characterization, capacitance spectroscopy is examined using the complex capacitance defined by  $C(s) = 1/(sZ(s)) \equiv C_r + iC_i$ , as depicted in Fig. 3.8(d). In both conductivity scenarios, increasing the bulk ion concentration leads to a rise in the real component of the capacitance,  $\overline{C}_r$ , and causes the overall spectrum to shift rightward on the frequency axis. This trend highlights the enhanced charge storage capability at higher electrolyte concentrations. The bullet points correspond to the cut-off frequency, suggesting that the parts of the curves in Fig. 3.8(d) lying to the right of those points should be accessible by ECS. Unlike Fig. 3.8(a), one can see in Fig. 3.8(d) that the bullets are clustered close to the origin, indicating that the most part of the Nyquist curves for the complex capacitance may be observed in ECS at all ion concentrations.

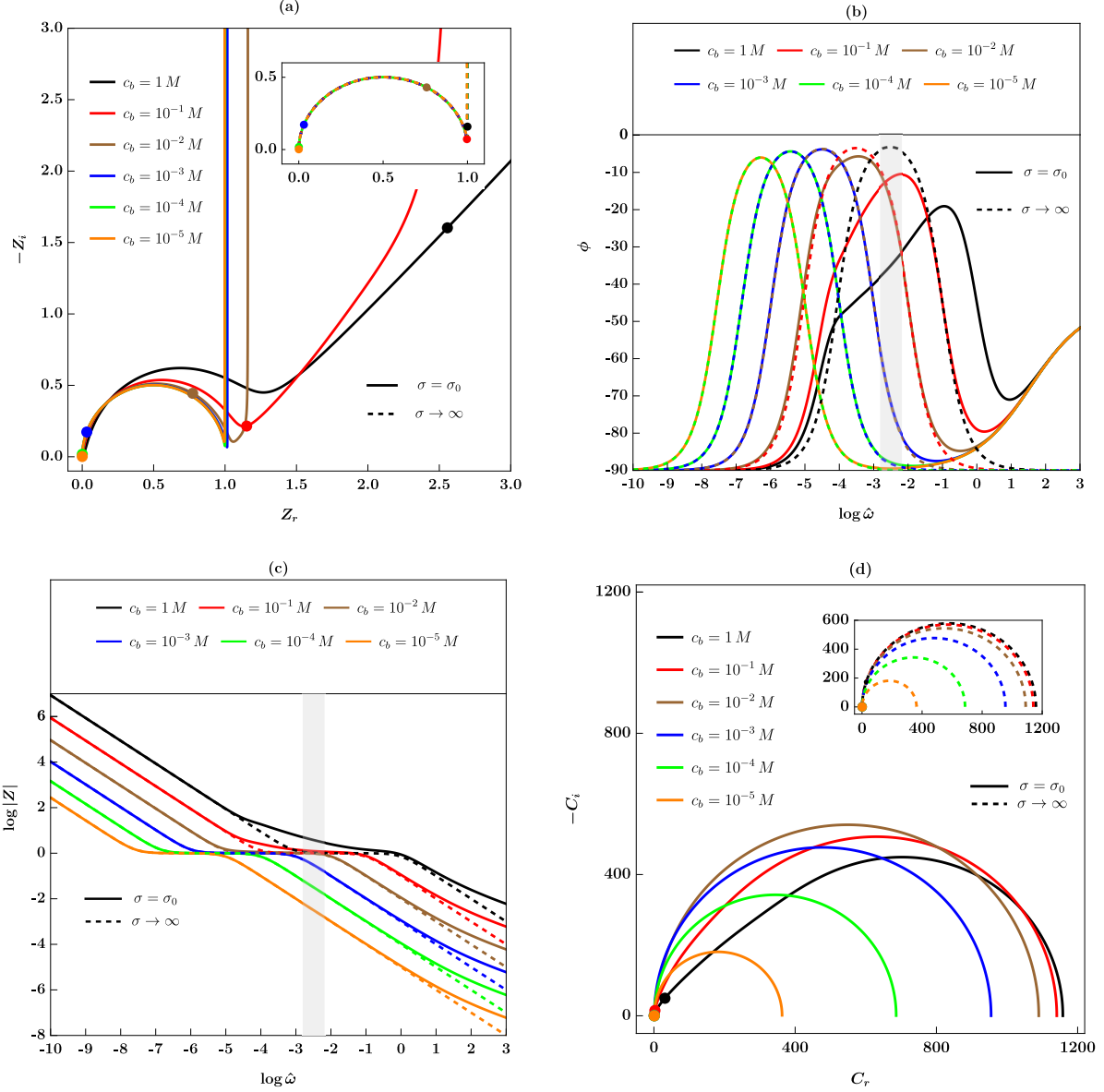


**Figure 3.8:** Effects of ion concentration on the frequency response of the GE/electrolyte interface when  $a = 1$  mm and  $R_c = 0$ . Solid curves represent finite graphene conductivity, while dashed curves indicate infinite conductivity. (a) Impedance Nyquist plot. (b, c) Bode plots. (d) Capacitive Nyquist plot. The bullet points in (a) and (d), together with the shaded areas in (b) and (c), indicate the cut-off frequency  $\hat{\omega}_c$  below which EIS and ECS are applicable.

## Effects of the Electrode Area

The influence of electrode area on the frequency response of the GE/electrolyte interface is examined by varying the electrode radius while keeping the ion concentration fixed at  $c_b = 10^{-2}$  M, as shown in Fig. 3.9. The impact of the external circuitry is excluded by setting  $R_c = 0$ .

Fig. 3.9(a) presents the Nyquist plot, where notable shifts are observed in the impedance spectra for the finite conductivity case (solid lines) as the electrode radius increases. In contrast, the infinite conductivity scenario (dashed lines shown in the inset) shows minimal sensitivity to changes in radius. The positions of the bullets in this figure, which correspond to the cut-off frequency, suggest that the portions of the Nyquist curves for impedance that are observable in EIS is not strongly influenced by the graphene electrode radius.

This trend is further highlighted in the Bode plots of Fig. 3.9(b) and Fig. 3.9(c), where the finite conductivity case exhibits enhanced frequency sensitivity with increasing radius—particularly in the high-frequency regime. The infinite conductivity response, however, remains nearly invariant across the same range. Despite these differences, the overall qualitative behavior is preserved in both cases: capacitive characteristics dominate at low frequencies, while Warburg-type features emerge at high frequencies for finite conductivity, and purely capacitive behavior persists under infinite conductivity. The shaded bars in both figures denote the cut-off frequency below which EIS is applicable.

The dependency on electrode area is also reflected in the capacitive Nyquist plots of Fig. 3.9(d), where the finite conductivity case reveals moderate variation with radius, whereas the infinite conductivity case remains largely unchanged. Similar to Fig. 3.8(d), one sees in Fig. 3.9(d) that the bullets corresponding to the cut-off frequency are clustered close to the origin, indicating that the most parts of the Nyquist curves for the complex capacitance are observable in ECS for all electrode radii.

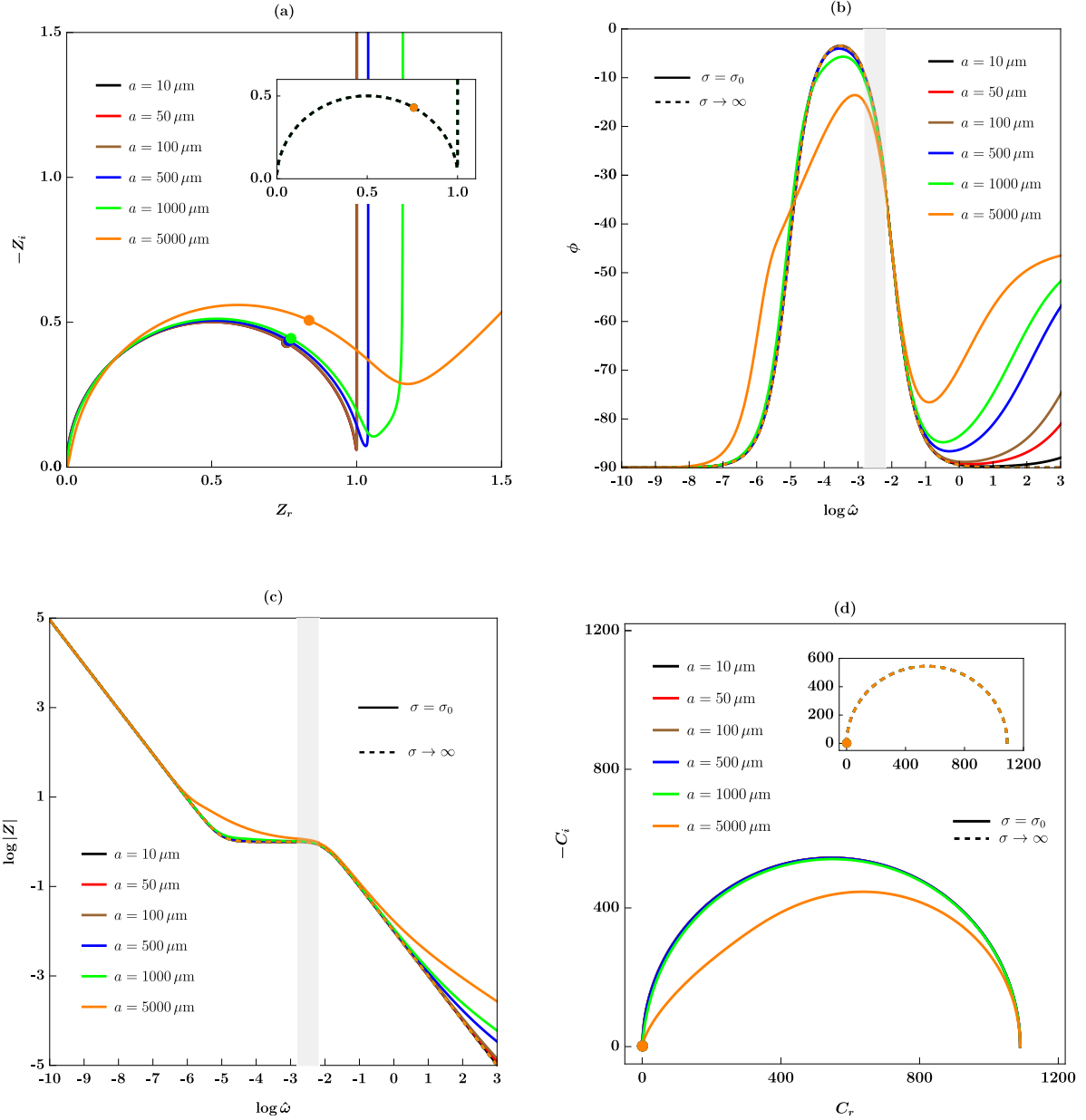


**Figure 3.9:** Effects of electrode area on the frequency response of the GE/electrolyte interface when  $c_b = 10^{-2}$  M and  $R_c = 0$ . Solid curves represent finite graphene conductivity, while dashed curves indicate infinite conductivity. (a) Impedance Nyquist plot. (b, c) Bode plots. (d) Capacitive Nyquist plot. The bullet points in (a) and (d) along with the shaded area in (b, c) refer to the cut-off frequency  $\hat{\omega}_c$  below which the EIS and ECS are applicable.

## Effects of the Contact Resistance

We investigate the influence of contact resistance on the frequency response of the GE/electrolyte interface by varying the contact resistance  $R_c$ , while keeping the ion concentration and electrode radius fixed at  $c_b = 10^{-2}$  M and  $a = 1$  mm, respectively, as illustrated in Fig. 3.10.

Fig. 3.10(a) presents the Nyquist plots for both finite and infinite graphene conductivity under varying values of  $R_c$ . At low frequencies, the impedance curves remain unaffected by  $R_c$  in both cases, consistently displaying capacitive behavior. In the high-frequency regime, however, increasing  $R_c$  leads to a noticeable increase in the real part of the impedance,  $Z_r$ , for both conductivity cases. This trend is further supported by the Bode plots in Figs. 3.10(b) and 3.10(c). Specifically, Fig. 3.10(b) shows that at low frequencies, the phase angle tends toward  $-90^\circ$ , and Fig. 3.10(c) exhibits a log-log slope of unity, confirming capacitive dominance independent of  $R_c$ . At higher frequencies, increasing  $R_c$  drives the phase angle toward  $0^\circ$  in Fig. 3.10(b), indicating a transition to resistive behavior. This is corroborated in Fig. 3.10(c), where the slope of the magnitude plot flattens, further emphasizing resistive dominance. The applicability of EIS is also depicted in the Nyquist plot in Fig. 3.10(a), where the cut-off frequencies for the finite and infinite conductivity (inset) cases are marked by bullet points. In the Bode plots shown in Figs. 3.10(b) and 3.10(c), a range of the maximum frequencies accessible in the EIS is indicated by the shaded bars surrounding the cut-off frequency.

The capacitive Nyquist plot in Fig. 3.10(d) completes the analysis. For both conductivity cases, the real part of the capacitance,  $C_r$ , remains relatively insensitive to  $R_c$ , demonstrating a robust capacitive response across all frequencies. The cut-off frequency, indicated by bullet points, marks the regime below which ECS is applicable. As illustrated in Fig. 3.10(d), the influence of contact resistance  $R_c$  on the cut-off frequency is minimal. For the given values of  $R_c$ , the bullet points for both finite and infinite conductivities remain clustered at high frequencies.

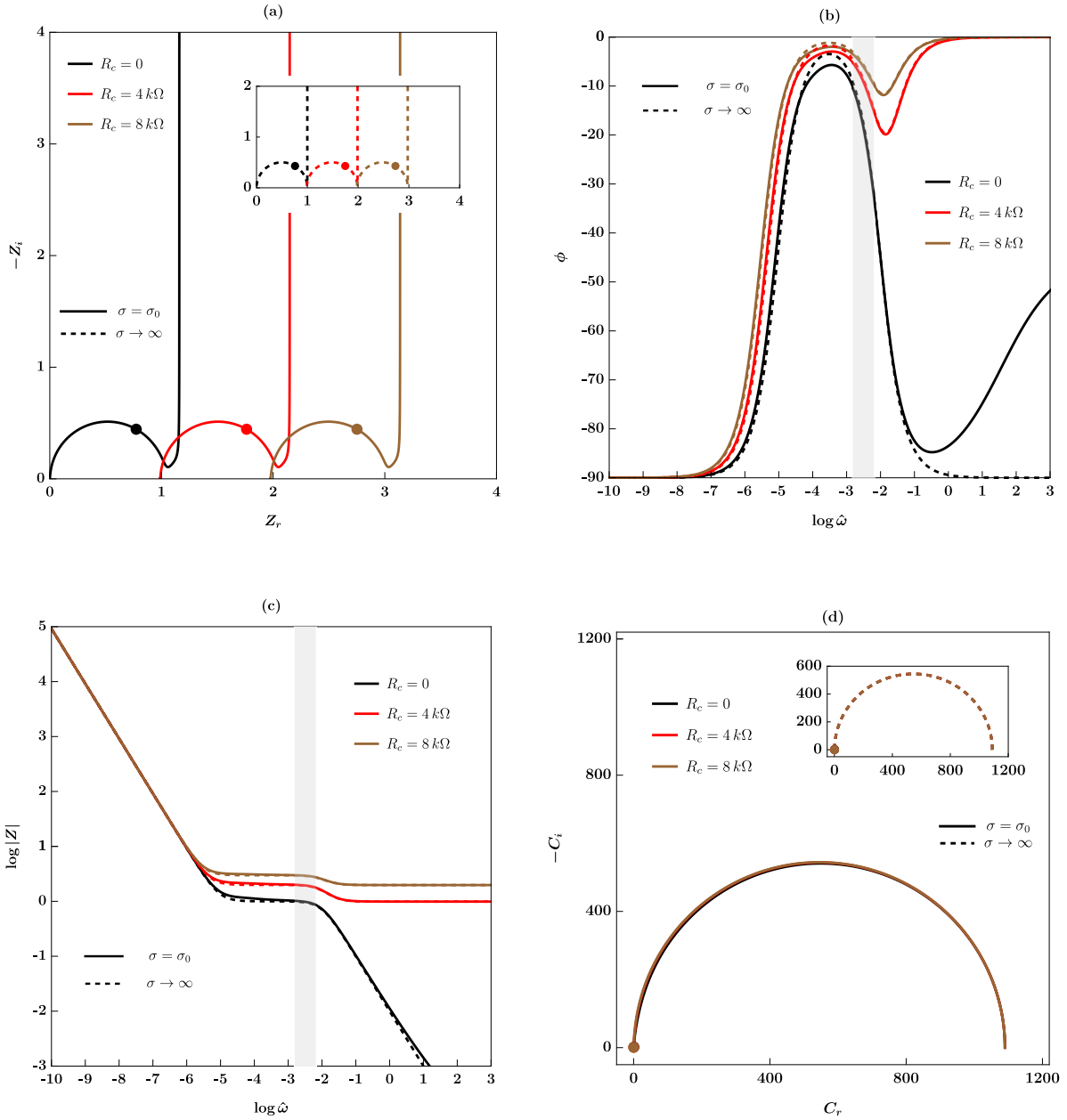


**Figure 3.10:** Effects of contact resistance on the frequency response of the GE/electrolyte interface when  $c_b = 10^{-2} \text{ M}$  and  $a = 1 \text{ mm}$ . Solid curves represent finite graphene conductivity, while dashed curves indicate infinite conductivity. (a) Impedance Nyquist plot. (b, c) Bode plots. (d) Capacitive Nyquist plot. The bullet points in (a) and (d) along with the shaded area in (b, c) refer to the cut-off frequency  $\hat{\omega}_c$  below which the EIS and ECS are applicable.

## 3.6 Concluding Remarks

In this chapter, we examined the frequency response of the graphene/electrolyte interface in dilute electrolytes under two distinct scenarios: (1) neutral graphene with infinite conductivity and (2) neutral graphene with finite conductivity.

In the first case, we derived an analytical expression for the impedance of an electrochemical cell incorporating a graphene electrode. Starting from the linearized Poisson–Nernst–Planck (PNP) equations and appropriate boundary conditions at the graphene interface, the system was nondimensionalized and solved using Laplace transform techniques. A comparative analysis of the impedance behavior for graphene–metal (GM) and metal–metal (MM) electrode configurations was performed across a wide range of frequencies and ion concentrations. In terms of sensitivity to changes in ion concentration, the MM configuration demonstrated greater responsiveness—particularly at low frequencies and higher ionic strengths. Also, we confirmed that the quantum capacitance of graphene can be reliably extracted from the zero-frequency intercept of the real axis in the Nyquist plot of the equivalent cell capacitance. At low frequencies, this total capacitance is typically dominated by the quantum capacitance of the graphene electrode.

In the second case, we explored the frequency-dependent behavior of a graphene disk electrode (GE) in contact with an electrolyte within a three-dimensional geometry. Initially, the GE was modeled as an isolated circular interface. Departing from traditional phenomenological models involving distributed circuit elements, we incorporated the finite quantum conductivity of graphene based on its intrinsic quantum-mechanical properties. This formulation allowed us to derive an analytical expression for the quantum surface impedance of the GE. We then investigated charge relaxation dynamics under two regimes. In the fast-charging regime—associated with low conductivity and/or large quantum capacitance—the system exhibited Warburg-type impedance, characteristic of one-dimensional diffusion across a length scale  $a$ . In contrast, the slow-charging regime—associated with high conductivity and/or small quantum capacitance—displayed a behavior consistent with a classical RC circuit. This distinction connects our analysis to the framework of quantum rate theory (QRT), particularly via the quantum time scale defined in Eq. (3.21). To further elucidate relaxation dynamics, we analyzed the time evolution of the average potential drop across graphene,  $\bar{V}_q(\tau)$ , and demonstrated that its early-time behavior aligns with the Warburg regime, while its late-time behavior corresponds to the RC-circuit limit.

To couple the GE with the surrounding electrolyte, we independently analyzed the electrolyte domain. Assuming the Debye length is much smaller than the electrode radius, we neglected fringing electric fields near the boundary, thereby justifying a reduction to a one-dimensional model through surface averaging and Hankel transform techniques. With the surface-averaged charge density and potential on graphene already established, this approximation enabled a natural extension of the theory previously developed for the infinite-conductivity case. We subsequently established the GE/electrolyte interface by coupling the two domains and deriving a new boundary condition that complements those from the electrolyte analysis, ensuring a well-posed formulation. This enabled us to obtain a closed-form expression for the total electrochemical impedance of the GE/electrolyte interface, which captures the influence of frequency, ion concentration, electrode area, and contact resistance for both finite and infinite graphene conductivity.

The frequency response analysis under varying ion concentrations revealed that both finite and infinite conductivity cases share capacitive behavior in the low-frequency regime. However, in the high-frequency regime, only the finite conductivity case exhibited clear Warburg characteristics, as evidenced by a phase angle tending toward  $-45^\circ$ , a slope of  $-1/2$  in the impedance magnitude.

We then investigated the effect of electrode radius. In the low-frequency regime, we confirmed dominant capacitive behavior regardless of radius. At higher frequencies, however, the finite conductivity case exhibited pronounced sensitivity to changes in electrode size, with larger radii amplifying the deviations from ideal capacitive behavior, thereby highlighting the role of spatial charge redistribution dynamics.

Lastly, we assessed the influence of contact resistance. In both conductivity scenarios, the real component of the capacitance,  $C_r$ , shows minimal dependence on  $R_c$ , indicating a stable capacitive behavior over the entire frequency range.

We have also introduced the cut-off frequency below which EIS and ECS are applicable to relevant experiments and applications. This cut-off frequency, indicated by bullet points in the Nyquist plots and by shaded vertical bars in the Bode plots, corresponds to the scaled frequency of  $\hat{\omega}_c \approx 5.65 \times 10^{-3}$ , or equivalently,  $\Omega_c/2\pi \approx 1$  MHz in physical units. We have nevertheless also displayed our results at frequencies that exceed the cut-off frequency, mostly for academic interest to expose possible effects of the Warburg-type behavior of the graphene electrode at high frequencies.

# Chapter 4

## Charged Graphene in Dilute Electrolytes\*

### 4.1 Introduction

To extend our previous chapter, which examined the frequency response of a neutral graphene electrode at the Debye relaxation time scale—we now explore the behavior of a charged graphene electrode in equilibrium, where the dynamics of diffuse-layer charging are governed by the charging relaxation time scale. To this end, we carry out a leading-order asymptotic analysis within the framework of matched asymptotic expansions, yielding analytical expressions for both the static potential distribution and the time-dependent diffuse-charge dynamics in the electric double layer (EDL), under the influence of a finite DC bias and a small AC perturbation applied to the cell. Furthermore, the model incorporates more realistic boundary conditions by accounting for the Stern layers, which represent the interaction between the diffuse and compact layers, and by incorporating the appropriate boundary condition for a single-layer graphene electrode. We note that for bilayer or multilayer graphene electrodes, additional complexities arise in defining the quantum capacitance [113], due to notable alterations in the density of states (DOS) [114, 115] and layer-specific doping effects induced by metallic contacts (not by ion or solvent adsorption) [3, 116, 117]. These effects would necessitate a more sophisticated boundary condition than the one employed in our single-layer model and are therefore beyond the

---

<sup>1</sup>\*The material presented in this chapter has been published in the *Journal of The Electrochemical Society* (M. Yavarian et al., 2024) [112].

scope of this study.

## 4.2 Theory

The electrochemical cell considered in this chapter consists of a symmetric monovalent binary electrolyte, comprising two ionic species with identical diffusion coefficients  $D_+ = D_- = D$ , equal mobilities  $\mu_+ = \mu_- = \mu$ , and the same equilibrium bulk concentration  $c_b$ . A schematic of this one-dimensional setup is presented in Fig. 4.1, which shows the system along the  $X$  axis. In this configuration, the graphene electrode (GE) is placed at  $X = -L$  and the metal electrode (ME) at  $X = L$ , with each electrode separated from the electrolyte by a charge-free Stern layer of thickness  $h$ . We assume that both electrodes behave as blocking, thereby excluding specific ion adsorption and neglecting Faradaic reactions within the Stern layers. As a result, the region accessible to ions is bounded by the outer Helmholtz planes (OHPs) located at  $X = \pm H = \pm L \mp h$ , where we impose zero-flux boundary conditions for the ions. To emphasize the electrostatic role of the graphene electrode, we deliberately idealize the model by treating the metal electrode as having infinite quantum capacitance—effectively modeling it as an ideal metal—while disregarding heterogeneity and atomic-scale features. This simplification is motivated by the assumption that the density of electronic states (DOS) in a typical metal is sufficiently high that any excess surface charge does not lead to a measurable shift in its Fermi level [51]. Thus, the electronic contribution of the ME is considered negligible, and its charging is entirely governed by the potential drop across the ionic electrolyte. Additionally, our model neglects any potential offsets that may arise from differences in the work functions or electron affinities between dissimilar materials, such as between graphene and the metal contact used for charging the graphene electrode.

When a time-dependent external voltage  $V(\tau)$  is applied across the electrochemical cell, it induces an electrostatic potential  $\Phi(X, \tau)$  with a spatial profile depicted in Fig. 4.1, which also highlights the individual potential drops across different regions. In this figure,  $V_q(\tau)$  represents the potential drop within the graphene, associated with its Fermi level and responsible for modulating its doping. The quantities  $V_S^g(\tau) = \Phi(-H, \tau) - \Phi(-L, \tau)$  and  $V_S^m(\tau) = \Phi(L, \tau) - \Phi(H, \tau)$  denote the potential drops across the Stern layers adjacent to the graphene electrode (GE, superscript “ $g$ ”) and the metal electrode (ME, superscript “ $m$ ”), respectively. Here,  $\Phi(\mp L, \tau)$  corresponds to the potential at the location of the GE/ME, while  $\Phi(\mp H, \tau)$  refers to the potential at the outer Helmholtz planes (OHPs), i.e., the boundaries between the Stern layers and the electrolyte region. The potential drop across the ionic region of the electrolyte is thus defined as  $V_{el}(\tau) = \Phi(H, \tau) - \Phi(-H, \tau)$ .

Putting all contributions together, the total applied potential between the ME and GE is given by  $V(\tau) = V_q(\tau) + V_S^g(\tau) + V_S^m(\tau) + V_{el}(\tau)$  as also illustrated in Fig. 4.1.

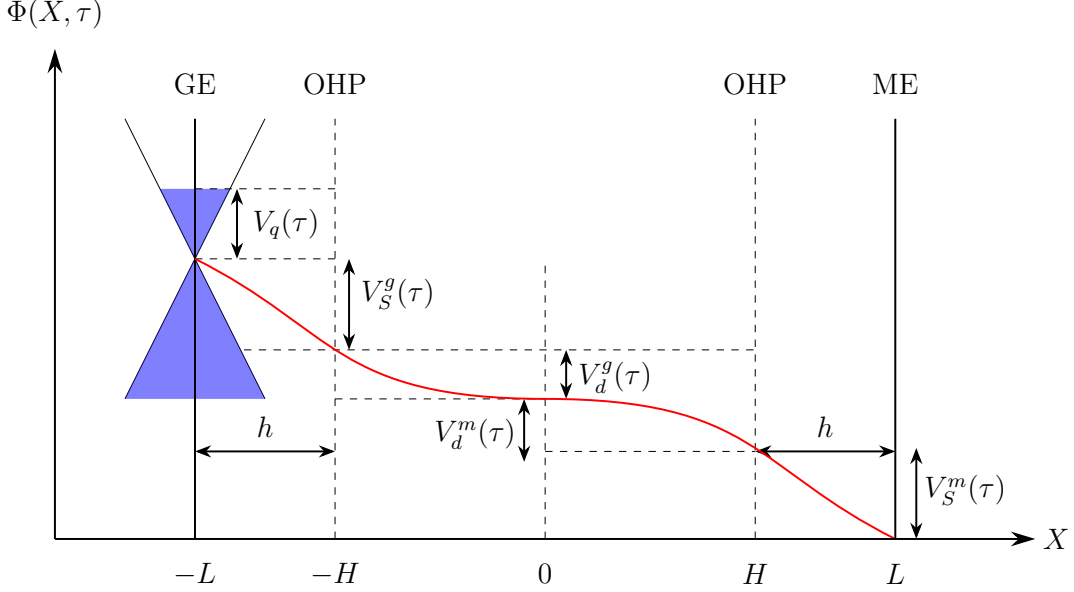


**Figure 4.1:** Schematic representation of the electrochemical cell comprising the graphene electrode (GE) and the metal electrode (ME), with the electrolyte confined between two outer Helmholtz planes (OHPs) positioned near each electrode. In response to a time-dependent applied voltage  $V(\tau)$ , the resulting electrostatic potential distribution  $\Phi(X, \tau)$  is shown, including the internal potential drop  $V_q(\tau)$  associated with the doping of graphene. The potential decreases linearly across the Stern layers, which extend from each electrode surface to its respective OHP, producing the potential drops labeled as  $V_S^g(\tau)$  and  $V_S^m(\tau)$  for the GE and ME sides, respectively. Beyond the Stern layers, the potential continues to decay through the neighboring diffuse layers until it reaches a uniform value in the bulk electrolyte. The potential drops across these diffuse regions are denoted by  $V_d^g(\tau)$  and  $V_d^m(\tau)$ .

### 4.2.1 PNP Model

The PNP equations given in Eq. (2.18) are to be solved over the spatial domain  $-H < X < H$ , subject to the relevant boundary conditions. In addition to the zero-flux boundary conditions for the ionic concentrations at the outer Helmholtz planes (OHPs), expressed as  $F_{\pm}(\pm H, \tau) = 0$ , two additional boundary conditions are needed for the electrostatic potential, incorporating the effect of Stern layers. Within the Stern layer adjacent to the graphene electrode (GE), the electric field remains constant

$$\left. \frac{\partial \Phi(X, \tau)}{\partial X} \right|_{X=-L^+} = \left. \frac{\partial \Phi(X, \tau)}{\partial X} \right|_{X=-H^-}, \quad (4.1)$$

while the normal component of the electric field remains continuous across the Stern plane

$$\epsilon_S \left. \frac{\partial \Phi(X, \tau)}{\partial X} \right|_{X=-H^-} = \epsilon_b \left. \frac{\partial \Phi(X, \tau)}{\partial X} \right|_{X=-H^+}, \quad (4.2)$$

where  $\epsilon_S$  denotes the dielectric permittivity within the Stern layer. Since the electrostatic potential  $\Phi(X, \tau)$  is continuous throughout the domain, the electric field in the Stern layer can alternatively be expressed in terms of the potential drop across the layer

$$\left. \frac{\partial \Phi(X, \tau)}{\partial X} \right|_{X=-H^-} = \frac{\Phi(-H, \tau) - \Phi(-L, \tau)}{h}, \quad (4.3)$$

which can be substituted into Eq. (4.2) to eliminate the electric field term at  $X = -H^-$ . This leads to a non-homogeneous Robin-type boundary condition for the potential at  $X = -H^+$

$$\Phi(-H, \tau) - \lambda_S \left. \frac{\partial \Phi(X, \tau)}{\partial X} \right|_{X=-H^+} = \Phi(-L, \tau), \quad (4.4)$$

which corresponds to the classical Stern boundary condition, where the parameter  $\lambda_S = h\epsilon_b/\epsilon_S$  defines the effective thickness of the Stern layer.

Applying the same procedure to the Stern layer adjacent to the metal electrode (ME), an analogous boundary condition to Eq. (4.4) can be derived. This yields the following Stern boundary condition for the potential at  $X = H^-$

$$\Phi(H, \tau) + \lambda_S \left. \frac{\partial \Phi(X, \tau)}{\partial X} \right|_{X=H^-} = \Phi(L, \tau). \quad (4.5)$$

To incorporate the effects of the graphene electrode (GE), we recognize that its surface charge density (per unit area) is determined by the instantaneous potential  $V_q(\tau)$  through the Dirac cone approximation, which describes the  $\pi$ -electron bands of graphene:

$$\sigma_g [V_q(\tau)] = en_g \left[ \operatorname{dilog} \left( 1 + \exp \left( \frac{eV_q(\tau)}{k_B T} \right) \right) - \operatorname{dilog} \left( 1 + \exp \left( \frac{-eV_q(\tau)}{k_B T} \right) \right) \right], \quad (4.6)$$

where  $n_g = \frac{2}{\pi} \left( \frac{k_B T}{\hbar u_F} \right)^2 \approx 9.2 \times 10^{-4} \text{ nm}^{-2}$  is the characteristic density of graphene at room temperature. The function  $\text{dilog}$  refers to the standard dilogarithm function [118]. By applying Gauss's law to a pillbox volume enclosing the graphene electrode, we obtain the following condition

$$-\epsilon_S \frac{\partial \Phi(X, \tau)}{\partial X} \Big|_{X=-L^+} = \sigma_g [V_q(\tau)]. \quad (4.7)$$

Utilizing this relation, we can reformulate the Stern boundary condition at the GE interface from Eq. (4.4) in one of two equivalent ways. First, as a non-homogeneous Neumann boundary condition applied at  $X = -H^+$ :

$$-\epsilon_b \frac{\partial \Phi(X, \tau)}{\partial X} \Big|_{X=-H^+} = \sigma_g [V_q(\tau)], \quad (4.8)$$

or alternatively, as a non-homogeneous Dirichlet boundary condition at  $X = -H$

$$\Phi(-H, \tau) = \Phi(-L, \tau) - \frac{\sigma_g [V_q(\tau)]}{\mathcal{C}_S}, \quad (4.9)$$

where  $\mathcal{C}_S = \epsilon_S/h$  represents the capacitance per unit area of the Stern layer. It is worth noting that the pillbox approach described in Eqs. (4.7) and (4.8) is based on the classical Gouy–Chapman–Stern (GCS) theory, which links the electrostatic potential at the outer Helmholtz plane (OHP) to the potential within the diffuse layer. For a refined version of GCS theory that incorporates finite spillover of electron density resembling a jellium model at the electrode/electrolyte interface, a comprehensive discussion is available in the work by Kant et al. [119].

The boundary conditions outlined above do not, by themselves, guarantee uniqueness of the solution unless overall charge conservation is enforced in the system. To ensure that the present PNP model is well-posed and fully specified, an additional constraint must be introduced. This can be achieved by taking the time derivative of the integrals on both sides of Eq. (2.16) over the interval  $-H \leq X \leq H$ , applying the zero-flux boundary conditions at the outer Helmholtz planes,  $F_{\pm}(\pm H, \tau) = 0$ , and invoking the condition of electroneutrality in the bulk electrolyte. As a result, we obtain the following constraint

$$\int_{-H}^H C_+(X, \tau) dX = \int_{-H}^H C_-(X, \tau) dX = 2Hc_b. \quad (4.10)$$

Furthermore, integrating the Poisson equation, Eq. (2.17), over the region from  $-H^+$  to  $H^-$  yields a Gauss's law condition for the electrolyte, expressing the continuity of the

electric field across the OHPs

$$\left. \frac{\partial \Phi(X, \tau)}{\partial X} \right|_{X=-H^+} = \left. \frac{\partial \Phi(X, \tau)}{\partial X} \right|_{X=H^-}. \quad (4.11)$$

Together, Eqs. (4.10) and (4.11) confirm that charge is conserved within the system and establish an important coupling between the electrodes. This relationship plays a crucial role in understanding how the electrostatic potential connects the two electrode interfaces.

For simplicity, we will henceforth omit the  $\pm$  superscripts indicating one-sided limits in the boundary conditions, without loss of generality in the forthcoming analysis.

### Dimensionless Formulation

To simplify the analysis, the problem is reformulated using nondimensional (reduced) variables as follows: the spatial coordinate is rescaled as  $x = X/H$ , and the electrode position becomes  $\ell = L/H$ . Time is normalized by defining  $t = \tau/\tau_c$ , where the charging time scale is given by  $\tau_c = \lambda_D H/D$ , with  $\lambda_D$  representing the Debye length. The normalized salt concentration is defined as  $c = (C_+ + C_-)/2c_b$ , and the reduced charge density is  $\rho = (C_+ - C_-)/2c_b$ . The electrostatic potential and the applied voltage are also expressed in reduced form as  $\{\phi, v\} = e/(k_B T)\{\Phi, V\}$ . Surface charge densities are normalized via  $\varsigma = \sigma/(en_d)$ , where  $n_d = (4\pi\lambda_B\lambda_D)^{-1}$  is a characteristic concentration associated with a semi-infinite diffuse layer with  $\lambda_B = e^2/(4\pi\epsilon_b k_B T)$  being the Bjerrum length. With this normalization, all capacitances in the system (per unit area) are rendered dimensionless by scaling with the Debye capacitance,  $C_D = e^2 n_d / (k_B T) \equiv \epsilon_b / \lambda_D$ .

With the reduced variables introduced above, the dimensionless form of the PNP equations, corresponding to Eq. (2.18), becomes for  $-1 < x < 1$ :

$$\frac{\partial c(x, t)}{\partial t} = \varepsilon \frac{\partial}{\partial x} \left[ \frac{\partial c(x, t)}{\partial x} + \rho(x, t) \frac{\partial \phi(x, t)}{\partial x} \right], \quad (4.12a)$$

$$\frac{\partial \rho(x, t)}{\partial t} = \varepsilon \frac{\partial}{\partial x} \left[ \frac{\partial \rho(x, t)}{\partial x} + c(x, t) \frac{\partial \phi(x, t)}{\partial x} \right], \quad (4.12b)$$

$$-\varepsilon^2 \frac{\partial^2 \phi(x, t)}{\partial x^2} = \rho(x, t). \quad (4.12c)$$

In the above formulation, the small dimensionless parameter  $\varepsilon = \lambda_D/H \ll 1$  characterizes the relative thickness of the diffuse layer and forms the basis for the asymptotic analysis employed in this chapter.

The above equations are subject to the following nondimensionalized boundary conditions, which include the zero-flux conditions at the outer Helmholtz planes and the Stern boundary conditions

$$\left[ \frac{\partial c(x, t)}{\partial x} + \rho(x, t) \frac{\partial \phi(x, t)}{\partial x} \right] \Big|_{x=\pm 1} = 0, \quad (4.13a)$$

$$\left[ \frac{\partial \rho(x, t)}{\partial x} + c(x, t) \frac{\partial \phi(x, t)}{\partial x} \right] \Big|_{x=\pm 1} = 0, \quad (4.13b)$$

$$\phi(-1, t) - \varepsilon \alpha \frac{\partial \phi(x, t)}{\partial x} \Big|_{x=-1} = \phi(-\ell, t), \quad (4.13c)$$

$$\phi(1, t) + \varepsilon \alpha \frac{\partial \phi(x, t)}{\partial x} \Big|_{x=1} = \phi(\ell, t). \quad (4.13d)$$

Here,  $\alpha = \lambda_S / \lambda_D \equiv \mathcal{C}_D / \mathcal{C}_S$  is the inverse of the normalized Stern capacitance, scaled by the Debye capacitance. The Neumann and Dirichlet forms of the Stern boundary condition at the GE, corresponding to Eq. (4.13c), follow directly from the reduced versions of Eq. (4.8) and Eq. (4.9) as:

$$- \varepsilon \frac{\partial \phi(x, t)}{\partial x} \Big|_{x=-1} = \varsigma_g [v_q(t)], \quad (4.14a)$$

$$\phi(-1, t) = \phi(-\ell, t) - \alpha \varsigma_g [v_q(t)]. \quad (4.14b)$$

The parameter  $\alpha$  quantifies the thickness of the Stern layer in comparison to the diffuse layer. It is important to note that the limiting case  $\alpha \rightarrow 0$  corresponds to the Gouy–Chapman model, where the Stern layer is neglected. Conversely, the limit  $\alpha \rightarrow \infty$  recovers the Helmholtz model, in which the diffuse layer is absent. In the present analysis, we focus on scenarios involving finite values of  $\alpha$ , while consistently maintaining the condition  $\varepsilon \ll 1$  [120].

The dimensionless expression for the total current in the system is given by  $j(t) = j_c(x, t) + j_d(x, t)$ , where

$$j_c(x, t) = - \left[ \frac{\partial \rho(x, t)}{\partial x} + c(x, t) \frac{\partial \phi(x, t)}{\partial x} \right], \quad (4.15a)$$

$$j_d(x, t) = -\varepsilon \frac{\partial^2 \phi(x, t)}{\partial x \partial t}, \quad (4.15b)$$

represent the conduction current and the displacement current, respectively, in dimensionless form. Both components are scaled by the limiting diffusion current, defined as  $J_{\text{lim}} = (2eDc_b) / H$ .

The system is considered to be biased with a constant potential  $\bar{v}$ , leading to an equilibrium configuration. This equilibrium is then perturbed by a small time-dependent harmonic voltage, denoted by  $\delta v(t)$ , in which we assume that  $|\delta v(t)| \ll \bar{v}$  to justify a first-order perturbation analysis. This assumption allows for the linearization of the PNP equations and associated boundary conditions, enabling the evaluation of the impedance of the biased system. Accordingly, each relevant variable is expressed as a sum of its equilibrium value—denoted with an overbar—and a small first-order perturbation. For instance, the potential drop within the graphene electrode is approximated by  $v_q(t) \approx \bar{v}_q + \delta v_q(t)$ , leading to the following linearized expression for the surface charge density of the GE

$$\varsigma_g [v_q(t)] \approx \varsigma_g [\bar{v}_q + \delta v_q(t)] \approx \bar{\varsigma}_g + \delta \varsigma_g(t). \quad (4.16)$$

Here,  $\bar{\varsigma}_g = \varsigma_g(\bar{v}_q)$  represents the dimensionless surface charge of graphene in equilibrium, while  $\delta \varsigma_g(t) = -C_q(\bar{v}_q)\delta v_q(t)$  denotes the first-order perturbation in surface charge. The quantity  $C_q(\bar{v}_q)$  is the normalized differential quantum capacitance of graphene,

$$C_q(\bar{v}_q) = -\frac{d\bar{\varsigma}_g}{d\bar{v}_q}. \quad (4.17)$$

Based on Eq. (4.6), the expression for  $C_q(\bar{v}_q)$  is given by  $C_q(\bar{v}_q) = 2\gamma \ln [2 \cosh(\bar{v}_q/2)]$  where  $\gamma = n_g/n_d$  is the ratio that encapsulates the coupling between graphene's electronic structure and the diffuse charge layer of the electrolyte [121]. It is also worth noting that at the neutrality point ( $\bar{v}_q = 0$ ), the quantum capacitance reaches its minimum, given in reduced form as  $C_q^0 \equiv 2\gamma \ln 2$ .

Following the substitution of the linearized variables into the dimensionless PNP system Eq. (4.12), we first solve for the equilibrium state and then analyze the first-order perturbation. This perturbed solution is subsequently used to evaluate the impedance of the system.

## 4.2.2 Equilibrium Solution

In Eq. (4.12), by setting  $\partial/\partial t = 0$ , noting that the expression in the bracket of the first equation represents the sum of the ion fluxes, while the bracketed term in the second equation corresponds to the conduction current (i.e., the difference of the ion fluxes)—both of which vanish in equilibrium—we obtain a system of ordinary differential equations describ-

ing the equilibrium state

$$\frac{d\bar{c}(x)}{dx} + \bar{\rho}(x) \frac{d\bar{\phi}(x)}{dx} = 0, \quad (4.18a)$$

$$\frac{d\bar{\rho}(x)}{dx} + \bar{c}(x) \frac{d\bar{\phi}(x)}{dx} = 0, \quad (4.18b)$$

$$-\varepsilon^2 \frac{d^2\bar{\phi}(x)}{dx^2} = \bar{\rho}(x). \quad (4.18c)$$

where the barred quantities refer to the equilibrium part. By substituting Eq. (4.18c) into Eq. (4.18a) and integrating, we obtain an expression for the equilibrium ion concentration

$$\bar{c}(x) = \bar{c}_0 + \frac{\varepsilon^2}{2} \left[ \frac{d\bar{\phi}(x)}{dx} \right]^2, \quad (4.19)$$

where  $\bar{c}_0$  is an integration constant determined by the integral constraint

$$\int_{-1}^1 \bar{c}(x) dx = 2, \quad (4.20)$$

which results from the normalization of Eq. (4.10). By applying Eq. (4.20) to Eq. (4.19), the integration constant  $\bar{c}_0$  is found to be

$$\bar{c}_0 = 1 - \frac{\varepsilon^2}{4} \int_{-1}^1 \left[ \frac{d\bar{\phi}(x)}{dx} \right]^2 dx. \quad (4.21)$$

Substituting Eq. (4.21) into Eq. (4.19) gives the concentration profile in equilibrium as

$$\bar{c}(x) = 1 + \varepsilon^2 \left[ \frac{1}{2} \left[ \frac{d\bar{\phi}(x)}{dx} \right]^2 - \frac{1}{4} \int_{-1}^1 \left[ \frac{d\bar{\phi}(x)}{dx} \right]^2 dx \right]. \quad (4.22)$$

Substituting both Eq. (4.22) and Eq. (4.18c) into Eq. (4.18b), leads to the following integro-differential equation that governs the equilibrium potential

$$\varepsilon^2 \left[ \frac{d^3\bar{\phi}(x)}{dx^3} - \frac{1}{2} \left[ \frac{d\bar{\phi}(x)}{dx} \right]^3 + \frac{1}{4} \frac{d\bar{\phi}(x)}{dx} \int_{-1}^1 \left[ \frac{d\bar{\phi}(x)}{dx} \right]^2 dx \right] - \frac{d\bar{\phi}(x)}{dx} = 0. \quad (4.23)$$

Due to the presence of singular perturbation terms involving  $\varepsilon$ , both Eq. (4.22) and Eq. (4.23) lack analytical solutions in terms of elementary functions and are also challenging

to solve numerically. To address these difficulties, we apply singular perturbation theory using the method of matched asymptotic expansions. This approach allows us to evaluate the complete PNP model by dividing the domain into two separate regions: an “outer region,” which corresponds to the quasineutral bulk electrolyte, and “inner regions” near each electrode, where diffuse-charge dynamics dominate. By matching the solutions in these two regions appropriately, we obtain a composite solution that is uniformly valid across the entire domain in the asymptotic limit  $\varepsilon \rightarrow 0$ . This leads to a reduced model in which the diffuse layers are treated as *thin double layers* compared to the system size—an assumption that remains accurate well below the limiting current density [122, 123, 124]. For the asymptotic analysis at and above the classical limiting current, the reader is referred to Ref.[125].

## Outer Region

As discussed in Section 2.5, in the outer region, we look for regular asymptotic expansions of the form  $f(x) = f_0(x) + \varepsilon f_1(x) + \varepsilon^2 f_2(x) + \dots$ , which are organized by powers of  $\varepsilon$ , starting with the leading-order approximation at  $\varepsilon = 0$ . By substituting such expansions for  $\bar{\phi}(x)$ ,  $\bar{c}(x)$ , and  $\bar{\rho}(x)$  into Eq. (4.23), Eq. (4.22), and Eq. (4.18c), and collecting terms of like powers of  $\varepsilon$ , we derive a sequence of differential equations governing the behavior of potential, concentration, and charge density. At the leading order (i.e., when  $\varepsilon = 0$ ), we obtain the following system:

$$\frac{d\bar{\phi}_b(x)}{dx} = 0, \tag{4.24a}$$

$$\bar{c}_b = 1, \tag{4.24b}$$

$$\bar{\rho}_b(x) = 0. \tag{4.24c}$$

Here, the subscript “*b*” indicates that the solution pertains to the outer (bulk) region of the electrolyte, distinguishing it from the inner diffuse layers near the electrodes. From Eq. (4.24a), we infer that the electrostatic potential in the bulk remains spatially constant in equilibrium, denoted by  $\bar{\phi}_b$  and from Eq. (4.24b), we conclude that the total salt concentration is spatially uniform in equilibrium at the leading order. Additionally, Eq. (4.24c) confirms that the outer region is electrically neutral at leading order.

## Inner Region

In the inner regions near the electrodes, as discussed in Section 2.5, we resolve the thin boundary layers by introducing stretched coordinates that magnify their width. Specif-

ically, we define the potential near the GE and the ME as  $\bar{\phi}_g(y) = \bar{\phi}(-1 + \varepsilon y)$  and  $\bar{\phi}_m(z) = \bar{\phi}(1 - \varepsilon z)$  using the coordinate transformations

$$y = \frac{1 + x}{\varepsilon}, \quad (4.25a)$$

$$z = \frac{1 - x}{\varepsilon}, \quad (4.25b)$$

respectively. These stretched coordinates, defined in Eq. (4.25), effectively eliminate the singular perturbation present in the Poisson equation, Eq. (4.18c). This transformation enables us to perform regular asymptotic expansions within the inner layers and derive the leading-order solutions near each electrode independently [126].

The leading-order equations governing the inner layer near the GE are derived by transforming Eq. (4.23), Eq. (4.22), and Eq. (4.18c) using the stretched coordinate from Eq. (4.25a) to give

$$-\frac{d^3 \bar{\psi}_g(y)}{dy^3} + \frac{1}{2} \left( \frac{d\bar{\psi}_g(y)}{dy} \right)^3 + \frac{d\bar{\psi}_g(y)}{dy} = 0, \quad (4.26a)$$

$$\bar{c}_g(y) = 1 + \frac{1}{2} \left( \frac{d\bar{\psi}_g(y)}{dy} \right)^2, \quad (4.26b)$$

$$\bar{\rho}_g(y) = -\frac{d^2 \bar{\psi}_g(y)}{dy^2}. \quad (4.26c)$$

Here,  $\bar{\psi}_g(y) = \bar{\phi}_g(y) - \bar{\phi}_b$  denotes the excess potential in the inner region with respect to the outer region. The corresponding leading-order equations for the ME follow the same form as those in Eq. (4.26), but are expressed in terms of the stretched coordinate  $z \geq 0$  and excess inner potential  $\bar{\psi}_m(z) = \bar{\phi}_m(z) - \bar{\phi}_b$ , with subscripts  $g$  replaced by  $m$ , and functions  $\bar{c}_m(z)$  and  $\bar{\rho}_m(z)$  defined analogously.

By transforming Eq. (4.13c) and Eq. (4.13d) into the stretched inner coordinates using Eq. (4.25), the governing equations for the inner regions, Eq. (4.26), are subject to the following leading-order Stern boundary conditions

$$\bar{\psi}_g(0) - \alpha \frac{d\bar{\psi}_g(y)}{dy} \Big|_{y=0} = -\bar{v}_g, \quad (4.27a)$$

$$\bar{\psi}_m(0) - \alpha \frac{d\bar{\psi}_m(z)}{dz} \Big|_{z=0} = \bar{v}_m. \quad (4.27b)$$

Here,  $\bar{v}_g = \bar{\phi}_b - \bar{\phi}(-\ell)$  and  $\bar{v}_m = \bar{\phi}(\ell) - \bar{\phi}_b$  represent the equilibrium potential drops across the EDLs adjacent to the graphene and metal electrodes, respectively. Each EDL comprises both a Stern layer and a diffuse layer. Since the bulk potential  $\bar{\phi}_b$  remains constant (Eq. (4.24a)), the total applied equilibrium voltage can be decomposed into contributions from the internal potential drop across graphene and the two adjacent EDLs, i.e.,  $\bar{v} = \bar{v}_q + \bar{v}_g + \bar{v}_m$  (see Fig. 4.1).

By integrating Eq. (4.26a) from 0 to  $\infty$  and applying the leading-order matching condition,

$$\lim_{y \rightarrow \infty} \left( \frac{d\bar{\phi}_g(y)}{dy} \right) \sim \varepsilon \lim_{x \rightarrow -1} \left( \frac{d\bar{\phi}_b(x)}{dx} \right) = 0, \quad (4.28)$$

and subsequently taking the second derivative  $d^2\bar{\phi}_g(y)/dy^2 \rightarrow 0$  as  $y \rightarrow \infty$ , one can derive—after some algebraic manipulation—the leading-order electric field within the diffuse layer near the GE

$$-\frac{d\bar{\psi}_g(y)}{dy} = 2 \operatorname{csch}(y + K_g), \quad (4.29)$$

where  $K_g$  is an integration constant determined through the boundary condition at  $y = 0$ , using Eq. (4.27a). The corresponding leading-order solution to Eq. (4.29) is

$$\bar{\psi}_g(y) = 4 \tanh^{-1} [e^{-(y+K_g)}] \operatorname{sign} [\bar{\psi}_g(0)]. \quad (4.30)$$

From the result in Eq. (4.30), we can deduce the identity [120]

$$\operatorname{csch}(y + K_g) = \sinh \left( \frac{\bar{\psi}_g(y)}{2} \right), \quad (4.31)$$

which, when substituted into Eq. (4.29), leads to the following expression for the electric field

$$-\frac{d\bar{\psi}_g(y)}{dy} = 2 \sinh \left( \frac{\bar{\psi}_g(y)}{2} \right). \quad (4.32)$$

Since the governing equations for the ME side are structurally identical to those in Eq. (4.26), the same leading-order form of the electric field applies in the inner region near the ME

$$-\frac{d\bar{\psi}_m(z)}{dz} = 2 \sinh \left( \frac{\bar{\psi}_m(z)}{2} \right). \quad (4.33)$$

Furthermore, by integrating the Poisson equation, Eq. (4.26c), over the interval  $0 < y < \infty$ , and applying the matching condition given in Eq. (4.28) along with the expression from Eq. (4.32), we obtain the surface charge density within the diffuse layer near the GE as

$$\bar{\zeta}_d^g = \left. \frac{d\bar{\psi}_g(y)}{dy} \right|_{y=0} = -2 \sinh \left( \frac{\bar{\psi}_g(0)}{2} \right). \quad (4.34)$$

Applying the same methodology and using Eq. (4.33), the surface charge density within the diffuse layer on the ME side is given by

$$\bar{\zeta}_d^m = \left. \frac{d\bar{\psi}_m(z)}{dz} \right|_{z=0} = -2 \sinh \left( \frac{\bar{\psi}_m(0)}{2} \right). \quad (4.35)$$

Now, transforming the coupling condition in Eq. (4.11) into the inner coordinate system, we get

$$\left. \frac{d\bar{\psi}_g(y)}{dy} \right|_{y=0} = - \left. \frac{d\bar{\psi}_m(z)}{dz} \right|_{z=0}, \quad (4.36)$$

which leads us to the relation

$$\bar{\psi}_g(0) = -\bar{\psi}_m(0), \quad (4.37)$$

and also implies that  $\bar{\zeta}_d^g + \bar{\zeta}_d^m = 0$ , confirming the leading-order charge neutrality of the electrolyte in equilibrium. By comparing the Stern boundary conditions Eq. (4.27a) and Eq. (4.27b) and using the identities in Eq. (4.37) and Eq. (4.36), we conclude

$$\bar{v}_g = \bar{v}_m, \quad (4.38)$$

indicating that the total leading-order voltage drops across the electric double layers near both the GE and ME are equal at equilibrium. Thus, the potential drop inside the graphene can be written as

$$\bar{v}_q = \bar{v} - 2\bar{v}_g, \quad (4.39)$$

which reveals how the internal potential drop across graphene is related to both the total applied voltage and the combined potential drops across the diffuse layers on either side of the cell (see Fig. 4.1).

By transforming the normalized Neumann form of the Stern boundary condition from Eq. (4.14a) into the inner coordinate  $y$  in Eq. (4.25a) and using Eq. (4.34) together with

Eq. (4.39), we recover the expression for charge neutrality near the GE in equilibrium  $\bar{\varsigma}_g(\bar{v}_g) + \bar{\varsigma}_d^g = 0$  which can be written explicitly as

$$\gamma \left[ \operatorname{dilog} \left( 1 + e^{\bar{v}-2\bar{v}_g} \right) - \operatorname{dilog} \left( 1 + e^{-(\bar{v}-2\bar{v}_g)} \right) \right] = 2 \sinh \left( \frac{\bar{\psi}_g(0)}{2} \right), \quad (4.40)$$

where the left-hand side represents the equilibrium surface charge on graphene, and the right-hand side corresponds to the diffuse-layer charge near the GE. In addition, substituting Eq. (4.34) into the Stern boundary condition Eq. (4.27a) yields a direct relation between the equilibrium potential drop across the diffuse layer near the GE,  $\bar{\psi}_g(0)$ , and the voltage drop across the adjacent EDL,  $\bar{v}_g$ :

$$\bar{\psi}_g(0) + 2\alpha \sinh \left( \frac{\bar{\psi}_g(0)}{2} \right) = -\bar{v}_g. \quad (4.41)$$

The coupled system of equations given by Eq. (4.40) and Eq. (4.41) can be solved numerically for the unknowns  $\bar{\psi}_g(0)$  and  $\bar{v}_g$ , thereby fully characterizing the equilibrium response of the system for any specified values of  $\bar{v}$  and  $\alpha$ .

### 4.2.3 Linear dynamics

Recalling that the barred quantities denote the equilibrium state, the linearized PNP equations, Eq. (4.12), governing the perturbations in salt concentration,  $\delta c(x, t)$ , charge density,  $\delta \rho(x, t)$ , and potential,  $\delta \phi(x, t)$ , take the following form

$$\frac{\partial \delta c(x, t)}{\partial t} = \varepsilon \frac{\partial}{\partial x} \left[ \frac{\partial \delta c(x, t)}{\partial x} + \bar{\rho}(x) \frac{\partial \delta \phi(x, t)}{\partial x} + \delta \rho(x, t) \frac{d\bar{\phi}(x)}{dx} \right], \quad (4.42a)$$

$$\frac{\partial \delta \rho(x, t)}{\partial t} = \varepsilon \frac{\partial}{\partial x} \left[ \frac{\partial \delta \rho(x, t)}{\partial x} + \bar{c}(x) \frac{\partial \delta \phi(x, t)}{\partial x} + \delta c(x, t) \frac{d\bar{\phi}(x)}{dx} \right], \quad (4.42b)$$

$$-\varepsilon^2 \frac{\partial^2 \delta \phi(x, t)}{\partial x^2} = \delta \rho(x, t). \quad (4.42c)$$

The boundary conditions, Eq. (4.13), are linearized as

$$\left[ \frac{\partial \delta c(x, t)}{\partial x} + \bar{\rho}(x) \frac{\partial \delta \phi(x, t)}{\partial x} + \delta \rho(x, t) \frac{d\bar{\phi}(x)}{dx} \right] \Big|_{x=\pm 1} = 0, \quad (4.43a)$$

$$\left[ \frac{\partial \delta \rho(x, t)}{\partial x} + \bar{c}(x) \frac{\partial \delta \phi(x, t)}{\partial x} + \delta c(x, t) \frac{d\bar{\phi}(x)}{dx} \right] \Big|_{x=\pm 1} = 0, \quad (4.43b)$$

$$\delta \phi(-1, t) - \varepsilon \alpha \frac{\partial \delta \phi(x, t)}{\partial x} \Big|_{x=-1} = \delta \phi(-\ell, t), \quad (4.43c)$$

$$\delta \phi(1, t) + \varepsilon \alpha \frac{\partial \delta \phi(x, t)}{\partial x} \Big|_{x=1} = \delta \phi(\ell, t), \quad (4.43d)$$

with the currents, Eq. (4.15), being linearized as

$$\delta j_c(x, t) = - \left[ \frac{\partial \delta \rho(x, t)}{\partial x} + \bar{c}(x) \frac{\partial \delta \phi(x, t)}{\partial x} + \delta c(x, t) \frac{d\bar{\phi}(x)}{dx} \right], \quad (4.44a)$$

$$\delta j_d(x, t) = -\varepsilon \frac{\partial^2 \delta \phi(x, t)}{\partial x \partial t}. \quad (4.44b)$$

Transforming into the frequency domain using Laplace transform which is denoted by a tilde, the system of Eq. (4.42) becomes

$$s \delta \tilde{c}(x, s) = \varepsilon \frac{\partial}{\partial x} \left[ \frac{\partial \delta \tilde{c}(x, s)}{\partial x} + \bar{\rho}(x) \frac{\partial \delta \tilde{\phi}(x, s)}{\partial x} + \delta \tilde{\rho}(x, s) \frac{d\bar{\phi}(x)}{dx} \right], \quad (4.45a)$$

$$s \delta \tilde{\rho}(x, s) = \varepsilon \frac{\partial}{\partial x} \left[ \frac{\partial \delta \tilde{\rho}(x, s)}{\partial x} + \bar{c}(x) \frac{\partial \delta \tilde{\phi}(x, s)}{\partial x} + \delta \tilde{c}(x, s) \frac{d\bar{\phi}(x)}{dx} \right], \quad (4.45b)$$

$$-\varepsilon^2 \frac{\partial^2 \delta \tilde{\phi}(x, s)}{\partial x^2} = \delta \tilde{\rho}(x, s), \quad (4.45c)$$

where  $s = i\omega\tau_c$  is the Laplace variable. The boundary conditions, (4.43), are also transformed into the frequency domain as

$$\left[ \frac{\partial \delta \tilde{c}(x, s)}{\partial x} + \bar{\rho}(x) \frac{\partial \delta \tilde{\phi}(x, s)}{\partial x} + \delta \tilde{\rho}(x, s) \frac{d\bar{\phi}(x)}{dx} \right] \Big|_{x=\pm 1} = 0, \quad (4.46a)$$

$$\left[ \frac{\partial \delta \tilde{\rho}(x, s)}{\partial x} + \bar{c}(x) \frac{\partial \delta \tilde{\phi}(x, s)}{\partial x} + \delta \tilde{c}(x, s) \frac{d\bar{\phi}(x)}{dx} \right] \Big|_{x=\pm 1} = 0, \quad (4.46b)$$

$$\delta \tilde{\phi}(-1, s) - \varepsilon \alpha \frac{\partial \delta \tilde{\phi}(x, s)}{\partial x} \Big|_{x=-1} = \delta \tilde{\phi}(-\ell, s), \quad (4.46c)$$

$$\delta \tilde{\phi}(1, s) + \varepsilon \alpha \frac{\partial \delta \tilde{\phi}(x, s)}{\partial x} \Big|_{x=1} = \delta \tilde{\phi}(\ell, s), \quad (4.46d)$$

with the currents, Eq. (4.44), being transformed into the frequency domain according to

$$\delta \tilde{j}_c(x, s) = - \left[ \frac{\partial \delta \tilde{\rho}(x, s)}{\partial x} + \bar{c}(x) \frac{\partial \delta \tilde{\phi}(x, s)}{\partial x} + \delta \tilde{c}(x, s) \frac{d\bar{\phi}(x)}{dx} \right], \quad (4.47a)$$

$$\delta \tilde{j}_d(x, s) = -\varepsilon s \frac{\partial \delta \tilde{\phi}(x, s)}{\partial x}. \quad (4.47b)$$

By substituting the Poisson equation, Eq. (4.45c), into Eq. (4.45a) and Eq. (4.45b), we obtain the following system

$$s \delta \tilde{c}(x, s) = \varepsilon \frac{\partial^2 \delta \tilde{c}(x, s)}{\partial x^2} - \varepsilon^3 \frac{\partial^2}{\partial x^2} \left[ \frac{d\bar{\phi}(x)}{dx} \frac{\partial \delta \tilde{\phi}(x, s)}{\partial x} \right], \quad (4.48a)$$

$$-s\varepsilon \frac{\partial^2 \delta \tilde{\phi}(x, s)}{\partial x^2} = -\varepsilon^2 \frac{\partial^4 \delta \tilde{\phi}(x, s)}{\partial x^4} + \frac{\partial}{\partial x} \left[ \bar{c}(x) \frac{\partial \delta \tilde{\phi}(x, s)}{\partial x} + \delta \tilde{c}(x, s) \frac{d\bar{\phi}(x)}{dx} \right]. \quad (4.48b)$$

## Outer Region

Expanding Eq. (4.48a) asymptotically in powers of  $\varepsilon$ , we find that the leading-order perturbation in concentration is identically zero

$$\delta \tilde{c}_b(x, s) = 0. \quad (4.49)$$

Given that  $\bar{c}_b(x) = 1$  in the bulk according to Eq. (4.22) and that  $\delta \tilde{c}(x, s) = 0$  from Eq. (4.45a) and  $\delta \tilde{\rho}(x, s) = 0$  from Eq. (4.45c), Eq. (4.48b) simplifies at leading order to

$\partial^2 \delta \tilde{\phi}(x, s) / \partial x^2 = 0$ . Thus, the perturbation of the potential in the bulk (outer region) is

$$\delta \tilde{\phi}_b(x, s) = A(s)x + B(s), \quad (4.50)$$

valid for  $-1 < x < 1$ , where  $A(s)$  and  $B(s)$  are constants to be determined. From Eq. (4.47a), the leading-order conductive current density in the bulk is constant and given by

$$\delta \tilde{j}_{c,b}(x, s) = -\frac{\partial \delta \tilde{\phi}_b(x, s)}{\partial x} = -A(s), \quad (4.51)$$

while the leading-order displacement current density vanishes, as inferred from Eq. (4.47b)

$$\delta \tilde{j}_{d,b}(x, s) = 0. \quad (4.52)$$

Together, Eq. (4.51) and Eq. (4.52) demonstrate that, at leading order in the linear regime, the total current density within the bulk region is purely conductive. The constant  $A(s)$  characterizes the frequency-dependent response and will be determined through the appropriate matching conditions explained in the following.

## Conservation of Current

Transforming the linearized current densities in Eq. (4.47) to the inner region near the GE via the transformation in Eq. (4.25a), we obtain

$$\delta \tilde{j}_c^g(y, s) = \frac{-1}{\varepsilon} \left[ \frac{\partial \delta \tilde{\rho}_g(y, s)}{\partial y} + \bar{c}_g(y) \frac{\partial \delta \tilde{\phi}_g(y, s)}{\partial y} + \delta \tilde{c}_g(y, s) \frac{d\bar{\phi}_g(y)}{dy} \right], \quad (4.53a)$$

$$\delta \tilde{j}_d^g(y, s) = -s \frac{\partial \delta \tilde{\phi}_g(y, s)}{\partial y}, \quad (4.53b)$$

where we define  $\delta \tilde{\phi}_g(y, s) = \delta \tilde{\phi}(-1 + \varepsilon y, s)$ , and similarly for other variables. It is known that the total linearized current density remains independent of position [79] in the inner region, and is fully specified by its value at the boundary  $\delta \tilde{j}_g(0, s) = \delta \tilde{j}_c^g(0, s) + \delta \tilde{j}_d^g(0, s)$ . From the zero-flux boundary condition at  $x = -1$  in Eq. (4.46b) and using the coordinate mapping in Eq. (4.25a), it follows from Eq. (4.53a) that  $\delta \tilde{j}_c^g(0, s) = 0$ . Consequently, the total linearized current density at the GE is solely due to the displacement current at the Stern plane  $\delta \tilde{j}_g(0, s) = \delta \tilde{j}_d^g(0, s)$ , which is obtained by evaluating Eq. (4.53b) at  $y = 0$ .

We also note that Eq. (4.15a) and Eq. (4.12b) combine into a continuity equation

$$\frac{\partial \rho(x, t)}{\partial t} + \varepsilon \frac{\partial j_c(x, t)}{\partial x} = 0, \quad (4.54)$$

which, when linearized, Laplace transformed, and expressed in the inner coordinates using Eq. (4.25a), becomes—with Poisson's equation (Eq. (4.42c)) substituted— as

$$\frac{\partial \delta \tilde{j}_c^g(y, s)}{\partial y} = s \frac{\partial^2 \delta \tilde{\phi}_g(y, s)}{\partial y^2}. \quad (4.55)$$

This equation is subject to the boundary condition  $\delta \tilde{j}_c^g(0, s) = 0$  and the matching condition for the currents,  $\delta \tilde{j}_c^g(\infty, s) = \delta \tilde{j}_{c,b}(-1, s) = -A(s)$ , as given by Eq. (4.51). Integrating Eq. (4.55) over  $y$  from 0 to  $\infty$  and using the matching condition

$$\lim_{y \rightarrow \infty} \left( \frac{\partial \delta \tilde{\phi}_g(y, s)}{\partial y} \right) \sim \varepsilon \lim_{x \rightarrow -1} \left( \frac{\partial \delta \tilde{\phi}_b(x, s)}{\partial x} \right) = 0, \quad (4.56)$$

we arrive at

$$A(s) = s \left. \frac{\partial \delta \tilde{\psi}_g(y, s)}{\partial y} \right|_{y=0}, \quad (4.57)$$

which can be interpreted as  $\delta \tilde{j}_{c,b}(x, s) = \delta \tilde{j}_d^g(0, s)$  considering Eq. (4.51). Equation (4.57) reveals that, at leading order, the boundary layer behaves as a capacitor, with the total current determined by the conduction current in the bulk,  $\delta \tilde{j}_{c,b}(x, s) = -A(s)$ , and equal to the displacement current at the surface of the graphene electrode. It is important to emphasize that employing alternative time scales such as the diffusion time scale  $\tau_H = H^2/D$  or the Debye time scale  $\tau_D = \lambda_D^2/D$  in place of the charging time scale  $\tau_c = \lambda_D H/D$  would not recover Eq. (4.57) at leading order. This is due to a mismatch in the balancing of  $\mathcal{O}(1)$  terms in the asymptotic limit  $\varepsilon \rightarrow 0$ , potentially violating the physical requirement of current continuity across the diffuse layer, which is inherently enforced in the matching condition [122].

## Inner Region

By transforming Eq. (4.48) into the inner coordinate system near the GE using the substitution from Eq. (4.25a), the resulting linearized governing equations in this inner region

take the following form

$$s\varepsilon \delta\tilde{c}_g(y, s) = \frac{\partial^2 \delta\tilde{c}_g(y, s)}{\partial y^2} - \frac{\partial^2}{\partial y^2} \left[ \frac{d\bar{\psi}_g(y)}{dy} \frac{\partial \delta\tilde{\psi}_g(y, s)}{\partial y} \right], \quad (4.58a)$$

$$-s\varepsilon \frac{\partial^2 \delta\tilde{\psi}_g(y, s)}{\partial y^2} = -\frac{\partial^4 \delta\tilde{\psi}_g(y, s)}{\partial y^4} + \frac{\partial}{\partial y} \left[ \bar{c}_g(y) \frac{\partial \delta\tilde{\psi}_g(y, s)}{\partial y} + \delta\tilde{c}_g(y, s) \frac{d\bar{\psi}_g(y)}{dy} \right], \quad (4.58b)$$

$$-\frac{\partial^2 \delta\tilde{\psi}_g(y, s)}{\partial y^2} = \delta\tilde{\rho}_g(y, s). \quad (4.58c)$$

In this formulation,  $\delta\tilde{\psi}_g(y, s) = \delta\tilde{\phi}_g(y, s) - \delta\tilde{\phi}_b(-1, s) = \delta\tilde{\phi}(-1 + \varepsilon y, s) + A(s) - B(s)$  denotes the linear perturbation of the excess potential within the diffuse layer on the GE side of the inner region where we have used the expression for the bulk potential perturbation from Eq. (4.50). At leading order, the linearized governing equations given in Eq. (4.58) reduce to

$$\frac{\partial^2 \delta\tilde{c}_g(y, s)}{\partial y^2} - \frac{\partial^2}{\partial y^2} \left[ \frac{d\bar{\psi}_g(y)}{dy} \frac{\partial \delta\tilde{\psi}_g(y, s)}{\partial y} \right] = 0, \quad (4.59a)$$

$$\frac{\partial^4 \delta\tilde{\psi}_g(y, s)}{\partial y^4} - \frac{\partial}{\partial y} \left[ \bar{c}_g(y) \frac{\partial \delta\tilde{\psi}_g(y, s)}{\partial y} + \delta\tilde{c}_g(y, s) \frac{d\bar{\psi}_g(y)}{dy} \right] = 0, \quad (4.59b)$$

$$-\frac{\partial^2 \delta\tilde{\psi}_g(y, s)}{\partial y^2} = \delta\tilde{\rho}_g(y, s). \quad (4.59c)$$

Integrating Eq. (4.59a) once and using the equilibrium matching condition from Eq. (4.28) along with

$$\lim_{y \rightarrow \infty} \left( \frac{\partial \delta\tilde{c}_g(y, s)}{\partial y} \right) \sim \varepsilon \lim_{x \rightarrow -1} \left( \frac{\partial \delta\tilde{c}_b(x, s)}{\partial x} \right) = 0, \quad (4.60)$$

we obtain the intermediate result

$$\frac{\partial \delta\tilde{c}_g(y, s)}{\partial y} - \frac{\partial}{\partial y} \left( \frac{d\bar{\psi}_g(y)}{dy} \frac{\partial \delta\tilde{\psi}_g(y, s)}{\partial y} \right) = 0. \quad (4.61)$$

Integrating once more, and applying the linearized matching conditions  $\lim_{y \rightarrow \infty} \delta\tilde{c}_g(y, s) \sim \lim_{x \rightarrow -1} \delta\tilde{c}_b(x, s) = 0$  along with Eq. (4.28) again, we find that the concentration perturbation in the diffuse layer near the GE is given by

$$\delta\tilde{c}_g(y, s) = \frac{d\bar{\psi}_g(y)}{dy} \frac{\partial \delta\tilde{\psi}_g(y, s)}{\partial y}. \quad (4.62)$$

Substituting this result into Eq. (4.59b), integrating, and once more using the matching condition for the electric field using Eq. (4.28) yields

$$\frac{\partial^3 \delta \tilde{\psi}_g(y, s)}{\partial y^3} = \left[ \bar{c}_g(y) + \left( \frac{d\bar{\psi}_g(y)}{dy} \right)^2 \right] \frac{\partial \delta \tilde{\psi}_g(y, s)}{\partial y}. \quad (4.63)$$

Rewriting the above in terms of the electric field,  $\delta \tilde{E}_g(y, s) = -\partial \delta \tilde{\psi}_g(y, s) / \partial y$  and using the expressions for  $\bar{c}_g(y)$  from Eq. (4.26b) and  $d\bar{\psi}_g(y)/dy$  from Eq. (4.29), the above equation becomes

$$\frac{\partial^2 \delta \tilde{E}_g(y, s)}{\partial y^2} = [1 + 6 \operatorname{csch}^2(y + K_g)] \delta \tilde{E}_g(y, s), \quad (4.64)$$

which is a second-order linear differential equation with variable coefficients whose linearly independent eigenfunction  $U(y)$ , vanishing as  $y \rightarrow \infty$ , is given by [127]

$$U(y) = 3 \operatorname{csch}(y + K_g) \coth(y + K_g). \quad (4.65)$$

Hence, the general solution for the electric field perturbation, Eq. (4.64), can be written as

$$\delta \tilde{E}_g(y, s) = G(s)U(y), \quad (4.66)$$

where  $G(s)$  is a constant to be determined. It is important to note that Eq. (4.66) satisfies the asymptotic condition  $\delta \tilde{E}_g(\infty, s) = 0$ , which is required by the matching condition for the electric field at leading order, Eq. (4.56).

Utilizing Eq. (4.29) along with Eq. (4.31), we arrive at the following identity (as detailed in [120])

$$2 \operatorname{csch}(y + K_g) \coth(y + K_g) = \frac{d^2 \bar{\psi}_g(y)}{dy^2}. \quad (4.67)$$

This result allows us to express the electric field given in Eq. (4.66) in terms of the equilibrium excess potential  $\bar{\psi}_g(y)$  in the diffuse layer near the GE. By making use of Eq. (4.32), the electric field perturbation becomes

$$\delta \tilde{E}_g(y, s) = \frac{3}{2} G(s) \frac{d^2 \bar{\psi}_g(y)}{dy^2} = \frac{3}{2} G(s) \sinh[\bar{\psi}_g(y)]. \quad (4.68)$$

To determine the perturbed excess potential in the inner region adjacent to the GE using Eq. (4.66), we integrate

$$-\frac{\partial \delta \tilde{\psi}_g(y, s)}{\partial y} = G(s)U(y). \quad (4.69)$$

from 0 to  $\infty$  where  $U(y)$  in Eq. (4.69) is defined in Eq. (4.65). Then, we apply the matching condition  $\delta\tilde{\psi}_g(\infty, s) = 0$ , arising from the requirement

$$\lim_{y \rightarrow \infty} \delta\tilde{\phi}_g(y, s) \sim \lim_{x \rightarrow -1} \delta\tilde{\phi}_b(x, s), \quad (4.70)$$

to give the expression for the excess potential perturbation as

$$\delta\tilde{\psi}_g(y, s) = 3G(s) \operatorname{csch}(y + K_g) = 3G(s) \sinh \left[ \frac{\bar{\psi}_g(y)}{2} \right]. \quad (4.71)$$

We now define the linear perturbation of the excess potential in the diffuse layer of the inner region adjacent to the metal ME as  $\delta\tilde{\psi}_m(z, s) = \delta\tilde{\phi}_m(z, s) - \delta\tilde{\phi}_b(1, s) = \delta\tilde{\phi}(1 - \varepsilon z, s) - A(s) - B(s)$ , and observe that the governing equation for the associated linearized electric field,  $\delta\tilde{E}_m(z, s) = \partial\delta\tilde{\psi}_m(z, s)/\partial z$ , is identical in form to the equation governing the field near the GE. Hence, by analogy with Eq. (4.68), we can express the electric field perturbation in the ME region as

$$\delta\tilde{E}_m(z, s) = \frac{3}{2}M(s) \sinh \left[ \bar{\psi}_m(z) \right], \quad (4.72)$$

where  $M(s)$  is another constant that needs to be determined. By integrating the above expression from  $z$  to  $\infty$  and applying the boundary condition  $\delta\tilde{E}_m(\infty, s) = 0$ , we obtain

$$\delta\tilde{\psi}_m(z, s) = -3M(s) \operatorname{csch}(z + K_m) = -3M(s) \sinh \left[ \frac{\bar{\psi}_m(z)}{2} \right]. \quad (4.73)$$

Evaluating Eq. (4.68) and Eq. (4.72) at  $y = 0$  and  $z = 0$ , respectively, and applying the linearized coupling condition  $\delta\tilde{E}_g(0, s) = \delta\tilde{E}_m(0, s)$  together with Eq. (4.37), we deduce that the integration constant  $M(s)$  appearing in Eq. (4.72) and Eq. (4.73) must satisfy  $M(s) = -G(s)$ . Additionally, applying Gauss's law in the diffuse layers of both inner regions, we obtain the linearized expressions for the perturbed surface charge densities adjacent to the graphene and metal electrodes, respectively, as  $\delta\tilde{\zeta}_d^g(s) = -\delta\tilde{E}_g(0, s) = -\frac{3}{2}G(s) \sinh \left[ \bar{\psi}_g(0) \right]$  and  $\delta\tilde{\zeta}_d^m(s) = \delta\tilde{E}_m(0, s) = -\frac{3}{2}G(s) \sinh \left[ \bar{\psi}_m(0) \right]$ , which confirms that the electrolyte remains charge-neutral to leading order in the linear approximation  $\delta\tilde{\zeta}_d^g(s) + \delta\tilde{\zeta}_d^m(s) = 0$ . Moreover, referring to the linearized Neumann boundary condition near the GE in normalized form (see Eq. (4.8)), given by  $\delta\tilde{E}_g(0, s) = \delta\tilde{\zeta}_g(s)$ , we conclude that the linearized surface charge density on the graphene electrode is balanced by the nearby diffuse layer at leading order  $\delta\tilde{\zeta}_g(s) + \delta\tilde{\zeta}_d^g(s) = 0$ .

Substituting  $y = 0$  and  $z = 0$  into Eq. (4.71) and Eq. (4.73), respectively, and using the relation  $M(s) = -G(s)$  along with Eq. (4.37), gives  $\delta\tilde{\psi}_m(0, s) = -3M(s) \sinh [\bar{\psi}_m(0)/2] = -3G(s) \sinh [\bar{\psi}_g(0)/2] = -\delta\tilde{\psi}_g(0, s)$ . This identity can now be used in the linearized Stern boundary conditions, given in Eq. (4.46c) and Eq. (4.46d), which in the inner coordinates adjacent to the GE and ME become

$$\delta\tilde{\psi}_g(0, s) + \alpha \delta\tilde{E}_g(0, s) = -\delta\tilde{v}_g(s), \quad (4.74a)$$

$$\delta\tilde{\psi}_m(0, s) - \alpha \delta\tilde{E}_m(0, s) = \delta\tilde{v}_m(s). \quad (4.74b)$$

Here,  $\delta\tilde{v}_g(s) = \delta\tilde{\phi}_b(-1, s) - \delta\tilde{\phi}(-\ell, s)$  represents the linearized potential drop across the full EDL (Stern layer + diffuse layer) near the GE, and  $\delta\tilde{v}_m(s) = \delta\tilde{\phi}(\ell, s) - \delta\tilde{\phi}_b(1, s)$  is the corresponding quantity on the ME side. Adding the left-hand sides of Eq. (4.74a) and Eq. (4.74b), and using the condition  $\delta\tilde{E}_g(0, s) = \delta\tilde{E}_m(0, s)$ , we conclude that the linearized potential drops across the two EDLs are equal  $\delta\tilde{v}_m(s) = \delta\tilde{v}_g(s)$ . To find  $G(s)$ , we revisit Eq. (4.74a) and note that  $\delta\tilde{E}_g(0, s) = \frac{3}{2}G(s) \sinh [\bar{\psi}_g(0)] = C_d \delta\tilde{\psi}_g(0, s)$ , where the potential perturbation at the boundary is given by  $\delta\tilde{\psi}_g(0, s) = 3G(s) \sinh [\bar{\psi}_g(0)/2]$  and  $C_d = \cosh [\bar{\psi}_g(0)/2]$  is the normalized diffuse layer capacitance at equilibrium near the GE. Inserting these relations into Eq. (4.74a) leads to  $\delta\tilde{\psi}_g(0, s) = -\delta\tilde{v}_g(s)/(1 + \alpha C_d)$ . Also, since  $\delta\tilde{E}_g(0, s) = -\delta\tilde{\zeta}_d^g(s)$ , it follows from Eq. (4.74a) that the linearized surface charge in the diffuse layer is  $\delta\tilde{\zeta}_d^g(s) = C_{DL} \delta\tilde{v}_g(s)$  where

$$C_{DL} [\bar{\psi}_g(0)] = \left[ \alpha + \operatorname{sech} \left( \frac{\bar{\psi}_g(0)}{2} \right) \right]^{-1} \equiv (C_S^{-1} + C_d^{-1})^{-1}. \quad (4.75)$$

is the total normalized capacitance of the EDL near the GE, combining the Stern layer capacitance  $C_S = 1/\alpha$  and the diffuse layer capacitance  $C_d$  in series.

## 4.2.4 Impedance

To derive the impedance, we first observe that the total linearized potential difference between the ME and the GE can be expressed as  $\delta\tilde{\phi}(\ell, s) - \delta\tilde{\phi}(-\ell, s) = \delta\tilde{v}_m(s) + \delta\tilde{v}_g(s) + \delta\tilde{v}_b(s)$ , where the potential drop across the outer (bulk) region in the linear regime is determined from Eq. (4.50) as  $\delta\tilde{v}_b(s) = \delta\tilde{\phi}_b(1, s) - \delta\tilde{\phi}_b(-1, s) = 2A(s)$ . Therefore, the full linearized potential difference applied across the ME and GE becomes  $\delta\tilde{v}(s) = \delta\tilde{v}_q(s) + 2\delta\tilde{v}_g(s) + \delta\tilde{v}_b(s)$ , where we recall that  $\delta\tilde{v}_m(s) = \delta\tilde{v}_g(s) = \delta\tilde{\zeta}_d^g(s)/C_{DL}$ . Using Eq. (4.16), the perturbation of the potential drop across graphene may be expressed in terms of the surface charge variation as  $\delta\tilde{v}_q(s) = -\delta\tilde{\zeta}_g(s)/C_q = \delta\tilde{\zeta}_d^g(s)/C_q$ , where  $C_q$  is the normalized differential quantum capacitance of graphene, defined in Eq. (4.17).

To remain consistent with experimental measurement frameworks, we define the total impedance of the system by noting that the potential is applied to the GE, while the ME is held at ground. The impedance is then given by

$$Z(\omega) = -\frac{\delta\tilde{v}(s)}{\delta\tilde{j}(s)} = -\frac{\delta\tilde{v}_q(s) + 2\delta\tilde{v}_g(s)}{\delta\tilde{j}_d^g(0, s)} - \frac{\delta\tilde{v}_b(s)}{\delta\tilde{j}_{c,b}(-1, s)}, \quad (4.76)$$

where in the first term,  $\delta\tilde{j}(s)$  is expressed as the displacement current at the GE surface, given by Eq. (4.53b) as  $\delta\tilde{j}_d^g(0, s) = s\delta\tilde{E}_g(0, s) = -s\delta\tilde{\zeta}_d^g(s)$ , and in the second term,  $\delta\tilde{j}(s)$  corresponds to the conductive current in the bulk, which from Eq. (4.51) is Eq. (4.51),  $\delta\tilde{j}_{c,b}(-1, s) = -A(s)$ , which directly cancels with  $A(s)$  in the expression for the bulk potential drop,  $\delta\tilde{v}_b(s) = 2A(s)$ . Consequently, the total dimensionless impedance simplifies to

$$Z(\omega) = R_b + \frac{1}{sC(\bar{v})}, \quad (4.77)$$

where  $R_b = 2$  denotes the dimensionless bulk resistance, and

$$C(\bar{v}) = \left[ C_q^{-1}(\bar{v}_q) + 2C_{DL}^{-1}[\bar{\psi}_g(0)] \right]^{-1}, \quad (4.78)$$

represents the dimensionless total capacitance of the system. Here,  $C_{DL}$  is defined in Eq. (4.75) and depends on the equilibrium potential drop across the diffuse layer adjacent to the GE,  $\bar{\psi}_g(0)$ , while  $C_q$  is a function of  $\bar{v}_q = \bar{v} - 2\bar{v}_g$ . The values of  $\bar{\psi}_g(0)$  and  $\bar{v}_g$  are obtained by solving the coupled system described in Eq. (4.40) and Eq. (4.41) for any prescribed equilibrium voltage  $\bar{v}$  and ion concentration  $c_b$ .

## 4.3 Results and Discussion

We analyze the impedance characteristics of the system as influenced by key external parameters, namely ion concentration, the total applied potential, and the capacitance of the Stern layers. Ion concentration  $c_b$  is expressed in units of M (mol/L), representative of an aqueous electrolyte containing monovalent ions at room temperature, with the Bjerrum length given by  $\lambda_B \approx 7.2 \text{ \AA}$ , and the Debye length defined as  $\lambda_D = \lambda_{1M}/\sqrt{c_b}$ , where  $\lambda_{1M} \approx 3.03 \text{ \AA}$  is the Debye length corresponding to  $c_b = 1 \text{ M}$ , introduced for convenience. The corresponding Debye capacitance is numerically approximated as  $\mathcal{C}_D \approx 229\sqrt{c_b} \mu\text{F}/\text{cm}^2$ . To ensure consistency with experimental data, the concentrations employed in this analysis include  $c_b = 10^{-1} \text{ M}$ ,  $10^{-2} \text{ M}$ ,  $10^{-3} \text{ M}$ ,  $10^{-4} \text{ M}$ , and  $10^{-5} \text{ M}$ . The total potential difference applied to the ME relative to the GE is taken as  $V = 0, 0.1 \text{ V}, 0.2 \text{ V}, 0.3 \text{ V}, 0.4 \text{ V}$ , and  $0.5 \text{ V}$ . It is worth noting that while the GE appears nominally uncharged at  $V = 0$ , this condition does not correspond to the actual potential of zero charge (PZC) in the system due to the omission of interfacial potential offsets across different media (e.g., work function mismatches) in our modeling, even though ion adsorption and chemical functionalization are excluded. To incorporate both the influence of the Stern layer and its coupling to ion concentration, we define the scaled Stern layer thickness via the relation  $\alpha = \hat{\alpha}\sqrt{c_b}$ , where  $\hat{\alpha} = (\epsilon_b/\epsilon_S)(h/\lambda_{1M})$ . For numerical computations, we consider two representative values,  $\hat{\alpha} = 10$  and  $\hat{\alpha} = 1$ , which reflect high and low estimates of the Stern layer effect, respectively. Additionally, to represent the limit where the Stern layer is effectively absent, we approximate  $\hat{\alpha} \rightarrow 0$  by assigning  $\hat{\alpha} = 10^{-4}$  in our computations.

### 4.3.1 Equilibrium Analysis

Figure 4.2 illustrates the variation of the system's total equilibrium capacitance as a function of externally applied potential, for various ion concentrations and scaled Stern layer thicknesses  $\hat{\alpha}$ . As recently validated by experiments [3], in electrochemical systems incorporating a GE, the total capacitance is largely governed by the quantum capacitance of graphene when ion concentrations are high. Consequently, the curve corresponding to  $c_b = 0.1 \text{ M}$  and  $\hat{\alpha} = 0$  in Fig. 4.2 closely follows the voltage-dependent quantum capacitance profile, reaching a minimum value of  $0.8 \mu\text{F}/\text{cm}^2$  at  $V = 0$ . From the figure, all the curves exhibit a concave profile at  $V = 0$ , where each displays a minimum that becomes smaller as the ion concentration decreases. It can also be observed that for small applied voltages,  $|V| \lesssim 0.1 \text{ V}$ , the influence of the Stern layer on the overall capacitance is negligible. In contrast, for larger voltage magnitudes,  $|V| \gtrsim 0.1 \text{ V}$ , an increase in Stern thickness up to  $\hat{\alpha} = 10$  leads to a noticeable flattening of the curves, effectively capping the

total capacitance. These observations are in close agreement with previous theoretical and experimental studies, further validating the present model and confirming its consistency with [128].

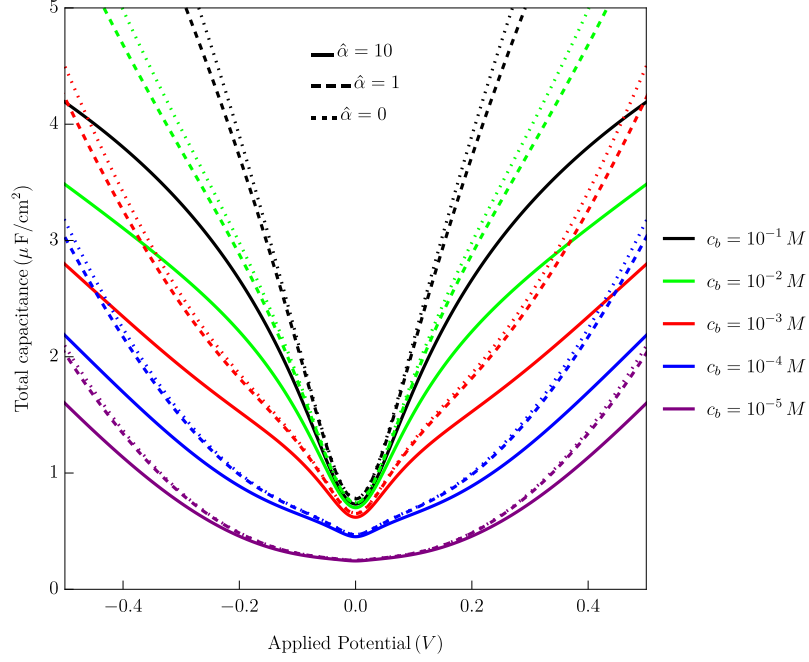


**Figure 4.2:** The equilibrium behavior of the system’s total capacitance as a function of voltage, for varying ion concentrations  $c_b$  and scaled Stern layer thicknesses  $\hat{\alpha}$ .

In the remainder of the analysis, we restrict attention to the cases  $\hat{\alpha} = 10$  and  $\hat{\alpha} = 0$ , since the response for  $\hat{\alpha} = 1$  is nearly identical to  $\hat{\alpha} = 0$ , indicating that the presence of a thin Stern layer has little effect.

### 4.3.2 Frequency Response Analysis

To examine the frequency-dependent response of the system, we rescale the impedance given in equation (4.77) by defining  $Z(\omega) = \mathcal{Z}/\mathcal{R}_0$ , where  $\mathcal{Z}$  denotes the impedance in physical units ( $\Omega$ ), and  $\mathcal{R}_0 = H/(2e\mu A c_b) \equiv \mathcal{R}_{1M}/c_b$  represents the resistance in  $\Omega$  units. Here,  $\mathcal{R}_{1M} = H/(2e\mu A c_{1M})$  is the resistance of an electrolyte with ion concentration  $c_{1M} \approx 0.602 \text{ nm}^{-3}$  and electrode area  $A$ . Based on this, an alternative impedance scaling is introduced as  $\hat{Z} = \mathcal{Z}/\mathcal{R}_{1M}$ , which eliminates the dependence on ion concentration, yielding

$$\hat{Z} = \frac{2}{c_b} + \frac{1}{i\hat{\omega}\sqrt{c_b}C(\bar{v}, c_b)} \equiv \hat{Z}_r + i\hat{Z}_i, \quad (4.79)$$

where  $\hat{\omega} = \omega\lambda_{1M}H/D$  is the normalized frequency variable, and  $\hat{Z}_r$  and  $\hat{Z}_i$  are the real and imaginary components of the scaled impedance  $\hat{Z}$ , respectively. A representative estimate for the scaling factor in  $\hat{\omega}$  can be made by choosing  $H = 1 \text{ }\mu\text{m}$  and  $D = 10^{-6} \text{ cm}^2/\text{sec}$ , leading to  $\lambda_{1M}H/D \approx 3 \text{ }\mu\text{sec}$ . Recalling the cut-off frequency of  $\omega_c/(2\pi) = 1 \text{ MHz}$ , below which EIS is applicable, the scaled cut-off frequency corresponds to  $\hat{\omega}_c \approx 18.85$ . The system's frequency response is then characterized by the impedance magnitude,  $|\hat{Z}| = \sqrt{\hat{Z}_r^2 + \hat{Z}_i^2}$ , and the phase angle,  $\hat{\phi} = \arctan(\hat{Z}_i/\hat{Z}_r)$ . In the subsequent analysis, we explore the impact of two external parameters—the ion concentration and the applied bias voltage—on the frequency response of the system, both with ( $\hat{\alpha} = 10$ ) and without ( $\hat{\alpha} = 0$ ) a Stern layer.

Fig. 4.3 presents the frequency response of the system, with panels (a) and (b) displaying the magnitude and phase, respectively, for various ion concentrations under two conditions: with a Stern layer thickness of  $\hat{\alpha} = 10$  and without a Stern layer ( $\hat{\alpha} = 0$ ). The applied potential is fixed at  $V = 0.2 \text{ V}$ . In Fig. 4.3(b), it is evident that the phase response tends toward  $-90^\circ$  at low frequencies, which corresponds to the slope of  $-1$  in the magnitude plot shown in Fig. 4.3(a), indicating a predominantly capacitive response in this regime. Conversely, at higher frequencies, the phase approaches  $0^\circ$  and the magnitude curves flatten, indicating that the system exhibits resistive behavior. Additionally, both panels reveal that decreasing the ion concentration from  $c_b = 10^{-1} \text{ M}$  to  $c_b = 10^{-5} \text{ M}$  shifts the transition to capacitive behavior toward lower frequencies. This trend highlights the potential of the graphene-based electrochemical cell for (bio)sensing applications, where sensitivity at low frequencies is particularly advantageous [129]. Furthermore, Fig. 4.3(a,b) demonstrates that the inclusion or exclusion of the Stern layer has a negligible effect across the range of concentrations considered.

Ion concentrations in the millimolar (mM) range have been reported to offer an optimal compromise between sensitivity and specificity for the detection of biological analytes and the monitoring of cellular activity using ion-selective electrodes [130, 131, 132]. Motivated by this, panels (c) and (d) of Fig. 4.3 examine the frequency response under varying applied potentials while maintaining a fixed bulk concentration of  $c_b = 10^{-3}$  M, and considering two values of the Stern layer thickness. As shown in Fig. 4.3(c) and Fig. 4.3(d), the system continues to exhibit capacitive behavior at low frequencies and resistive behavior at high frequencies. Across the voltage range from  $V = 0$  to  $V = 0.5$  V, the response curves remain relatively close to one another. Similar to the trends in panels (a) and (b), increasing the bias voltage shifts the impedance features toward lower frequencies, indicating an earlier onset of capacitive behavior, with the phase angle approaching  $\hat{\phi} \rightarrow -90^\circ$ . While the Stern layer has little effect on the impedance response at lower voltages ( $V \lesssim 0.2$  V), its influence becomes more apparent at higher voltages. In these cases, the presence of the Stern layer delays the capacitive transition, shifting the response to lower frequencies.

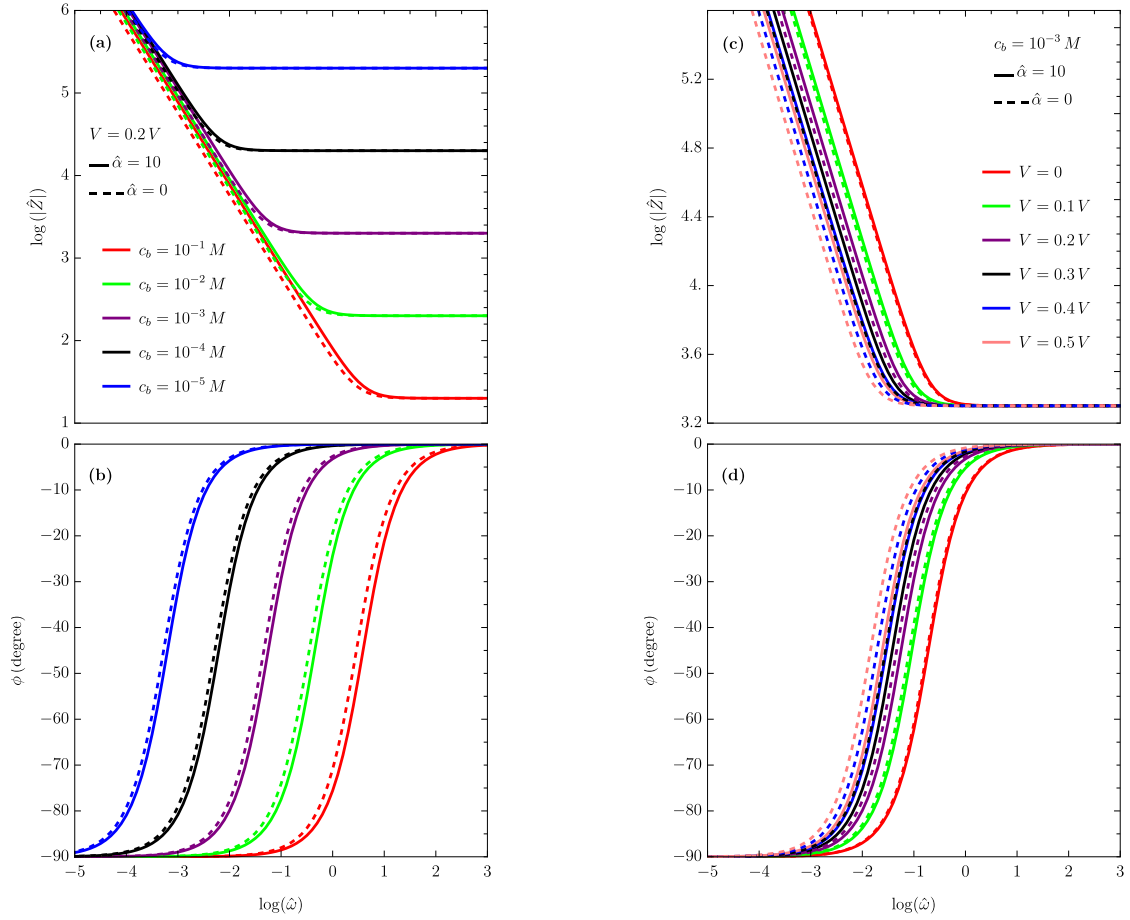


**Figure 4.3:** Frequency response of the graphene-based electrochemical cell. Left panels: (a) magnitude and (b) phase angle as functions of frequency for various ion concentrations  $c_b$  and Stern layer thicknesses  $\hat{a}$ , with the applied voltage fixed at  $V = 0.2$  V. Right panels: (c) magnitude and (d) phase angle plotted against frequency for different applied voltages and Stern layer thicknesses  $\hat{a}$ , with the ion concentration set to  $c_b = 10^{-3}$  M.

## Sensitivity

An important feature of the proposed graphene-based electrochemical system is its sensitivity, which characterizes the electrode's ability to detect small variations in analyte (ion) concentrations through changes in impedance components such as phase and magnitude [133]. In this work, we focus on the Bode phase response,  $\hat{\phi}$ , as a measure of sensitivity, rather than the magnitude response  $|\hat{Z}|$ , due to its superior accuracy and robustness in capturing analyte-induced changes in practical measurements. Phase-based impedance sensing has been widely employed in diverse applications including bioimpedance diagnostics, food quality monitoring, and chemical concentration detection [133, 134].

The angular phase sensitivity, denoted by  $S_{\hat{\phi}}$ , is defined as the relative variation in phase angle with respect to a reference phase value [133], given by

$$S_{\hat{\phi}} = \frac{\hat{\phi} - \hat{\phi}_{\text{ref}}}{\hat{\phi}_{\text{ref}}}, \quad (4.80)$$

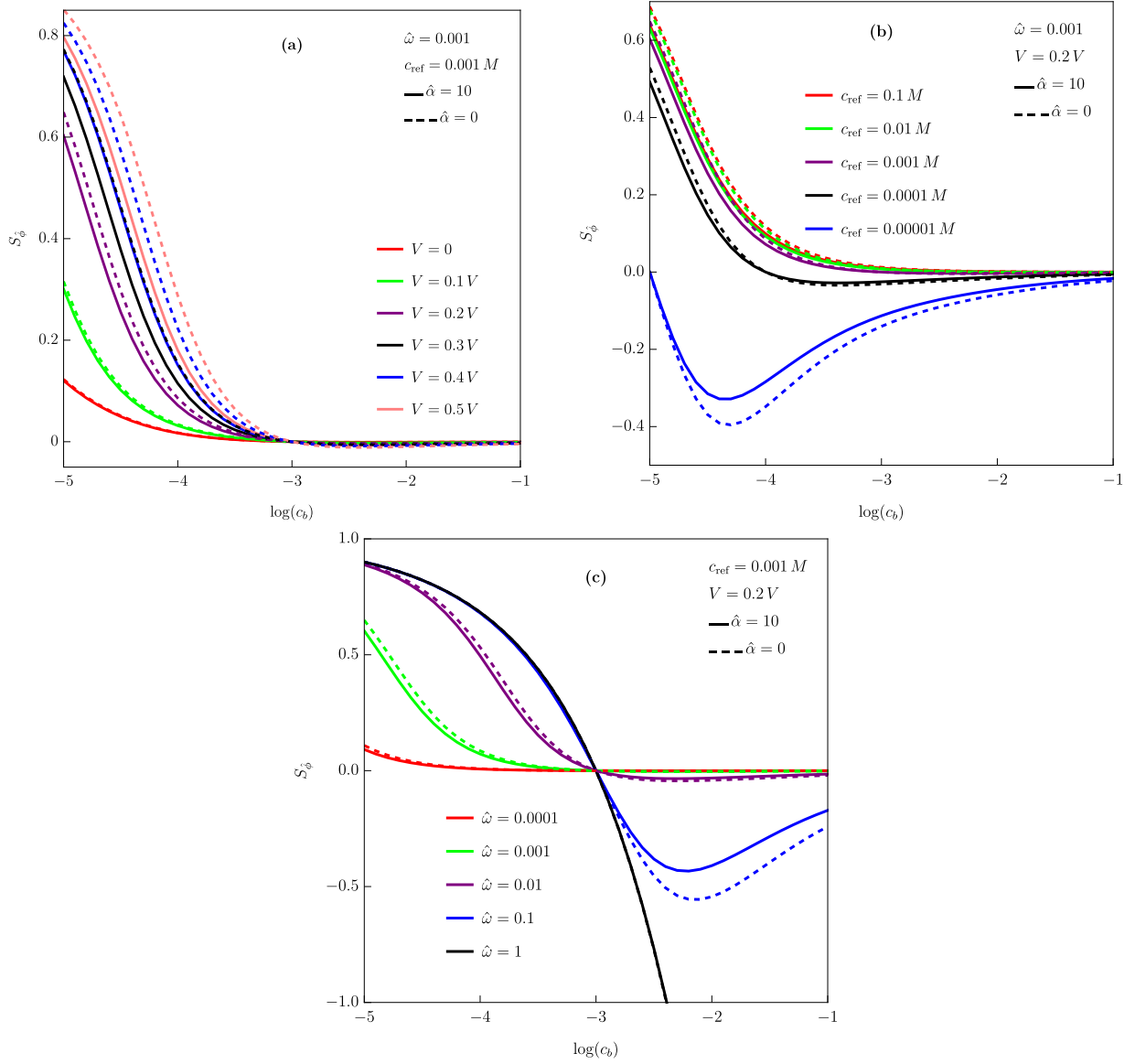
where  $\hat{\phi}_{\text{ref}}$  is the phase response corresponding to a reference ion concentration  $c_{\text{ref}}$ . In what follows, we examine the dependence of  $S_{\hat{\phi}}$  on ion concentration for various values of the applied DC voltage  $V$ , reference concentration  $c_{\text{ref}}$ , and normalized operating frequency  $\hat{\omega}$ , as shown in Fig. 4.4.

Fig. 4.4(a) illustrates the phase sensitivity of the system under varying bias voltages at an operating frequency of  $\hat{\omega} = 10^{-3}$ , with the reference ion concentration set to  $c_{\text{ref}} = 10^{-3}$  M. The results indicate that increasing the bias voltage enhances the sensitivity, although this effect is diminished in the presence of a Stern layer. The influence of the Stern layer becomes appreciable only at higher voltages ( $V = 0.2$  V to  $V = 0.5$  V), while it remains negligible at lower voltages ( $V = 0$  and  $V = 0.1$  V). Additionally, the choice of the reference ion concentration plays a critical role. Specifically, for  $c_b < 10^{-3}$  M, the sensitivity increases with decreasing  $c_b$ , whereas for  $c_b > 10^{-3}$  M, the system exhibits minimal sensitivity to changes in ion concentration.

Fig. 4.4(b) presents the phase sensitivity of the system for various reference ion concentrations, with the applied voltage fixed at  $V = 0.2$  V and the operating frequency set to  $\hat{\omega} = 10^{-3}$ . For reference concentrations ranging from  $c_{\text{ref}} = 10^{-1}$  M to  $c_{\text{ref}} = 10^{-4}$  M, the system exhibits positive sensitivity at low ion concentrations ( $c_b \lesssim 10^{-3}$  M), while remaining largely insensitive for  $c_b > 10^{-3}$  M, consistent with the trends observed in Fig. 4.4(a). Within this range, the magnitude of sensitivity decreases as the reference concentration is lowered, and no significant influence of the Stern layer is observed. However, a distinct behavior emerges at the lowest reference concentration,  $c_{\text{ref}} = 10^{-5}$  M, where the system

exhibits negative sensitivity in the range  $10^{-5} \text{ M} < c_b \lesssim 10^{-2} \text{ M}$ , gradually approaching zero as  $c_b$  increases toward  $10^{-1} \text{ M}$ . In this case, the presence of the Stern layer leads to a notable suppression of sensitivity, particularly for ion concentrations between  $10^{-5} \text{ M}$  and  $10^{-3} \text{ M}$ .

In Fig. 4.4(c), the phase sensitivity is analyzed for a range of operating frequencies, while holding the reference ion concentration and applied voltage fixed at  $c_{\text{ref}} = 10^{-3} \text{ M}$  and  $V = 0.2 \text{ V}$ , respectively, and allowing for variations in the Stern layer thickness. The results reveal two distinct regimes of sensitivity divided by  $c_b = 10^{-3} \text{ M}$ . For  $10^{-5} \text{ M} < c_b < 10^{-3} \text{ M}$ , sensitivity remains positive and increases with frequency from  $\hat{\omega} = 10^{-4}$  to  $\hat{\omega} = 10^{-1}$ , beyond which it saturates, showing no significant change up to  $\hat{\omega} = 1$ . In contrast, for more concentrated electrolytes ( $10^{-3} \text{ M} < c_b < 10^{-1} \text{ M}$ ), sensitivity is negligible at low frequencies ( $\hat{\omega} = 10^{-4}$  to  $\hat{\omega} = 10^{-2}$ ), but becomes increasingly negative as the frequency rises to  $\hat{\omega} = 10^{-1}$ , with a pronounced drop to large negative values at  $\hat{\omega} = 1$ . Further increases in frequency ( $\hat{\omega} = 10, 10^2, 10^3$ ) do not significantly alter the sensitivity, indicating a plateau consistent with the system's transition to resistive behavior in the high-frequency regime. Notably, the influence of the Stern layer is only evident at  $\hat{\omega} = 10^{-1}$ , where it slightly reduces the magnitude of the sensitivity in the concentration range  $10^{-3} \text{ M} < c_b < 10^{-1} \text{ M}$ .



**Figure 4.4:** The phase sensitivity of the proposed graphene-based electrochemical cell *vs* ion concentration. (a) The variations of the phase sensitivity for different values of the bias voltage and the Stern thickness when the reference ion concentration and the operating frequency are set to  $c_{\text{ref}} = 10^{-3} M$  and  $\hat{\omega} = 10^{-3}$ . (b) The variations of the phase sensitivity for different values of the reference ion concentration and the Stern thickness, when  $V = 0.2 V$  and  $\hat{\omega} = 10^{-3}$ . (c) The variations of the phase sensitivity for different values of the operating frequency and the Stern thickness when  $c_{\text{ref}} = 10^{-3} M$  and  $V = 0.2 V$ .

## 4.4 Concluding Remarks

In this chapter, we have investigated the AC response of a charged graphene interfaced with a dilute electrolyte in electrochemical systems under the thin double-layer limit,  $\varepsilon = \lambda_D/H \rightarrow 0$ . This was achieved through the application of the matched asymptotic expansions of the full PNP equations with appropriate boundary conditions for a 1:1 symmetric electrolyte, incorporating both the Stern and diffuse layers in the structure of the electric double layer. The leading-order analysis was carried out in equilibrium conditions under an arbitrary DC applied voltage combined with a small AC perturbations of the quantities. We demonstrated that employing the proper charging time scale,  $\tau_c = \lambda_D H/D$ , produced consistent asymptotic results, leading to a physically meaningful expression for the impedance of the electrochemical cell.

The total capacitance in DC analysis indicate that the Stern layer only significantly affects the system under high bias voltages. Using a normalized frequency,  $\hat{\omega}$ , independent of ion concentration, our frequency-domain analysis showed that lowering ion concentration or increasing the applied voltage enhances the capacitive response in the low-frequency regime—an important feature for (bio)sensing applications. Conversely, increasing concentration or decreasing DC voltages promotes a transition toward resistive behavior at higher frequencies.

Our study of phase sensitivity demonstrated that higher bias voltages enhance sensitivity at low ion concentrations, but the Stern layer tends to suppress this improvement. We also showed that the graphene-based electrode exhibits sensitivity at low operating frequencies ( $\hat{\omega} = 10^{-3}$  to  $10^{-1}$ ) when  $c_b < c_{\text{ref}}$ . Furthermore, at  $\hat{\omega} = 10^{-1}$ , we observed an increase in negative sensitivity for  $c_b > c_{\text{ref}}$ , with notable damping due to the Stern layer. At frequencies beyond  $\hat{\omega} = 1$ , a sudden drop to large negative sensitivity occurs, likely corresponding to the transition to resistive behavior in the system.

# Chapter 5

## Neutral Graphene in Ionic Liquids\*

### 5.1 Introduction

In this chapter, we extend the previous chapters on impedance spectroscopy in simple electrolyte systems interfaced with graphene electrodes [112, 51] to the context of ILs, utilizing mean-field theories originally introduced by Bazant, Storey, and Kornyshev (BSK) [45]. In this framework, we implement the boundary conditions formulated in [63], which account for non-zero electrostatic correlations at the electrode surfaces, together with a modified boundary condition specific to graphene electrodes interfacing ILs [112, 51]. The BSK model has been successfully applied to electrolyte systems, capturing complex ionic correlation effects, including the reversal of electrophoretic mobility in colloids immersed in multivalent electrolytes [136], and the enhanced ion transport in biological ion channels [137, 138, 139, 140]. Unlike our earlier investigations, we do not include DC analysis in this study. Instead, we assume the system resides in a neutral equilibrium configuration, thereby allowing us to concentrate solely on the AC behavior in ILs. Building upon the methodology introduced by Zhao [141], a boundary-layer analysis of the modified Poisson–Nernst–Planck (mPNP) equations is conducted at leading order in the thin EDL limit, utilizing appropriate spatial and temporal scaling to enable asymptotic matching.

In this chapter, we initiate our analysis by linearizing the modified Poisson–Nernst–Planck (mPNP) equations, which incorporate both electrostatic correlation and steric effects, under the assumption that the surface potentials remain small relative

---

<sup>1\*</sup>The material presented in this chapter has been published in *Physical Review E* (M. Yavarian et al., 2025) [135].

to the thermal voltage. This is carried out in conjunction with boundary conditions that account for non-zero correlation effects at the electrode surfaces, the blocking character of the electrodes, and an updated condition tailored to the graphene electrode interfaced with ILs [121]. Upon nondimensionalizing the system, we proceed with a leading-order asymptotic matching in the frequency domain, employing newly defined length scales for the thin electric double layers (EDLs) and a suitable time scale characteristic of the IL response. Utilizing the outer solution and leading-order inner region dynamics, we derive a closed-form expression for the impedance in the low-frequency limit.

## 5.2 Theory

In linear regime, we adopt the system of equations derived in Section 2.4.3 as in Eq. (2.30). By substituting the modified Poisson equation, Eq. (2.23), into the linearized conduction current, Eq. (2.28), we obtain the expression of conduction current in terms of the electrostatic potential  $\Phi(X, \tau)$  as

$$J_c(X, \tau) = \epsilon_b D \left[ \frac{\partial^3 \Phi(X, \tau)}{\partial X^3} - \frac{1}{\lambda_D^2} \frac{\partial \Phi(X, \tau)}{\partial X} - L_c^2 \frac{\partial^5 \Phi(X, \tau)}{\partial X^5} \right], \quad (5.1)$$

where we dropped the  $\delta$  sign for the simplicity of equations. In systems involving ILs, the displacement field is modified and given by  $D(X, \tau) = -\hat{\epsilon} \partial \Phi(X, \tau) / \partial X$ . Consequently, the displacement current, defined as  $J_d(X, \tau) = -\partial D(X, \tau) / \partial \tau$ , incorporates the effects of electrostatic correlations through the operator  $\hat{\epsilon}$ . By applying  $\hat{\epsilon} = \epsilon_b (L_c^2 \nabla^2 - 1)$ , the displacement current takes the form

$$J_d(X, \tau) = -\epsilon_b \frac{\partial}{\partial \tau} \left[ \frac{\partial \Phi(X, \tau)}{\partial X} - L_c^2 \frac{\partial^3 \Phi(X, \tau)}{\partial X^3} \right], \quad (5.2)$$

which separates into two distinct components: the first term corresponds to the classical displacement current, while the second captures the influence of the IL, specifically the electrostatic correlations between ions.

To obtain an explicit solution to the governing equations, it is essential to impose suitable boundary conditions. As shown by de Souza and Bazant [63], the appropriate boundary condition for the higher-order Poisson equation arises from an interfacial stress balance that accounts for both mechanical and electrochemical forces within the structured ionic layers near the charged surface. By enforcing continuity in the normal component of

the total stress tensor—which includes hydrostatic and electrostatic contributions—a natural boundary condition on the electrostatic potential emerges, where  $\partial^3\Phi(X, \tau)/\partial X^3 \neq 0$  at the electrode surfaces. This non-zero third derivative reflects the discontinuity in the normal component of the Maxwell stress tensor across the electrode–electrolyte interface. Physically, it characterizes the electrostatic stress exerted by the correlated ionic environment on the surface and is associated with short-range repulsive forces and overscreening phenomena typical of ILs. Such a comprehensive boundary condition corrects a limitation in the original BSK formulation [45], where interfacial stresses were omitted and the condition  $\partial^3\Phi(X, \tau)/\partial X^3 = 0$  was assumed. To enhance both the mathematical rigor and the physical fidelity of the model—particularly in capturing the layered ionic structure and oscillatory screening evident in experiments and molecular simulations—we impose non-negligible correlation effects at the electrode surfaces [63]

$$L_c \frac{\partial^3\Phi(X, \tau)}{\partial X^3} \Big|_{X=\pm L} = \frac{\partial^2\Phi(X, \tau)}{\partial X^2} \Big|_{X=\pm L}, \quad (5.3)$$

along with the vanishing conduction current condition at the blocking electrodes

$$\left[ \frac{\partial^3\Phi(X, \tau)}{\partial X^3} - \frac{1}{\lambda_D^2} \frac{\partial\Phi(X, \tau)}{\partial X} - L_c^2 \frac{\partial^5\Phi(X, \tau)}{\partial X^5} \right] \Big|_{X=\pm L} = 0. \quad (5.4)$$

We emphasize that the appearance of a non-zero third derivative in the boundary condition Eq. (5.3) is consistent with the linear regime considered in this study, where surface potentials remain small, i.e.,  $|V(\tau)| \ll k_B T/e$  [63]. In contrast, for large surface potentials  $|V(\tau)| \gg k_B T/e$ , where the system is driven out of the equilibrium condition, the boundary condition suggested by Gupta *et al.* [142], namely  $\partial^2\Phi(X, \tau)/\partial X^2 = 0$ , may be more appropriate.

As demonstrated in Eqs. (11) and (12) of our previous work [112], for a system consisting of two distinct electrode materials (graphene and metal), one can apply zero-flux boundary conditions at the electrodes and enforce global charge neutrality through Gauss' law over the entire IL cell. This leads to the conclusion that the system is antisymmetric, satisfying  $\Phi(-X, \tau) = -\Phi(X, \tau)$ ,  $\rho(-X, \tau) = -\rho(X, \tau)$ , and  $C_{\pm}(-X, \tau) = C_{\pm}(X, \tau)$ . This symmetry allows us to restrict our analysis to just one half of the cell.

To incorporate the interfacial characteristics of graphene, we define the total diffuse surface charge density (per unit area) in the vicinity of the graphene electrode (GE) as [122]

$$\varsigma_d(\tau) = \int_{-L}^0 \rho(X, \tau) dX. \quad (5.5)$$

The linearized expression for the surface charge density of graphene, denoted by  $\varsigma_g(\tau)$ , is given by

$$\varsigma_g(\tau) \approx -\mathcal{C}_q V_q(\tau). \quad (5.6)$$

The presence of multiple length scales with distinct orders of magnitude—namely the Debye length ( $\lambda_D$ ), correlation length ( $L_c$ ), and the system size ( $L$ )—makes the dynamics of the system sensitive to their relative magnitudes. This motivates the nondimensionalization of the equations to identify the relevant dimensionless groups. We introduce the dimensionless parameters in accordance with Refs. [112, 141]. We use  $L$  as the characteristic length scale and define the characteristic time scale as  $\tau_c = \lambda_D^{3/2} L / (DL_c^{1/2})$ . Accordingly, time and space are nondimensionalized as  $t = \tau/\tau_c$  and  $x = X/L$ . The governing equations are then reformulated using the following reduced variables: the dimensionless correlation length  $l_c = L_c/L$ , the dimensionless Debye length  $l_D = \lambda_D/L$ , the normalized charge density  $\rho = \varrho/(2ec_b)$ , and the rescaled potentials  $\{\phi, v\} = (e/k_B T)\{\Phi, V\}$ . The current density per unit area is scaled as  $j = J/J_{\text{lim}}$ , where  $J_{\text{lim}} = 2eDc_b/L$  represents the diffusion-limited current density. Similarly, surface charge densities are nondimensionalized via  $\sigma = \varsigma/(2ec_b L)$ , and all capacitances are normalized with respect to the Debye capacitance per unit area,  $\mathcal{C}_D = \epsilon_b/\lambda_D$ . Finally, the equations are transformed into the frequency domain using the Laplace transform by substituting  $\partial/\partial t \equiv s = i\Omega\tau_c$ , where  $\Omega$  (in rad/sec) is the angular frequency of the externally applied AC voltage  $V(\tau)$ .

As a consequence of the above nondimensionalization and transformation to the frequency domain, two additional characteristic length scales naturally emerge in the equations. To illustrate this, consider the normalized and Laplace-transformed form of the continuity equation, Eq. (4.54), which becomes

$$s\rho(x, s) = -\frac{\varepsilon}{\delta_c} \frac{\partial j_c(x, s)}{\partial x}. \quad (5.7)$$

Here, the dimensionless parameter  $\delta_c = l_c/l_D = L_c/\lambda_D$  is interpreted as the correlation length ratio, which governs the degree to which the diffuse layer overcompensates the electrode surface charge. Overcompensation arises, for instance, near a negatively charged electrode when the diffuse layer accumulates an excess of positive ions—more than what is required for local charge neutrality. To restore balance, negatively charged ions that were previously repelled from the interface return from the bulk, giving rise to spatial oscillations in charge density within the EDL. These oscillations, characterized by alternating layers of excess positive and negative ions, are a hallmark of overscreening effects in ILs. The second emerging length scale is  $\varepsilon = \sqrt{\lambda_D L_c}/L$ , which characterizes the spatial extent or thickness of the EDL. Unlike the traditional Debye length  $\lambda_D$  commonly used in dilute

aqueous solutions, this length scale reflects the interplay between screening and correlation effects in ILs. In the following section, we will demonstrate that this parameter plays a central role in the asymptotic matching procedure employed in our analysis.

Continuing with the normalization and transformation process, the conduction current given in Eq. (5.1) becomes

$$j_c(x, s) = \frac{\varepsilon^4}{l_c^2} \frac{\partial^3 \phi(x, s)}{\partial x^3} - \frac{\partial \phi(x, s)}{\partial x} - \varepsilon^4 \frac{\partial^5 \phi(x, s)}{\partial x^5}, \quad (5.8)$$

and the displacement current from Eq. (5.2) is normalized and expressed as

$$j_d(x, s) = -\varepsilon s \left[ \frac{\partial \phi(x, s)}{\partial x} - l_c^2 \frac{\partial^3 \phi(x, s)}{\partial x^3} \right], \quad (5.9)$$

while the Poisson equation, Eq. (2.23), takes the dimensionless form

$$\rho(x, s) = \varepsilon^4 \frac{\partial^4 \phi(x, s)}{\partial x^4} - \frac{\varepsilon^4}{l_c^2} \frac{\partial^2 \phi(x, s)}{\partial x^2}. \quad (5.10)$$

The boundary conditions from Eqs. (5.3) and (5.4) are likewise transformed into their dimensionless forms as follows

$$\delta_c \left. \frac{\partial^3 \phi(x, s)}{\partial x^3} \right|_{x=\pm 1} = \left. \frac{\partial^2 \phi(x, s)}{\partial x^2} \right|_{x=\pm 1}, \quad (5.11)$$

$$\left[ \frac{\varepsilon^4}{l_c^2} \frac{\partial^3 \phi(x, s)}{\partial x^3} - \frac{\partial \phi(x, s)}{\partial x} - \varepsilon^4 \frac{\partial^5 \phi(x, s)}{\partial x^5} \right] \Big|_{x=\pm 1} = 0. \quad (5.12)$$

The total surface charge density of the diffuse layer adjacent to the graphene electrode (GE), originally defined in Eq. (5.5), takes the following normalized form

$$\sigma_d(s) = \int_{-1}^0 \rho(x, s) dx, \quad (5.13)$$

and the normalized expression for the graphene surface charge density, as defined in Eq. (5.6), becomes

$$\sigma_g(s) \approx \frac{-\varepsilon}{\sqrt{\delta_c}} C_q v_q(s), \quad (5.14)$$

where  $C_q = \mathcal{C}_q/\mathcal{C}_D$  denotes the quantum capacitance of neutral graphene normalized by the Debye capacitance per unit area. It is important to emphasize that the presence of the

factor  $\sqrt{\delta_c}$  in Eq. (5.14) is essential for the asymptotic analysis developed in the following section. This factor naturally arises from the choice of the characteristic length scale  $\sqrt{\lambda_D L_c}$ , which is fundamental for describing the structure of the electric double layer in ILs.

### 5.2.1 Asymptotic Matching

In this chapter, we consider typical physical scales for the system: the Debye length is on the order of  $\lambda_D \sim 1 \text{ \AA}$ , and the electrostatic correlation length is approximately  $L_c \sim 1 \text{ nm}$ , while the overall size of the electrochemical cell is  $L \sim 1 \mu\text{m}$ . These values lead to the conclusion that  $\varepsilon = \sqrt{\lambda_D L_c}/L \ll 1$ , indicating that the electric double layer (EDL) is *thin*, justifying the use of asymptotic expansions in powers of  $\varepsilon$  and permitting the application of the method of matched asymptotic expansions in the singular limit  $\varepsilon \ll 1$ . In what follows, we summarize the asymptotic matching procedure developed in [112, 122], focusing on the leading-order behavior of the diffuse layer near the graphene electrode (GE), and ultimately derive an analytic expression for the cell impedance.

#### Outer Region

We begin our analysis by introducing a regular asymptotic expansion—denoted using an overbar—for the potential in the bulk or “*outer*” region as follows

$$\bar{\phi}(x, s) \sim \bar{\phi}_0(x, s) + \varepsilon \bar{\phi}_1(x, s) + \varepsilon^2 \bar{\phi}_2(x, s) + \dots . \quad (5.15)$$

Analogous expansions are used for  $\bar{\rho}(x, s)$ ,  $\bar{j}_c(x, s)$ ,  $\bar{j}_d(x, s)$ , and other relevant quantities. Substituting these expansions into the nondimensionalized equations introduced in the previous subsection, namely Eqs. (5.7)–(5.14), we observe from Eq. (5.10) that  $\bar{\rho}_0(x, s) = 0$ . This confirms that, at leading order in  $\varepsilon$ , the outer region remains electroneutral:  $\bar{\rho}(x, s) \approx \bar{\rho}_0(x, s) = 0$ .

At leading order, the conduction current from Eq. (5.8) reduces to

$$\bar{j}_{c,0}(x, s) = -\frac{\partial \bar{\phi}_0(x, s)}{\partial x}, \quad (5.16)$$

while the displacement current from Eq. (5.9) vanishes at this order, i.e.,  $\bar{j}_{d,0}(x, s) = 0$ . Therefore, the total current at leading order, given by  $\bar{j}_0(s) = \bar{j}_{c,0}(x, s) + \bar{j}_{d,0}(x, s)$ , simplifies to

$$\bar{j}_0(s) = -\frac{\partial \bar{\phi}_0(x, s)}{\partial x}, \quad (5.17)$$

indicating that it is solely governed by the conduction current in the outer region. Integrating Eq. (5.17) yields the antisymmetric leading-order potential profile

$$\bar{\phi}_0(x, s) = -\bar{j}_0(s) x, \quad (5.18)$$

which directly results from the appropriate scaling of the time variable via  $\tau_c = \lambda_D^{3/2} L / (DL_c^{1/2})$ . Consequently, the total potential drop across the outer region at leading order is

$$\bar{v}_{b,0}(s) = \bar{\phi}_0(1, s) - \bar{\phi}_0(-1, s) = -2\bar{j}_0(s). \quad (5.19)$$

### Inner Region

To complete the matched asymptotic expansion, we now consider the “*inner*” region, which captures the singular behavior near the boundary layers adjacent to the electrodes. Due to the antisymmetric nature of the problem, where  $\phi(-x, s) = -\phi(x, s)$ , we limit our analysis to the boundary layer near the graphene electrode (GE) located at  $x = -1$ . For this purpose, we introduce the inner variable  $y = (x + 1)/\varepsilon$  to resolve the fine structure within the boundary layer. This transformation removes singularities in the governing equations, enabling a regular asymptotic expansion in terms of  $\varepsilon$ , represented using tilde notation

$$\tilde{\psi}(y, s) \sim \tilde{\psi}_0(y, s) + \varepsilon \tilde{\psi}_1(y, s) + \varepsilon^2 \tilde{\psi}_2(y, s) + \dots, \quad (5.20)$$

where  $\tilde{\psi}(y, s) = \tilde{\phi}(y, s) - \bar{\phi}(-1, s)$  denotes the excess potential with respect to the outer region. The continuity equation, Eq. (5.7), transforms into the inner region as

$$s\tilde{\rho}(y, s) = -\frac{1}{\delta_c} \frac{\partial \tilde{j}_c(y, s)}{\partial y}. \quad (5.21)$$

The conduction current from Eq. (5.8) becomes

$$\varepsilon \tilde{j}_c(y, s) = \frac{1}{\delta_c} \frac{\partial^3 \tilde{\psi}(y, s)}{\partial y^3} - \frac{\partial \tilde{\psi}(y, s)}{\partial y} - \frac{\partial^5 \tilde{\psi}(y, s)}{\partial y^5}, \quad (5.22)$$

The displacement current, Eq. (5.9), is transformed as

$$\tilde{j}_d(y, s) = -s \left[ \frac{\partial \tilde{\psi}(y, s)}{\partial y} - \delta_c \frac{\partial^3 \tilde{\psi}(y, s)}{\partial y^3} \right]. \quad (5.23)$$

Similarly, the Poisson equation in the inner region becomes

$$\tilde{\rho}(y, s) = \frac{\partial^4 \tilde{\psi}(y, s)}{\partial y^4} - \frac{1}{\delta_c} \frac{\partial^2 \tilde{\psi}(y, s)}{\partial y^2}. \quad (5.24)$$

The boundary conditions, originally given in Eqs. (5.11) and (5.12), take the following forms

$$\left. \frac{\partial^3 \tilde{\psi}(y, s)}{\partial y^3} \right|_{y=0} = \frac{\varepsilon}{\delta_c} \left. \frac{\partial^2 \tilde{\psi}(y, s)}{\partial y^2} \right|_{y=0}, \quad (5.25)$$

$$\left[ \frac{1}{\delta_c} \frac{\partial^3 \tilde{\psi}(y, s)}{\partial y^3} - \frac{\partial \tilde{\psi}(y, s)}{\partial y} - \frac{\partial^5 \tilde{\psi}(y, s)}{\partial y^5} \right] \bigg|_{y=0} = 0, \quad (5.26)$$

and we impose that the excess potential vanishes far into the bulk

$$\tilde{\psi}(\infty, s) = 0. \quad (5.27)$$

The diffuse surface charge density near the GE, as expressed in Eq. (5.13), scales as  $\sigma_d(s) \sim \varepsilon \tilde{\sigma}_d(s)$ , with

$$\tilde{\sigma}_d(s) = \int_0^\infty \tilde{\rho}(y, s) dy \sim \tilde{\sigma}_{d,0}(s) + \varepsilon \tilde{\sigma}_{d,1}(s) + \varepsilon^2 \tilde{\sigma}_{d,2}(s) + \dots, \quad (5.28)$$

Likewise, the graphene surface charge density, from Eq. (5.14), scales as  $\sigma_g(s) = \varepsilon \tilde{\sigma}_g(s)$ , with

$$\tilde{\sigma}_g(s) \approx \frac{-1}{\sqrt{\delta_c}} C_q \tilde{v}_q(s) \sim \tilde{\sigma}_{g,0}(s) + \varepsilon \tilde{\sigma}_{g,1}(s) + \varepsilon^2 \tilde{\sigma}_{g,2}(s) + \dots. \quad (5.29)$$

## Leading Order Dynamics

To study the linear behavior in the inner region, we begin by combining Eq. (5.21), Eq. (5.22), and Eq. (5.24) to derive a single governing equation for the potential  $\tilde{\psi}(y, s)$

$$\frac{1}{\delta_c} \frac{\partial^6 \tilde{\psi}(y, s)}{\partial y^6} - \left( \frac{1}{\delta_c^2} + \varepsilon s \right) \frac{\partial^4 \tilde{\psi}(y, s)}{\partial y^4} + \frac{1}{\delta_c} (1 + \varepsilon s) \frac{\partial^2 \tilde{\psi}(y, s)}{\partial y^2} = 0. \quad (5.30)$$

At leading order (i.e., when  $\varepsilon = 0$ ), the equation simplifies to

$$\frac{\partial^6 \tilde{\psi}_0(y, s)}{\partial y^6} - \frac{1}{\delta_c} \frac{\partial^4 \tilde{\psi}_0(y, s)}{\partial y^4} + \frac{\partial^2 \tilde{\psi}_0(y, s)}{\partial y^2} = 0, \quad (5.31)$$

which governs the leading-order potential in the inner region. The bounded solution satisfying Eq. (5.27) is given by

$$\tilde{\psi}_0(y, s) = A_1(s) \frac{e^{-y\gamma_1}}{\gamma_1^2} + A_2(s) \frac{e^{-y\gamma_2}}{\gamma_2^2}, \quad (5.32)$$

where the parameters  $\gamma_1$  and  $\gamma_2$  are defined as

$$\begin{aligned} \gamma_1 &= \sqrt{\frac{1 + \sqrt{1 - 4\delta_c^2}}{2\delta_c}}, \\ \gamma_2 &= \sqrt{\frac{1 - \sqrt{1 - 4\delta_c^2}}{2\delta_c}}. \end{aligned} \quad (5.33)$$

To determine the integration constants  $A_1(s)$  and  $A_2(s)$ , we impose the leading-order boundary conditions. From Eq. (5.25), we obtain

$$\left. \frac{\partial^3 \tilde{\psi}_0(y, s)}{\partial y^3} \right|_{y=0} = 0, \quad (5.34)$$

and from Eq. (5.26), we have

$$\left[ \frac{1}{\delta_c} \frac{\partial^3 \tilde{\psi}_0(y, s)}{\partial y^3} - \frac{\partial \tilde{\psi}_0(y, s)}{\partial y} - \frac{\partial^5 \tilde{\psi}_0(y, s)}{\partial y^5} \right] \Big|_{y=0} = 0. \quad (5.35)$$

Combining these two conditions, by substituting Eq. (5.34) into Eq. (5.35), we arrive at a simplified boundary condition

$$\left[ \frac{\partial \tilde{\psi}_0(y, s)}{\partial y} + \frac{\partial^5 \tilde{\psi}_0(y, s)}{\partial y^5} \right] \Big|_{y=0} = 0. \quad (5.36)$$

It is worth noting that, at leading order, the correlation-influenced boundary condition from Ref. [63] (Eq. (5.25)) effectively reduces to the condition proposed in the original BSK formulation [45], which neglects such effects. This equivalence reflects the asymptotic consistency of the simplified boundary layer theory at small  $\varepsilon$ .

An additional boundary condition can be derived by integrating the Poisson equation, Eq. (5.24), over the semi-infinite inner region from 0 to  $\infty$ , and applying the standard van

Dyke matching conditions for the electric field and its higher-order derivatives

$$\begin{aligned} \lim_{y \rightarrow \infty} \frac{\partial \tilde{\psi}(y, s)}{\partial y} &\sim \varepsilon \lim_{x \rightarrow -1} \frac{\partial \bar{\phi}(x, s)}{\partial x} \implies \left. \frac{\partial \tilde{\psi}_0(y, s)}{\partial y} \right|_{y \rightarrow \infty} = 0, \\ \lim_{y \rightarrow \infty} \frac{\partial^3 \tilde{\psi}(y, s)}{\partial y^3} &\sim \varepsilon^3 \lim_{x \rightarrow -1} \frac{\partial^3 \bar{\phi}(x, s)}{\partial x^3} \implies \left. \frac{\partial^3 \tilde{\psi}_0(y, s)}{\partial y^3} \right|_{y \rightarrow \infty} = 0, \end{aligned} \quad (5.37)$$

These conditions, together with Eq. (5.34), allow us to obtain the leading-order diffuse layer surface charge density as

$$\tilde{\sigma}_{d,0}(s) = \left. \frac{1}{\delta_c} \frac{\partial \tilde{\psi}_0(y, s)}{\partial y} \right|_{y=0}. \quad (5.38)$$

In parallel, the graphene surface charge density at leading order, from Eq. (5.29), is

$$\tilde{\sigma}_{g,0}(s) \approx \frac{-1}{\sqrt{\delta_c}} C_q \tilde{v}_{q,0}(s), \quad (5.39)$$

where  $\tilde{v}_{q,0}(s)$  is the leading-order voltage drop inside graphene. This can be related to the total voltage drop across the left half-cell,  $\tilde{v}_{g,0}(s) = \tilde{v}_{q,0}(s) + \tilde{v}_{d,0}(s)$ , where  $\tilde{v}_d(s) = \bar{\phi}(-1, s) - \bar{\phi}(0, s) = -\tilde{\psi}(0, s) \sim -\tilde{\psi}_0(0, s) - \varepsilon \tilde{\psi}_1(0, s) - \dots$  is the potential drop across the diffuse layer adjacent to the GE in which when substituted into Eq. (5.39) gives

$$\tilde{\sigma}_{g,0}(s) \approx \frac{-1}{\sqrt{\delta_c}} C_q \left[ \tilde{v}_{g,0}(s) + \tilde{\psi}_0(0, s) \right]. \quad (5.40)$$

Now, applying charge neutrality near the graphene electrode at leading order, i.e.,  $\tilde{\sigma}_{g,0}(s) + \tilde{\sigma}_{d,0}(s) = 0$ , and substituting Eqs. (5.38) and (5.40), we arrive at the following boundary condition for graphene [51], at  $y = 0$

$$\tilde{\psi}_0(0, s) - \frac{1}{\sqrt{\delta_c} C_q} \left. \frac{\partial \tilde{\psi}_0(y, s)}{\partial y} \right|_{y=0} = -\tilde{v}_{g,0}(s). \quad (5.41)$$

We emphasize here that this charge neutrality condition,  $\tilde{\sigma}_{g,0}(s) + \tilde{\sigma}_{d,0}(s) = 0$ , is consistent with the generalized Gauss' law formulated for ILs by Schlumpberger and Bazant (see Eq. (10) in Ref. [143]).

With the pair of boundary conditions derived in Eq. (5.36) and Eq. (5.41), the integration constants  $A_1(s)$  and  $A_2(s)$  can be explicitly determined. Substituting their expressions

into Eq. (5.32) yields the leading-order potential in the inner region near the graphene electrode as

$$\tilde{\psi}_0(y, s) = -\tilde{v}_{g,0}(s) \left[ \frac{e^{-y\gamma_2} \gamma_1 (1 + \gamma_1^4)}{\frac{1}{\sqrt{\delta_c} C_q} (\gamma_1^4 - \gamma_2^4) + \gamma_1 - \gamma_2 + \gamma_1^5 - \gamma_2^5} - \frac{e^{-y\gamma_1} \gamma_2 (1 + \gamma_2^4)}{\frac{1}{\sqrt{\delta_c} C_q} (\gamma_1^4 - \gamma_2^4) + \gamma_1 - \gamma_2 + \gamma_1^5 - \gamma_2^5} \right]. \quad (5.42)$$

We emphasize that, to leading order, the frequency-dependent dynamics are encapsulated solely within the amplitude  $\tilde{v}_{g,0}(s)$ , while the spatial variation is dictated by the square-bracketed prefactor, which is purely a function of the inner coordinate  $y \in [0, \infty)$  and independent of  $s$ .

Using the result in Eq. (5.42), we now construct a uniformly valid composite approximation for the electric potential across the full spatial domain. This is achieved by combining the outer solution, Eq. (5.18), with the inner expansions near each electrode, and subtracting their common asymptotic limit to avoid overlap. Exploiting the antisymmetric nature of the solution, the uniformly valid leading-order electrostatic potential becomes

$$\phi(x, s) \sim \bar{j}_0(s) x + \tilde{\psi}_0\left(\frac{1+x}{\varepsilon}, s\right) - \tilde{\psi}_0\left(\frac{1-x}{\varepsilon}, s\right). \quad (5.43)$$

## Conservation of Current

The appropriateness of the chosen charging time for ILs,  $\tau_c = \lambda_D^{3/2} L / (DL_c^{1/2})$  [141], can be confirmed by analyzing the governing equations. Specifically, by substituting the Poisson equation, Eq. (5.24), into the continuity equation, Eq. (5.21), integrating over the semi-infinite inner domain  $y \in [0, \infty)$ , and applying the matching conditions from Eq. (5.37) together with Eq. (5.34), one obtains the following leading-order relation

$$-s \frac{\partial \tilde{\psi}_0(y, s)}{\partial y} \Big|_{y=0} = \tilde{j}_{c,0}(\infty, s) - \tilde{j}_{c,0}(0, s). \quad (5.44)$$

Using the matching condition for the conduction current at leading order,  $\lim_{y \rightarrow \infty} \tilde{j}_{c,0}(y, s) \sim \lim_{x \rightarrow -1} \bar{j}_{c,0}(x, s)$  and the fact that the conduction current vanishes at the electrode due to

blocking conditions, i.e.,  $\tilde{j}_{c,0}(0, s) = 0$  from Eq. (5.36), the right-hand side of Eq. (5.44) becomes

$$-s \left. \frac{\partial \tilde{\psi}_0(y, s)}{\partial y} \right|_{y=0} = \bar{j}_{c,0}(-1, s). \quad (5.45)$$

Referring to Eq. (5.23) and recalling Eq. (5.34), the left-hand side of Eq. (5.45) can be interpreted as the leading-order displacement current

$$\tilde{j}_{d,0}(0, s) = -s \left. \frac{\partial \tilde{\psi}_0(y, s)}{\partial y} \right|_{y=0}, \quad (5.46)$$

so that substituting into Eq. (5.45) yields the current continuity condition

$$\tilde{j}_{d,0}(0, s) = \bar{j}_{c,0}(-1, s). \quad (5.47)$$

The physical interpretation of Eq. (5.47) affirms that current is conserved to leading order and remains continuous across the diffuse layer. This indicates that the boundary layer behaves like a capacitor, wherein the charging process is governed by the displacement current  $\tilde{j}_{d,0}(0, s)$  at the electrode interface. This displacement current is driven and sustained by the conduction current  $\bar{j}_{c,0}(-1, s)$  flowing in from the bulk, which supplies the required charge to build up the electrode potential.

## 5.2.2 Impedance

The dimensionless impedance of the electrochemical cell, normalized by the DC bulk resistance per unit area  $\mathcal{R}_b = L\lambda_D^2/(\epsilon_b D)$ , can be expressed as the sum of leading-order contributions from the outer and inner regions

$$Z(s) = \frac{-v(s)}{j(s)} = \frac{-\bar{v}_{b,0}(s)}{\bar{j}_{c,0}(-1, s)} - \frac{\tilde{v}_{q,0}(s) + 2\tilde{v}_{d,0}(s)}{\tilde{j}_{d,0}(0, s)}, \quad (5.48)$$

where  $v(s) = \bar{v}_{b,0}(s) + \tilde{v}_{g,0}(s) + \tilde{v}_{d,0}(s)$  is the total applied potential. From the inner region analysis, the leading-order voltage drop across the half-cell near the graphene electrode (GE) is  $\tilde{v}_{g,0}(s) = \tilde{v}_{q,0}(s) + \tilde{v}_{d,0}(s)$ . From the outer region analysis (see Eq. (5.19)), the leading-order bulk voltage drop is  $\bar{v}_{b,0}(s) = \bar{\phi}_0(1, s) - \bar{\phi}_0(-1, s) = -2\bar{j}_0(s)$ . In Eq. (5.48),  $j(s)$  denotes the total current density. In the first term, this is given by  $\bar{j}_{c,0}(-1, s) = \bar{j}_0(s)$ —the leading-order conduction current in the bulk. In the second term, it is  $\tilde{j}_{d,0}(0, s)$ —the leading-order displacement current on the GE surface as obtained in

Eq. (5.46). The structure of the impedance in Eq. (5.48) reveals that the system behaves as a series RC circuit

$$Z(s) = R + \tilde{Z}(s), \quad (5.49)$$

where the resistive term from the bulk (outer) region is

$$R = \frac{-\bar{v}_b(s)}{\bar{j}_{c,0}(-1, s)} = 2, \quad (5.50)$$

and the capacitive contribution from the inner region is

$$\tilde{Z}(s) = -\frac{\tilde{v}_{g,0}(s) + 2\tilde{v}_{d,0}(s)}{\tilde{j}_{d,0}(0, s)} \equiv \frac{1}{s\tilde{C}}, \quad (5.51)$$

with  $\tilde{C}$  denoting the total dimensionless capacitance. Recalling that  $\delta_c = L_c/\lambda_D$ , the characteristic charging time becomes  $\tau_c = \delta_c^{-1/2} L\lambda_D/D$ , so the Laplace variable  $s = i\Omega\tau_c$  scales with correlation length as  $s = i\omega\delta_c^{-1/2}$ , where  $\omega = (L\lambda_D/D)\Omega$  is a dimensionless frequency independent of  $\delta_c$ . Substituting this into Eq. (5.49) gives the frequency-domain form of the impedance

$$Z(\omega, \delta_c) = 2 + \frac{1}{i\omega C(\delta_c)}, \quad (5.52)$$

where

$$C(\delta_c) = \left( C_q^{-1} + 2C_d^{-1}(\delta_c) \right)^{-1} \quad (5.53)$$

is the total dimensionless capacitance. Here,  $C_d = \mathcal{C}_d/\mathcal{C}_D$  is the diffuse layer capacitance normalized by the Debye capacitance, and is given by [144]

$$C_d(\delta_c) = \frac{2\sqrt{2}\chi}{(1+\chi)^{3/2} - (1-\chi)^{3/2}}, \quad (5.54)$$

where  $\chi = \sqrt{1 - 4\delta_c^2}$ .

### 5.3 Results and Discussion

To ensure consistency with available experimental and simulation studies, we adopt the following physical parameters for the ionic liquid under consideration: a temperature of  $T = 300$  K, an ion concentration of  $c_b = 5$  M (where M denotes moles per liter), and a bulk dielectric permittivity of  $\epsilon_b = 10\epsilon_0$ , with  $\epsilon_0 \approx 8.85 \times 10^{-12}$  F/m representing the permittivity of free space. This estimate is in good agreement with the values reported in Ref. [145], validating the physical assumptions and scaling choices employed in this study.

At low voltages within the linear regime, the solutions are characterized by a single free parameter: the normalized correlation length scale  $\delta_c$ . To systematically investigate the influence of ion-ion correlations across different regimes—weak, intermediate, and strong—we consider values of  $\delta_c$  ranging from 0 to 16, in alignment with findings reported in the literature. To examine the structure of the electric double layer (EDL) as influenced by the correlation length, we begin by renormalizing the leading-order potential drop across the diffuse layer, as given in Eq. (5.42), through the transformation  $\tilde{\Psi}_0(y) = -\tilde{\psi}_0(y, s)/\tilde{v}_{g,0}(s)$ . The normalized potential  $\tilde{\Psi}_0(y)$  defined in this manner is independent of the frequency variable  $s$ . To better visualize the impact of  $\delta_c$  on the EDL profile, we recall the expression  $\varepsilon = \sqrt{\lambda_D L_c}/L = \sqrt{\delta_c} l_D$  and reformulate the inner coordinate as  $y = (1+x)/\varepsilon = \zeta/\sqrt{\delta_c}$ . Here,  $\zeta = (1+x)/l_D = (L+X)/\lambda_D \in [0, \infty)$  defines a new inner coordinate scaling that is independent of  $\delta_c$  and aligns with the framework used in Ref. [144]. This reformulation enables a consistent comparison of the potential profile in the diffuse layer across varying values of the correlation length. By substituting  $y = \zeta/\sqrt{\delta_c}$  into  $\tilde{\Psi}_0(y)$ , we obtain a rescaled potential  $\tilde{\Psi}_0(\zeta)$  that reveals the influence of  $\delta_c$  on the EDL structure. This behavior is illustrated for both electrode configurations in Fig. 5.1(a) and Fig. 5.1(b) [146].

Based on the parameters defined in Eq. (5.33), two distinct regimes emerge at the critical value  $\delta_c = 0.5$  for both electrode configurations. In the weak correlation regime, where  $\delta_c < 0.5$ , and particularly in the limiting case  $\delta_c \rightarrow 0$ , the influence of ionic liquid correlations is negligible, and the potential profiles exhibit smooth and monotonic behavior for both electrode systems, as illustrated in Fig. 5.1(a) and Fig. 5.1(b). In this regime, applying Eq. (5.42) and noting that  $C_q = \mathcal{C}_q/\mathcal{C}_D \approx 0.005$ , the normalized potential drop for the GM system tends toward  $\tilde{\Psi}_0(y) \rightarrow C_q/(1+C_q) \approx 0.005$  as  $\delta_c \rightarrow 0$ . This limiting value is visible in Fig. 5.1(a). For the MM system, which corresponds to the limit  $C_q \rightarrow \infty$  [51], the normalized potential drop reaches  $\tilde{\Psi}_0(y) \rightarrow 1$  across all values of  $\delta_c$ , as evident in Fig. 5.1(b). In contrast, for  $\delta_c > 0.5$ , the system enters the strong correlation regime, and the effects of electrostatic correlations become significant for both electrode types. In the asymptotic

limit  $\delta_c \rightarrow \infty$ , the solution to Eq. (5.42) gives  $\tilde{\Psi}_0(y) \rightarrow e^{-y/\sqrt{2}} [\cos(y/\sqrt{2}) - \sin(y/\sqrt{2})]$  which reveals the emergence of charge oscillations within the diffuse layer. Moreover, since the inner variable  $y \propto \delta_c^{-1/2}$ , the spatial extent of the EDL increases proportionally to  $\sqrt{\delta_c}$ , a feature that becomes increasingly prominent in both Fig. 5.1(a) and Fig. 5.1(b) as  $\delta_c$  increases. It is worth noting that the observed behavior in Fig. 5.1(b) for the MM system is in excellent agreement with the numerical simulations reported by Storey and Bazant (see Fig. 1(a) in Ref. [144]), as well as the studies by Gupta *et al.* (see Fig. 12(a) in Ref. [147] and Fig. 3 in Ref. [148]).

For the GM electrode configuration shown in Fig. 5.1(a), the magnitude of the potential drop across the diffuse layer is notably smaller than that observed in the MM configuration depicted in Fig. 5.1(b). This behavior suggests that graphene mitigates the effects of electrostatic correlations, likely due to its distinctive electronic properties—most notably its quantum capacitance. The presence of quantum capacitance in graphene appears to facilitate more uniform charge distribution, improved screening capabilities, and a more efficient ionic response at the electrode interface, thereby diminishing the spatial charge oscillations that are otherwise prominent in conventional metal electrodes.

The dependence of the total capacitance of the GM system on the correlation parameter  $\delta_c$  is presented in Fig. 5.1(c). In general, for highly correlated ionic liquids, the capacitive response becomes negligible, as electrostatic correlations tend to suppress the capacitance [144]. This trend is confirmed analytically via Eqs. (5.53) and (5.54), where the limiting behavior as  $\delta_c \rightarrow \infty$  yields  $C \rightarrow 0$  and  $C_d \rightarrow 0$ . This reduction is evident in the plotted GM data in Fig. 5.1(c), and similarly in the inset for the MM system. In contrast, in the weak correlation limit  $\delta_c \rightarrow 0$ , the total capacitance for the GM system approaches  $C \rightarrow C_q / (1 + C_q) \approx 0.005$  as follows from Eq. (5.53) using  $C_q \approx 0.005$ . For the MM system, taking  $C_q \rightarrow \infty$  leads to  $C_d \rightarrow 1$  via Eq. (5.54), a result that agrees well with numerical predictions by Storey and Bazant (see Fig. 1(b) in Ref. [144]).

Although the total capacitance remains small—on the order of  $C \approx 0.005$ —in the regime of low  $\delta_c$ , this finding underscores the viability of using graphene electrodes in ILs for low-frequency electrochemical impedance measurements. This aligns with similar conclusions drawn in our previous study involving aqueous electrolytes [51].

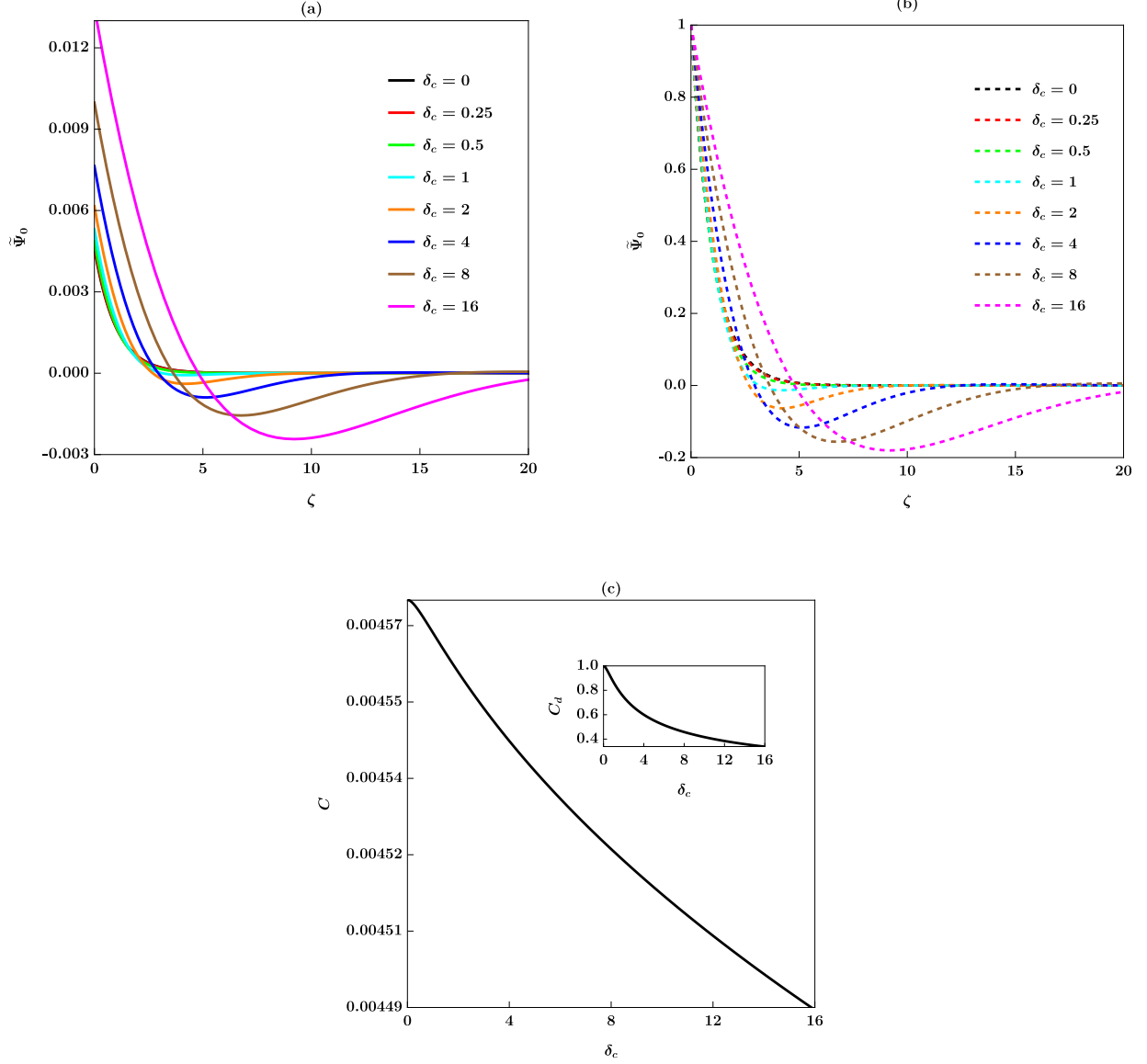


**Figure 5.1:** Impact of the electrostatic correlation length  $\delta_c$  on the structure of the electric double layer (EDL). (a) Variations of the normalized leading-order inner potential drop,  $\tilde{\Psi}_0$ , as a function of the rescaled inner coordinate  $\zeta = (L + X)/\lambda_D$  for the GM electrode pair. (b) Variations of the normalized leading-order inner potential drop,  $\tilde{\Psi}_0$ , as a function of the rescaled inner coordinate  $\zeta = (L + X)/\lambda_D$  for the MM electrode pair. (c) Variations of the total scaled capacitance,  $C(\delta_c)$ , and the scaled EDL capacitance,  $C_d(\delta_c)$  (inset), as functions of  $\delta_c$ .

The frequency response is characterized in terms of the phase angle,  $\phi = \arctan(Z_i/Z_r)$ , shown in Fig. 5.2(a), and the magnitude of the impedance,  $|Z| = \sqrt{Z_r^2 + Z_i^2}$ , shown in Fig. 5.2(b), where  $Z_r$  and  $Z_i$  denote the real and imaginary parts, respectively, of the scaled impedance  $Z$  from Eq. (5.52). Both quantities are plotted as functions of the scaled frequency  $\omega = \Omega L\lambda_D/D$ , displayed on a logarithmic scale. For a representative room-temperature ionic liquid with a diffusion coefficient of  $D = 10^{-7}$  cm<sup>2</sup>/sec and a characteristic cell thickness of  $L = 1$   $\mu$ m, the charging time scale is estimated as  $L\lambda_D/D \approx 11$   $\mu$ sec. This indicates that charging dynamics in IL systems are significantly slower than those in aqueous electrolytes, where we previously reported a characteristic time of approximately 3  $\mu$ s [112]. Also, recalling the cut-off frequency of  $\Omega_c/(2\pi) = 1$  MHz, below which EIS is applicable, the scaled cut-off frequency corresponds to  $\omega_c \approx 70$ .

Based on the phase response shown in Fig. 5.2(a), the MM configuration exhibits phase transitions across a broader frequency range in comparison to the GM configuration for all values of  $\delta_c$ . At high frequencies, as  $\delta_c$  decreases, both systems asymptotically approach purely resistive behavior, with  $\phi \rightarrow 0^\circ$ . In the low-frequency regime, while the MM system displays stronger capacitive behavior as  $\delta_c$  increases, the GM configuration appears to offer greater tunability at low frequencies. Specifically, the GM system reaches the fully capacitive phase response  $\phi = -90^\circ$  at slightly higher frequencies compared to MM, suggesting enhanced responsiveness in the low-frequency domain.

In terms of magnitude, as shown in Fig. 5.2(b), the GM configuration demonstrates a higher impedance magnitude at low frequencies than the MM configuration for the same  $\delta_c$  value. This is accompanied by a slope close to  $-1$  on the log-log plot, indicative of a dominant capacitive response. At high frequencies, both configurations converge to similar  $\log|Z|$  values with a slope approaching zero, signaling a shared resistive character in this regime irrespective of  $\delta_c$ . In the intermediate frequency range, however, the MM configuration consistently

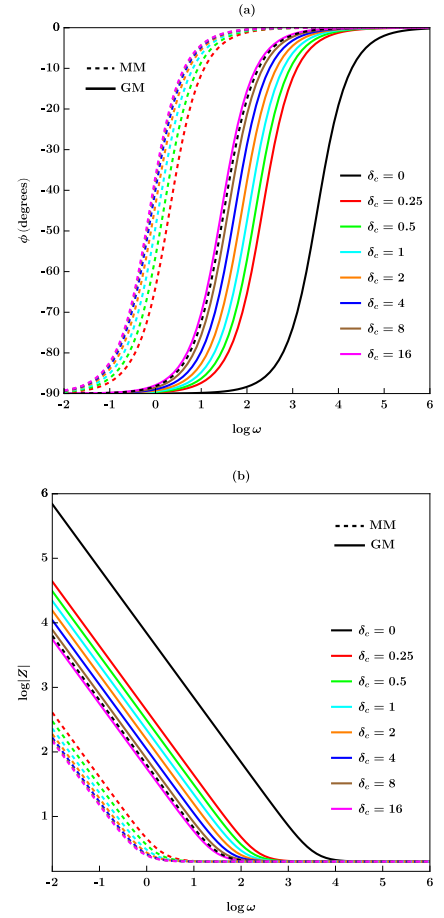


**Figure 5.2:** Impact of the electrostatic correlation length  $\delta_c$  on the frequency response. (a) Variations of the phase response for different values of  $\delta_c$ . (b) Variations of the magnitude response for different values of  $\delta_c$ .

shows a lower  $\log|Z|$  than GM, reflecting its superior conductive performance over that band.

## 5.4 Concluding Remarks

In this work, we have analytically derived the impedance response of an electrochemical cell containing a room-temperature ionic liquid in a neutral equilibrium state, bounded by a graphene-metal (GM) electrode pair and subjected to an externally applied AC voltage. The analysis was performed using the method of matched asymptotic expansions in the limit of thin electric double layers, where the small parameter is defined as  $\varepsilon = \sqrt{\lambda_D L_c}/L \ll 1$ . This allowed us to systematically resolve the leading-order diffuse-charge dynamics across a cell of finite thickness  $2L$ , employing the characteristic charging time scale  $\tau_c = \lambda_D^{3/2} L / (DL_c^{1/2})$  as proposed by Zhao [141].

Within the linear regime, under the influence of the correlation length  $\delta_c = L_c/\lambda_D$ , we investigated the structure of the EDL and the frequency-dependent impedance behavior. Our numerical analysis of the potential drop across the diffuse layer and the total capacitance yields results consistent with prior studies on metal-metal (MM) electrode configurations [141, 144]. For the GM configuration, we observe a reduced potential drop across the diffuse layer relative to MM systems. This behavior may be advantageous for applications where reduced energy storage, minimized ohmic losses, enhanced charge transport rates, and greater electrochemical stability are desired. Furthermore, our analysis indicates that the inclusion of graphene significantly lowers the total capacitance compared to MM systems—an effect that may enhance sensitivity in low-frequency applications such as biosensing, as discussed in our earlier study [51]. Finally, the impedance spectra reveal that MM systems span a broader frequency range and exhibit stronger low-frequency capacitive characteristics. Nonetheless, the GM configuration offers greater tunability in the low-frequency regime, presenting potential advantages for tailored electrochemical response in graphene-based IL systems.

# Chapter 6

## Summary and Future Directions

### 6.1 Summary

In Chapter 3, the frequency response of the graphene/electrolyte interface in dilute electrolytes for neutral graphene with infinite conductivity and neutral graphene with finite conductivity was studied. For the infinite conductivity case, beginning with the PNP equations and appropriate boundary conditions at the graphene interface, we nondimensionalized the system and solved it via the Laplace transform. A comparison between the impedance behavior of graphene–metal (GM) and metal–metal (MM) electrode pairs was conducted across a wide range of frequencies and ion concentrations. The frequency response analysis observation revealed that MM electrodes demonstrated greater sensitivity to ion concentration changes, especially at low frequencies and high ionic strengths. We also confirmed that the quantum capacitance of graphene can be reliably inferred from the zero-frequency intercept in the Nyquist plot of the equivalent cell capacitance, which is typically dominated by the quantum contribution.

For the finite conductivity case, we investigated the frequency-dependent response of a graphene disk electrode (GE) in a three-dimensional cylindrical geometry where we incorporated graphene’s intrinsic quantum-mechanical properties to derive its quantum impedance analytically. Two charge relaxation regimes were identified: the Warburg-type response in the rapid-charging regime (low conductivity or large capacitance) and RC-circuit behavior in the slow-charging regime (high conductivity or small capacitance). The latter is found to be aligned with the concept of quantum-mechanical rate spectroscopy defined by the quantum time scale of the graphene sheet with a finite conductivity. The time-dependent

evolution of the average potential drop inside graphene supported this distinction, capturing early and late time dynamics in high- and low-frequency regimes, respectively. To establish coupling with the electrolyte, we separately analyzed the electrolyte domain in which the quantities were surface averaged, enabling us to reduce the three-dimensional problem into a one-dimensional approximation via the Hankel transform. Coupling the electrolyte region with the GE yielded a boundary condition at the GE/electrolyte interface which finally led us to present a closed-form expression for the electrochemical impedance at the GE/electrolyte interface. The frequency response analysis on the influence of ion concentrations showed that both finite and infinite conductivity cases exhibit capacitive behavior in the low-frequency regime. At high frequencies, however, the finite conductivity case demonstrated Warburg characteristics, evidenced by a  $-45^\circ$  phase angle and  $-1/2$  slope in the Bode plots. We also examined the impact of electrode radius. At low frequencies, both cases retained capacitive behavior. At high frequencies, increasing the radius amplified deviations from ideal capacitive behavior in the finite conductivity case. Similarly, contact resistance reflected a consistent capacitive response across the full frequency spectrum in both models.

In Chapter 4, we explored the AC response of a charged graphene interfaced with a dilute electrolyte using the matched asymptotic expansions of the full PNP equations in the thin-double-layer limit. Using the appropriate charging time scale to ensure consistency in asymptotic analysis, the nonlinear leading-order solutions under the DC voltage plus the linear leading-order solutions under the small AC perturbations were combined to produce the analytic expression for the low-frequency RC impedance. According to the DC analysis, the Stern layer significantly influences capacitance only under high applied DC voltages. Normalized frequency-domain analysis revealed that lower ion concentrations and higher DC voltages enhance capacitive behavior at low frequencies, while the converse conditions induce resistive behavior at high frequencies. A sharp drop in phase sensitivity at intermediate frequencies marked the transition to resistive behavior. The general impedance features—capacitive at low frequencies, resistive at high frequencies, and governed by characteristic frequency—extend to broader systems such as asymmetric cells [149], mixed ionic-electronic conductors [150], and ion-exchange membranes [151].

In Chapter 5, we derived the impedance of a graphene–metal (GM) electrode system containing a room-temperature ionic liquid under a small AC voltage in the linear regime. Matched asymptotic expansions were used in the thin-double-layer limit to resolve the leading-order diffuse-charge dynamics, incorporating a suitable time scale from Zhao [141] to ensure consistent asymptotic results. The observation of the frequency response based on the electrostatic correlation length, revealed structural features of the electric double layer and the corresponding impedance. Compared to metal–metal (MM) systems, GM configurations exhibited smaller diffuse-layer potential drops and lower total capacitance, beneficial for applications requiring reduced energy storage and enhanced sensitivity. Impedance spectra showed broader frequency response and stronger low-frequency capacitive behavior in MM systems. However, GM systems allowed greater tunability in the low-frequency range, making them advantageous for bioelectronic applications with tailored electrochemical response.

## 6.2 Future Directions

- *Graphene with a Finite Conductivity*

In Chapter 4, we extended our analysis to charged graphene with infinite conductivity under the assumption that the system is in a neutral state at equilibrium, aligning with experimental findings reported in [93, 75, 74]. Building on this methodology, future work could further extend the study in Chapter 3 by considering graphene with finite conductivity when charged. In this scenario, the conductivity of graphene is no longer constant but varies with the doping level (applied DC voltage). At high doping levels, the conductivity becomes approximately linear in carrier density—a behavior also observed in Fig. 4.2 for the quantum capacitance of graphene.

In Chapter 3, the finite conductivity of graphene was treated by approximating the cylindrical region as an infinitely large area, thereby reducing the problem to a one-dimensional (1D) formulation. As another possible extension of that chapter, this approximation could be relaxed to treat the system in full three dimensions (3D). Employing numerical techniques such as those presented in [108, 152, 153] would enable a more comprehensive analysis of geometrical effects and provide deeper insights into the interplay between finite conductivity and spatial confinement.

## • *Boundary Conditions and Interfacial Models in Ionic Liquids*

A comprehensive theory for ion dynamics in ionic liquids (ILs) remains elusive, primarily due to unresolved issues concerning the appropriate boundary conditions and modeling the electrode/IL interfaces.

The first pertains to the boundary conditions necessitated by the higher-order Poisson equation used to capture electrostatic correlations. In Chapter 5, we incorporated non-vanishing interfacial electrostatic correlations—derived from interfacial stress balance via the *Gibbs–Duhem* relation [63]—as a refinement of the original BSK model [45]. While this approach improves the linear theory near the interface, it breaks down in the nonlinear regime where ion finite-size effects become prominent. To address this, Gupta et al. [142] proposed a variational framework based on the *grand potential* formalism, which systematically accounts for electrostatic correlations, steric constraints, and large surface potentials. Their model introduces self-consistent boundary conditions involving higher-order derivatives of the electrostatic potential, thereby offering a more complete and physically grounded description of the electrode/electrolyte interface.

The second challenge involves time-dependent modeling of ILs at electrode surfaces. This difficulty arises from two unresolved issues: identifying the correct length scale that governs charging dynamics in ILs and independently determining the compactness parameter,  $\gamma$ , as revealed by time-resolved X-ray reflectivity (XRR) techniques [154]. For instance, the characteristic charging time proposed by Zhao [141],  $\tau_c = \lambda_D^{3/2} L / (DL_c^{1/2})$ , which we adopted in Chapter 5, and the computationally-deduced by Lee et al. [155],  $\tau_c = (L^2/D) (\lambda_D/L_c)^{3/2}$ , were shown to deviate from XRR measurements [156]. This discrepancy is partly due to the interfacial electrical impedance, which, in the presence of ILs, often exhibits constant phase element (CPE) behavior even on atomically smooth surfaces [65, 41, 154]. The CPE response complicates measurements and introduces *capacitance hysteresis*, characterized by a delayed response to applied potentials [154]. Such complexities have been examined by Gore et al. [157], who compared EIS with linear AC voltammetry, and by Lucio and Shaw using Fourier-transformed AC voltammetry (FT-ACV) [158, 159, 160].

To address these issues, a possible extension of Chapter 5 could involve developing a microscopic model for the CPE impedance at the graphene/electrolyte interface in ILs. Such a framework, based on anomalous diffusion and random walk theory [91], would provide insight into the physical origins of CPE behavior. Furthermore, the discussion could be extended to nonlinear regimes under large applied voltages, where  $\gamma$  is expected to play a central role and the interfacial capacitance may exhibit additional voltage dependence. This analysis could build on the methodology developed in Chapter 4.

### • *Interfacial Low-Frequency Noise*

Graphene has emerged as a promising platform for biochemical sensing applications, particularly in ion-sensitive field-effect transistors (GFETs), with diverse uses in chemistry and biomedicine. The low-frequency response of GFETs in liquid environments has been widely studied [161, 162]. For instance, extracellular voltage fluctuations associated with action potentials can induce measurable changes in the resistance of a GFET, making these devices suitable for neural recording applications. Additionally, the binding of charged biomolecules—such as proteins or DNA—can be detected by GFET biosensors, positioning them as strong candidates for next-generation biomarker assays [161]. The origin of low-frequency noise at the graphene/liquid interface is typically attributed to two main mechanisms: (i) adsorption and desorption events at the graphene sensing surface [163], which degrade sensor resolution, and/or (ii) trapping and de-trapping of charge carriers in the transistor’s insulating layer [164], which impairs electrical conduction [165]. Mechanism (i) is commonly modeled using the site-binding framework [163], while mechanism (ii) is described by a stochastic process known as the *random telegraph signal* (RTS) [162]. RTSs have been experimentally observed in carbon nanotubes and theoretically predicted in graphene nanoribbons, due to their sensitivity to a small number of fluctuators within a confined contact region [166, 167]. The dynamic interplay of these noise sources in graphene-based devices can give rise to a characteristic low-frequency noise known as  $1/f$  noise [168].

# References

- [1] Alexander J Pak, Eunsu Paek, and Gyeong S Hwang. Impact of graphene edges on enhancing the performance of electrochemical double layer capacitors. *The Journal of Physical Chemistry C*, 118(38):21770–21777, 2014.
- [2] Jin-Hui Zhong, Jun-Yang Liu, Qiongyu Li, Mian-Gang Li, Zhi-Cong Zeng, Shu Hu, De-Yin Wu, Weiwei Cai, and Bin Ren. Interfacial capacitance of graphene: Correlated differential capacitance and in situ electrochemical raman spectroscopy study. *Electrochimica Acta*, 110:754–761, 2013.
- [3] Cheng Zhan, Justin Neal, Jianzhong Wu, and De-en Jiang. Quantum effects on the capacitance of graphene-based electrodes. *The Journal of Physical Chemistry C*, 119(39):22297–22303, 2015.
- [4] Paula A Brooksby, Anna K Farquhar, Haidee M Dykstra, Mark R Waterland, and Alison J Downard. Quantum capacitance of aryldiazonium modified large area few-layer graphene electrodes. *The Journal of Physical Chemistry C*, 119(46):25778–25785, 2015.
- [5] Hend S Magar, Rabeay YA Hassan, and Ashok Mulchandani. Electrochemical impedance spectroscopy (eis): Principles, construction, and biosensing applications. *Sensors*, 21(19):6578, 2021.
- [6] Vincent Vivier and Mark E Orazem. Impedance analysis of electrochemical systems. *Chemical Reviews*, 122(12):11131–11168, 2022.
- [7] Maibam Birla Singh and Rama Kant. Debye–falkenhagen dynamics of electric double layer in presence of electrode heterogeneities. *Journal of Electroanalytical Chemistry*, 704:197–207, 2013.

- [8] Giovanni Barbero, F Batalioto, and Antônio Martins Figueiredo Neto. Theory of small-signal ac response of a dielectric liquid containing two groups of ions. *Applied Physics Letters*, 92(17), 2008.
- [9] Maibam Birla Singh and Rama Kant. Theory of anomalous dynamics of electric double layer at heterogeneous and rough electrodes. *The Journal of Physical Chemistry C*, 118(10):5122–5133, 2014.
- [10] Laís C Lopes, Adriano Santos, and Paulo R Bueno. Measuring quantum conductance and capacitance of graphene using impedance-derived capacitance spectroscopy. *Carbon*, 184:821–827, 2021.
- [11] Yuliana Pérez Sánchez, Adriano Santos, and Paulo Roberto Bueno. Quantum mechanical meaning of the charge transfer resistance. *The Journal of Physical Chemistry C*, 126(6):3151–3162, 2022.
- [12] James Ross Macdonald, William B Johnson, ID Raistrick, DR Franceschetti, Norbert Wagner, MCH McKubre, DD Macdonald, B Sayers, N Bonanos, BCH Steele, et al. *Impedance Spectroscopy: Theory, Experiment, and Applications*. John Wiley & Sons, 2018.
- [13] Mark E. Orazem and Bernard Tribollet. *Electrochemical Impedance Spectroscopy*. John Wiley & Sons, 2nd edition, 2007.
- [14] X Muñoz-Berbel, Cristina García-Aljaro, and FJ Muñoz. Impedimetric approach for monitoring the formation of biofilms on metallic surfaces and the subsequent application to the detection of bacteriophages. *Electrochimica Acta*, 53(19):5739–5744, 2008.
- [15] Sandra N Garcia, Leslie Gutierrez, and Amy McNulty. Real-time cellular analysis as a novel approach for in vitro cytotoxicity testing of medical device extracts. *Journal of Biomedical Materials Research Part A*, 101(7):2097–2106, 2013.
- [16] Jacobo Paredes, Sheila Becerro, and Sergio Arana. Label-free interdigitated micro-electrode based biosensors for bacterial biofilm growth monitoring using petri dishes. *Journal of Microbiological Methods*, 100:77–83, 2014.
- [17] Diana Gutiérrez, Claudio Hidalgo-Cantabrana, Ana Rodríguez, Pilar García, and Patricia Ruas-Madiedo. Monitoring in real time the formation and removal of biofilms from clinical related pathogens using an impedance-based technology. *PLoS ONE*, 11(10):e0163966, 2016.

- [18] Tien Anh-Nguyen, Bogdan Tiberius, Uwe Pliquet, and Gerald A Urban. An impedance biosensor for monitoring cancer cell attachment, spreading and drug-induced apoptosis. *Sensors and Actuators A: Physical*, 241:231–237, 2016.
- [19] Jozef BJH van Duuren, Mathias Müsken, Bianka Karge, Jürgen Tomasch, Christoph Wittmann, Susanne Häussler, and Mark Brönstrup. Use of single-frequency impedance spectroscopy to characterize the growth dynamics of biofilm formation in *Pseudomonas aeruginosa*. *Scientific Reports*, 7(1):5223, 2017.
- [20] Yikang Xu, Youss Dhaouadi, Paul Stoodley, and Dacheng Ren. Sensing the unreachable: challenges and opportunities in biofilm detection. *Current Opinion in Biotechnology*, 64:79–84, 2020.
- [21] Xiahua Wang, Aiping Liu, Yun Xing, Hongwei Duan, Weizhong Xu, Qi Zhou, Huaping Wu, Cen Chen, and Benyong Chen. Three-dimensional graphene biointerface with extremely high sensitivity to single cancer cell monitoring. *Biosensors and Bioelectronics*, 105:22–28, 2018.
- [22] Jin Song, Yiwei Li, Fang Yin, Zhitao Zhang, Dingkun Ke, Dianbing Wang, Qipeng Yuan, and Xian-En Zhang. Enhanced electrochemical impedance spectroscopy analysis of microbial biofilms on an electrochemically in situ generated graphene interface. *ACS sensors*, 5(6):1795–1803, 2020.
- [23] Yuyan Shao, Jun Wang, Hong Wu, Jun Liu, İlhan A Aksay, and Yuehe Lin. Graphene based electrochemical sensors and biosensors: a review. *Electroanalysis: An International Journal Devoted to Fundamental and Practical Aspects of Electroanalysis*, 22(10):1027–1036, 2010.
- [24] Lucyano JA Macedo, Rodrigo M Iost, Ayaz Hassan, Kannan Balasubramanian, and Frank N Crespilho. Bioelectronics and interfaces using monolayer graphene. *Chem-ElectroChem*, 6(1):31–59, 2019.
- [25] Juliana Cecchetto, Adriano Santos, Adriano Mondini, Eduardo M Cilli, and Paulo R Bueno. Serological point-of-care and label-free capacitive diagnosis of dengue virus infection. *Biosensors and Bioelectronics*, 151:111972, 2020.
- [26] Mary Grace Cassar, Cristiana Sebu, Michael Pidcock, Brian Andrews, and Shubham Chandak. Optimal design of concentric electrodes for functional electrical stimulation in multilayered isotropic tissues. In *2023 3rd International Conference on Electrical, Computer, Communications and Mechatronics Engineering (ICECCME)*, pages 1–11. IEEE, 2023.

- [27] Chaejeong Heo, Jeongwan Yoo, Siyoung Lee, Areum Jo, Susie Jung, Hyosun Yoo, Young Hee Lee, and Minah Suh. The control of neural cell-to-cell interactions through non-contact electrical field stimulation using graphene electrodes. *Biomaterials*, 32(1):19–27, 2011.
- [28] Boyu Xu, Jiahui Pei, Liefeng Feng, and Xiao-Dong Zhang. Graphene and graphene-related materials as brain electrodes. *Journal of Materials Chemistry B*, 9(46):9485–9496, 2021.
- [29] Lu Yan, Bingxin Zhao, Xiaohong Liu, Xuan Li, Chao Zeng, Haiyan Shi, Xiaoxue Xu, Tong Lin, Liming Dai, and Yong Liu. Aligned nanofibers from polypyrrole/graphene as electrodes for regeneration of optic nerve via electrical stimulation. *ACS Applied Materials & Interfaces*, 8(11):6834–6840, 2016.
- [30] Rohit L Vekariya. A review of ionic liquids: Applications towards catalytic organic transformations. *Journal of Molecular Liquids*, 227:44–60, 2017.
- [31] Usman Ali Rana, Maria Forsyth, Douglas R MacFarlane, and Jennifer M Pringle. Toward protic ionic liquid and organic ionic plastic crystal electrolytes for fuel cells. *Electrochimica Acta*, 84:213–222, 2012.
- [32] Hirofumi Nakamoto and Masayoshi Watanabe. Brønsted acid–base ionic liquids for fuel cell electrolytes. *Chemical Communications*, (24):2539–2541, 2007.
- [33] Catherine A Summers and Robert A Flowers. Protein renaturation by the liquid organic salt ethylammonium nitrate. *Protein Science*, 9(10):2001–2008, 2000.
- [34] Alberto Scalia, Alberto Varzi, Arianna Moretti, Peter Ruschhaupt, Andrea Lamberti, Elena Tresso, and Stefano Passerini. Electrolytes based on n-butyl-n-methylpyrrolidinium 4, 5-dicyano-2-(trifluoromethyl) imidazole for high voltage electrochemical double layer capacitors. *ChemElectroChem*, 6(2):552–557, 2019.
- [35] Alberto Scalia, Alberto Varzi, Andrea Lamberti, Elena Tresso, Sangsik Jeong, Timo Jacob, and Stefano Passerini. High energy and high voltage integrated photoelectrochemical double layer capacitor. *Sustainable Energy & Fuels*, 2(5):968–977, 2018.
- [36] Pietro Zaccagnini, Daniele di Giovanni, Manuel Gomez Gomez, Stefano Passerini, Alberto Varzi, and Andrea Lamberti. Flexible and high temperature supercapacitor based on laser-induced graphene electrodes and ionic liquid electrolyte, a de-rated voltage analysis. *Electrochimica Acta*, 357:136838, 2020.

- [37] Celine Largeot, Cristelle Portet, John Chmiola, Pierre-Louis Taberna, Yury Gogotsi, and Patrice Simon. Relation between the ion size and pore size for an electric double-layer capacitor. *Journal of the American Chemical Society*, 130(9):2730–2731, 2008.
- [38] P Tamailarasan and S Ramaprabhu. Carbon nanotubes-graphene-solidlike ionic liquid layer-based hybrid electrode material for high performance supercapacitor. *The Journal of Physical Chemistry C*, 116(27):14179–14187, 2012.
- [39] Chenguang Liu, Zhenning Yu, David Neff, Aruna Zhamu, and Bor Z Jang. Graphene-based supercapacitor with an ultrahigh energy density. *Nano letters*, 10(12):4863–4868, 2010.
- [40] Li Li Zhang and XS Zhao. Carbon-based materials as supercapacitor electrodes. *Chemical Society Reviews*, 38(9):2520–2531, 2009.
- [41] Svyatoslav Kondrat, Guang Feng, Fernando Bresme, Michael Urbakh, and Alexei A Kornyshev. Theory and simulations of ionic liquids in nanoconfinement. *Chemical Reviews*, 123(10):6668–6715, 2023.
- [42] Tamás Pajkossy, Claus Müller, and Timo Jacob. The metal–ionic liquid interface as characterized by impedance spectroscopy and in situ scanning tunneling microscopy. *Physical Chemistry Chemical Physics*, 20(33):21241–21250, 2018.
- [43] Chengbao Liu, Shihui Qiu, Peng Du, Haichao Zhao, and Liping Wang. An ionic liquid–graphene oxide hybrid nanomaterial: synthesis and anticorrosive applications. *Nanoscale*, 10(17):8115–8124, 2018.
- [44] Jianglin Ye, Yih-Chyng Wu, Kui Xu, Kun Ni, Na Shu, Pierre-Louis Taberna, Yanwu Zhu, and Patrice Simon. Charge storage mechanisms of single-layer graphene in ionic liquid. *Journal of the American Chemical Society*, 141(42):16559–16563, 2019.
- [45] Martin Z Bazant, Brian D Storey, and Alexei A Kornyshev. Double layer in ionic liquids: Overscreening versus crowding. *Physical review letters*, 106(4):046102, 2011.
- [46] Alexei A Kornyshev. Double-layer in ionic liquids: paradigm change? *The Journal of Physical Chemistry B*, 111(20):5545–5557, 2007.
- [47] Sylvio May. Differential capacitance of the electric double layer: mean-field modeling approaches. *Current Opinion in Electrochemistry*, 13:125–131, 2019.

- [48] Rachel Downing, Guilherme Volpe Bossa, and Sylvio May. The role of ion–ion correlations for the differential capacitance of ionic liquids. *The Journal of Physical Chemistry C*, 122(50):28537–28544, 2018.
- [49] Yun Sung Park and In Seok Kang. Perturbation analysis for the effects of ion correlations on the surface force and the specific capacitance in a nanochannel. *Colloids and Surfaces A: Physicochemical and Engineering Aspects*, 614:126207, 2021.
- [50] Carla S Perez-Martinez, Alexander M Smith, and Susan Perkin. Underscreening in concentrated electrolytes. *Faraday Discussions*, 199:239–259, 2017.
- [51] Mahdi Yavarian, Roderick Melnik, and Zoran L Mišković. Modeling of charging dynamics in electrochemical systems with a graphene electrode. *Journal of Electroanalytical Chemistry*, 946:117711, 2023.
- [52] P Sharma and Zoran. L. Mišković. Ionic screening of charged impurities in electrolytically gated graphene: A partially linearized poisson-boltzmann model. *The Journal of Chemical Physics*, 143(13):134118, 2015.
- [53] Allen J Bard, Larry R Faulkner, and Henry S White. *Electrochemical Methods: Fundamentals and Applications*. John Wiley & Sons, 2022.
- [54] Lindsey Daniels. *The Interactions of Graphene with Ionic Solutions and Their Effects on the Differential Capacitance for Sensing Applications*. PhD thesis, University of Waterloo, 2019.
- [55] Yan Levin. Electrostatic correlations: from plasma to biology. *Reports on Progress in Physics*, 65(11):1577, 2002.
- [56] A Yu Grosberg, TT Nguyen, and BI Shklovskii. Colloquium: The physics of charge inversion in chemical and biological systems. *Reviews of Modern Physics*, 74(2):329, 2002.
- [57] RJ-M Pellenq, JM Caillol, and A Delville. Electrostatic attraction between two charged surfaces: A (n, v, t) monte carlo simulation. *The Journal of Physical Chemistry B*, 101(42):8584–8594, 1997.
- [58] Rahul Prasanna Misra, J Pedro de Souza, Daniel Blankschtein, and Martin Z Bazant. Theory of surface forces in multivalent electrolytes. *Langmuir*, 35(35):11550–11565, 2019.

- [59] Christopher W Outhwaite and Lutful B Bhuiyan. An improved modified poisson–boltzmann equation in electric-double-layer theory. *Journal of the Chemical Society, Faraday Transactions 2: Molecular and Chemical Physics*, 79(5):707–718, 1983.
- [60] Marcelo Lozada-Cassou, Rafael Saavedra-Barrera, and Douglas Henderson. The application of the hypernetted chain approximation to the electrical double layer: Comparison with monte carlo results for symmetric salts. *The Journal of Chemical Physics*, 77(10):5150–5156, 1982.
- [61] Adelina Voukadinova, Mónica Valiskó, and Dirk Gillespie. Assessing the accuracy of three classical density functional theories of the electrical double layer. *Physical Review E*, 98(1):012116, 2018.
- [62] Roland Roth. Fundamental measure theory for hard-sphere mixtures: a review. *Journal of Physics: Condensed Matter*, 22(6):063102, 2010.
- [63] J Pedro de Souza and Martin Z Bazant. Continuum theory of electrostatic correlations at charged surfaces. *The Journal of Physical Chemistry C*, 124(21):11414–11421, 2020.
- [64] Martin Z Bazant, Mustafa Sabri Kilic, Brian D Storey, and Armand Ajdari. Towards an understanding of induced-charge electrokinetics at large applied voltages in concentrated solutions. *Advances in Colloid and Interface Science*, 152(1-2):48–88, 2009.
- [65] Maxim V Fedorov and Alexei A Kornyshev. Ionic liquids at electrified interfaces. *Chemical Reviews*, 114(5):2978–3036, 2014.
- [66] Jianzhong Wu. Understanding the electric double-layer structure, capacitance, and charging dynamics. *Chemical Reviews*, 122(12):10821–10859, 2022.
- [67] Dirk Gillespie, Wolfgang Nonner, and Robert S Eisenberg. Coupling poisson–nernst–planck and density functional theory to calculate ionflux. *Journal of Physics: Condensed Matter*, 14(46):12129, 2002.
- [68] Roland Roth and Dirk Gillespie. Shells of charge: a density functional theory for charged hard spheres. *Journal of Physics: Condensed Matter*, 28(24):244006, 2016.
- [69] Mark H Holmes. *Introduction to Perturbation Methods*, volume 20. Springer Science & Business Media, 2012. See Chapter 2.

- [70] Ali H Nayfeh. *Perturbation Methods*. John Wiley & Sons, 2024. See Chapter 4.
- [71] William Paulsen. *Asymptotic Analysis and Perturbation Theory*. CRC Press, 2013. See Chapter 7.
- [72] Alexandros Ch Lazanas and Mamas I Prodromidis. Electrochemical impedance spectroscopy— a tutorial. *ACS Measurement Science Au*, 3(3):162–193, 2023.
- [73] Paulo Roberto Bueno and David Alejandro Miranda Mercado. Quantum rate theory for graphene. *The Journal of Physical Chemistry C*, 126(36):15374–15385, 2022.
- [74] Laís Cristine Lopes, Edgar Fabian Pinzón, Gabriela Dias-da Silva, Gustavo Troiano Feliciano, and Paulo Roberto Bueno. Electrochemical measurement of the electronic structure of graphene via quantum mechanical rate spectroscopy. *Electrochimica Acta*, 480:143837, 2024.
- [75] Paulo Roberto Bueno. Quantum rate theory and electron-transfer dynamics: A theoretical and experimental approach for quantum electrochemistry. *Electrochimica Acta*, 466:142950, 2023.
- [76] Bing-Ang Mei, Obaidallah Munteshari, Jonathan Lau, Bruce Dunn, and Laurent Pilon. Physical interpretations of nyquist plots for edlc electrodes and devices. *The Journal of Physical Chemistry C*, 122(1):194–206, 2018.
- [77] Alvaro Ochoa-Calle, Alfredo Guevara-García, Jorge Vazquez-Arenas, Ignacio González, and Marcelo Galván. Establishing the relationship between quantum capacitance and softness of n-doped graphene/electrolyte interfaces within the density functional theory grand canonical Kohn–Sham formalism. *The Journal of Physical Chemistry A*, 124(3):573–581, 2019.
- [78] Juhyun Song, Edwin Khoo, and Martin Z Bazant. Electrochemical impedance of electrodiffusion in charged medium under dc bias. *Physical Review E*, 100(4):042204, 2019.
- [79] AL Alexe-Ionescu, G Barbero, LR Evangelista, and EK Lenzi. Current–voltage characteristics and impedance spectroscopy: Surface conduction and adsorption–desorption effects in electrolytic cells. *The Journal of Physical Chemistry C*, 124(5):3150–3158, 2020.
- [80] AL Alexe-Ionescu, G Barbero, and LR Evangelista. Electric response of asymmetric electrolytic cells to small ac signals. *Journal of Electroanalytical Chemistry*, 873:114378, 2020.

- [81] Christophe Berthod, Haijing Zhang, Alberto F Morpurgo, and Thierry Giamarchi. Theory of cross quantum capacitance. *Physical Review Research*, 3(4):043036, 2021.
- [82] Brandon C Wood, Tadashi Ogitsu, Minoru Otani, and Juergen Biener. First-principles-inspired design strategies for graphene-based supercapacitor electrodes. *The Journal of Physical Chemistry C*, 118(1):4–15, 2014.
- [83] Cheng Zhan, Cheng Lian, Yu Zhang, Matthew W Thompson, Yu Xie, Jianzhong Wu, Paul RC Kent, Peter T Cummings, De-en Jiang, and David J Wesolowski. Computational insights into materials and interfaces for capacitive energy storage. *Advanced Science*, 4(7):1700059, 2017.
- [84] Sujay B Desai, Hossain M Fahad, Theodor Lundberg, Gregory Pitner, Hyungjin Kim, Daryl Chrzan, H-S Philip Wong, and Ali Javey. Gate quantum capacitance effects in nanoscale transistors. *Nano letters*, 19(10):7130–7137, 2019.
- [85] Q Xu, GM Yang, and WT Zheng. Dft calculation for stability and quantum capacitance of mos2 monolayer-based electrode materials. *Materials Today Communications*, 22:100772, 2020.
- [86] G Barbero and AL Alexe-Ionescu. Role of the diffuse layer of the ionic charge on the impedance spectroscopy of a cell of liquid. *Liquid Crystals*, 32(7):943–949, 2005.
- [87] Jacob N Israelachvili. *Intermolecular and Surface Forces*. Academic Press, 2011.
- [88] Anil Koklu, Vladimir Ajaev, and Ali Beskok. Self-similar response of electrode polarization for binary electrolytes in parallel plate capacitor systems. *Analytical chemistry*, 91(17):11231–11239, 2019.
- [89] Alexandria RC Bredar, Amanda L Chown, Andricus R Burton, and Byron H Farnum. Electrochemical impedance spectroscopy of metal oxide electrodes for energy applications. *ACS Applied Energy Materials*, 3(1):66–98, 2020.
- [90] Paul MS Monk. *Fundamentals of Electroanalytical Chemistry*. John Wiley & Sons, 2008.
- [91] J Ross Macdonald and Evgenij Barsoukov. *Impedance Spectroscopy: Theory, Experiment, and Applications*. John Wiley & Sons, 2018.
- [92] GAKPA Giovannetti, Petr A Khomyakov, Geert Brocks, VM vd Karpan, Jeroen van den Brink, and Paul J Kelly. Doping graphene with metal contacts. *Physical Review Letters*, 101(2):026803, 2008.

- [93] Simon Drieschner, Anton Guimerà, Ramon G Cortadella, Damià Viana, Evangelos Makrygiannis, Benno M Blaschke, Josua Vieten, and Jose A Garrido. Frequency response of electrolyte-gated graphene electrodes and transistors. *Journal of Physics D: Applied Physics*, 50(9):095304, 2017.
- [94] AL Efros. Negative density of states: Screening, einstein relation, and negative diffusion. *Physical Review B—Condensed Matter and Materials Physics*, 78(15):155130, 2008.
- [95] Eugene B Kolomeisky and Joseph P Straley. Relaxation of charge in monolayer graphene: Fast nonlinear diffusion versus coulomb effects. *Physical Review B*, 95(4):045415, 2017.
- [96] S Das Sarma, A Shaffique, E H Hwang, and E Rossi. Electronic transport in two-dimensional graphene. *Reviews of Modern Physics*, 83:407, 2011.
- [97] S Das Sarma and EH Hwang. Density-dependent electrical conductivity in suspended graphene: Approaching the dirac point in transport. *Physical Review B—Condensed Matter and Materials Physics*, 87(3):035415, 2013.
- [98] Kirill I Bolotin, Kenneth J Sikes, J Hone, HL Stormer, and Ph Kim. Temperature-dependent transport in suspended graphene. *Physical Review Letters*, 101(9):096802, 2008.
- [99] Alexander S Mayorov, Daniel C Elias, Ivan S Mukhin, Sergey V Morozov, Leonid A Ponomarenko, Kostya S Novoselov, AK Geim, and Roman V Gorbachev. How close can one approach the dirac point in graphene experimentally? *Nano letters*, 12(9):4629–4634, 2012.
- [100] Bo Fu, Yanru Chen, Weiwei Chen, Wei Zhu, Ping Cui, Qunxiang Li, Zhenyu Zhang, and Qinwei Shi. Disorder effects on the quasiparticle and transport properties of two-dimensional dirac fermionic systems. *Physical Review B*, 108(6):064207, 2023.
- [101] Milton Abramowitz and Irene A Stegun. *Handbook of Mathematical Functions with Formulas, Graphs, and Mathematical Tables*, volume 55. US Government printing office, 1968. , §9.6.1.
- [102] PA Khomyakov, AA Starikov, Geert Brocks, and Paul J Kelly. Nonlinear screening of charges induced in graphene by metal contacts. *Physical Review B—Condensed Matter and Materials Physics*, 82(11):115437, 2010.

- [103] John D Wiley. Cv profiling of gaas fet films. *IEEE Transactions on Electron Devices*, 25(11):1317–1324, 1978.
- [104] G Barbero and Ioannis Lelidis. Analysis of warburg’s impedance and its equivalent electric circuits. *Physical Chemistry Chemical Physics*, 19(36):24934–24944, 2017.
- [105] ZL Mišković and Nitin Upadhyaya. Modeling electrolytically top-gated graphene. *Nanoscale Research Letters*, 5:505–511, 2010.
- [106] Lindsey Daniels, Matthew Scott, and Zoran L Mišković. The effects of dielectric decrement and finite ion size on differential capacitance of electrolytically gated graphene. *Chemical Physics Letters*, 701:43–51, 2018.
- [107] Masayuki Itagaki, Satoshi Suzuki, Isao Shitanda, and Kunihiro Watanabe. Electrochemical impedance and complex capacitance to interpret electrochemical capacitor. *Electrochemistry*, 75(8):649–655, 2007.
- [108] Kenneth K Yamamoto, Anil Koklu, Ali Beskok, and Vladimir S Ajaev. Polarization of disk electrodes in high-conductivity electrolyte solutions. *The Journal of Chemical Physics*, 160(5), 2024.
- [109] Gaurav Kumar Mishra and Rama Kant. Modular theory for dc-biased electrochemical impedance response of supercapacitor. *Journal of Power Sources*, 473:228467, 2020.
- [110] R. Bracewell. *The Fourier Transform and Its Applications*. McGraw-Hill, 3rd edition, 1999.
- [111] Lokenath Debnath and Dambaru Bhatta. *Integral transforms and their applications*. Chapman and Hall/CRC, 2016.
- [112] Mahdi Yavarian, Roderick Melnik, and Zoran L Mišković. Frequency response of the diffuse-charge dynamics in electrochemical systems with a graphene electrode. *Journal of The Electrochemical Society*, 171(8):086501, 2024.
- [113] Jilin Xia, Fang Chen, Jinghong Li, and Nongjian Tao. Measurement of the quantum capacitance of graphene. *Nature nanotechnology*, 4(8):505–509, 2009.
- [114] Andrea C Ferrari, Jannik C Meyer, Vittorio Scardaci, Cinzia Casiraghi, Michele Lazzeri, Francesco Mauri, Stefano Piscanec, Dingde Jiang, Konstantin Sergeevich Novoselov, Siegmur Roth, et al. Raman spectrum of graphene and graphene layers. *Physical Review Letters*, 97(18):187401, 2006.

- [115] Bart Partoens and FM Peeters. From graphene to graphite: Electronic structure around the k point. *Physical Review B—Condensed Matter and Materials Physics*, 74(7):075404, 2006.
- [116] Cheng Zhan and De-en Jiang. Contribution of dielectric screening to the total capacitance of few-layer graphene electrodes. *The Journal of Physical Chemistry Letters*, 7(5):789–794, 2016.
- [117] Jiho Kim, Jiwon Jeon, Byoungju Lee, Kwangnam Yu, Marcelo A Kuroda, and EJ Choi. Infrared spectroscopic probe of charge distribution in gated multilayer graphene: evidence of nonlinear screening. *Physical Review Applied*, 13(1):014066, 2020.
- [118] Milton Abramowitz and Irene A Stegun. *Handbook of Mathematical Functions with Formulas, Graphs, and Mathematical Tables*, volume 55. US Government printing office, 1968. pp. 1004-1005.
- [119] Rama Kant, Jasmin Kaur, and Gaurav Kumar Mishra. Theory for influence of the metal electrolyte interface on heterogeneous electron transfer rate constant: fractional electron transferred transition state approach. *The Journal of Physical Chemistry C*, 124(4):2273–2288, 2020.
- [120] Antoine Bonnefont, Françoise Argoul, and Martin Z Bazant. Analysis of diffuse-layer effects on time-dependent interfacial kinetics. *Journal of Electroanalytical Chemistry*, 500(1-2):52–61, 2001.
- [121] Ahmed Shalabi, Lindsey Daniels, Matthew Scott, and ZL Mišković. Differential capacitance of ionic liquid interface with graphene: The effects of correlation and finite size of ions. *Electrochimica Acta*, 319:423–434, 2019.
- [122] Martin Z Bazant, Katsuyo Thornton, and Armand Ajdari. Diffuse-charge dynamics in electrochemical systems. *Physical review E*, 70(2):021506, 2004.
- [123] Bhavya Balu and Aditya S Khair. The electrochemical impedance spectrum of asymmetric electrolytes across low to moderate frequencies. *Journal of Electroanalytical Chemistry*, 911:116222, 2022.
- [124] Bhavya Balu and Aditya S Khair. A thin double layer analysis of asymmetric rectified electric fields (arefs). *Journal of Engineering Mathematics*, 129(1):4, 2021.

- [125] Kevin T Chu and Martin Z Bazant. Electrochemical thin films at and above the classical limiting current. *SIAM Journal on Applied Mathematics*, 65(5):1485–1505, 2005.
- [126] Nathan Jarvey, Filipe Henrique, and Ankur Gupta. Ion transport in an electrochemical cell: a theoretical framework to couple dynamics of double layers and redox reactions for multicomponent electrolyte solutions. *Journal of The Electrochemical Society*, 169(9):093506, 2022.
- [127] Andrei D Polyanin and Valentin F Zaitsev. *Handbook of Ordinary Differential Equations: Exact Solutions, Methods, and Problems*. Chapman and Hall/CRC, 2017.
- [128] Xiaowei Du, Hui Guo, Yan Jin, Qinghui Jin, and Jianlong Zhao. Electrochemistry investigation on the graphene/electrolyte interface. *Electroanalysis*, 27(12):2760–2765, 2015.
- [129] Christoph Slouka, David J Wurm, Georg Brunauer, Andreas Welzl-Wachter, Oliver Spadiut, Jürgen Fleig, and Christoph Herwig. A novel application for low frequency electrochemical impedance spectroscopy as an online process monitoring tool for viable cell concentrations. *Sensors*, 16(11):1900, 2016.
- [130] Hongmei Li, Kenneth B Walsh, Ferhat Bayram, and Goutam Koley. Direct measurement of  $k^+$  ion efflux from neuronal cells using a graphene-based ion sensitive field effect transistor. *RSC advances*, 10(62):37728–37734, 2020.
- [131] Sang-Chan Park, Hee June Jeong, Min Heo, Jae Ho Shin, and Jae-Hyuk Ahn. Carbon nanotube-based ion-sensitive field-effect transistors with an on-chip reference electrode toward wearable sodium sensing. *ACS Applied Electronic Materials*, 3(6):2580–2588, 2021.
- [132] Naif H Al-Hardan, Muhammad Azmi Abdul Hamid, Mohd Firdaus-Raih, Azman Jalar, Ain Zafirah Kamaruddin, Lim Kar Keng, Ensaf Mohammed AL-Khalqi, and Naser M Ahmed. Titanium dioxide ion-sensitive extended gate field effect transistor (isegfet): selective detection of potassium ions in artificial blood serum. *Journal of Materials Science: Materials in Electronics*, 35(5):1–16, 2024.
- [133] Lei Dai, Lichao Ma, Wei Meng, Yuehua Li, Zhangxing He, and Ling Wang. Impedancemetric  $no_2$  sensor based on pd doped perovskite oxide sensing electrode conjunction with phase angle response. *Electrochimica Acta*, 265:411–418, 2018.

- [134] Nabamita Pal, Gaurab Dutta, Khawlah Kharashi, and Erica P Murray. Investigation of an impedimetric lasrmno3-au/y2o3-zro2-al2o3 composite nox sensor. *Materials*, 15(3):1165, 2022.
- [135] Mahdi Yavarian, Roderick Melnik, and ZL Mišković. Impact of electrostatic correlations on the frequency response of a graphene electrode in ionic liquid. *Physical Review E*, 111(5):055503, 2025.
- [136] Robert F Stout and Aditya S Khair. A continuum approach to predicting electrophoretic mobility reversals. *Journal of Fluid Mechanics*, 752:R1, 2014.
- [137] Jinn-Liang Liu and Bob Eisenberg. Correlated ions in a calcium channel model: a poisson–fermi theory. *The Journal of Physical Chemistry B*, 117(40):12051–12058, 2013.
- [138] Jinn-Liang Liu and Bob Eisenberg. Numerical methods for a poisson-nernst-planck-fermi model of biological ion channels. *Physical Review E*, 92(1):012711, 2015.
- [139] Jinn-Liang Liu and Bob Eisenberg. Analytical models of calcium binding in a calcium channel. *The Journal of Chemical Physics*, 141(7), 2014.
- [140] Jinn-Liang Liu and Bob Eisenberg. Poisson-nernst-planck-fermi theory for modeling biological ion channels. *The Journal of Chemical Physics*, 141(22), 2014.
- [141] Hui Zhao. Diffuse-charge dynamics of ionic liquids in electrochemical systems. *Physical Review E—Statistical, Nonlinear, and Soft Matter Physics*, 84(5):051504, 2011.
- [142] Ankur Gupta, Ananth Govind Rajan, Emily A Carter, and Howard A Stone. Thermodynamics of electrical double layers with electrostatic correlations. *The Journal of Physical Chemistry C*, 124(49):26830–26842, 2020.
- [143] Sven Schlumpberger and Martin Z Bazant. Simple theory of ionic activity in concentrated electrolytes. *arXiv preprint arXiv:1709.03106*, 2017.
- [144] Brian D Storey and Martin Z Bazant. Effects of electrostatic correlations on electrokinetic phenomena. *Physical Review E—Statistical, Nonlinear, and Soft Matter Physics*, 86(5):056303, 2012.
- [145] J Pedro de Souza, Zachary AH Goodwin, Michael McEldrew, Alexei A Kornyshev, and Martin Z Bazant. Interfacial layering in the electric double layer of ionic liquids. *Physical Review Letters*, 125(11):116001, 2020.

- [146] We note that Eq.(49), with  $\gamma_1$  and  $\gamma_2$  defined in Eq.(40), is a continuous function of  $\delta_c$ , but exhibits singularities at the values  $\delta_c = 0$  and  $\delta_c = 0.5$ , which are analytically removable in the sense of the L'Hôpital's rule, but cannot be handled by our numerical code. Given that we verified that the potential in Eq.(49) is a smooth function of  $\delta_c$ , we adopted the values 0.001 and 0.499 to represent the cases of  $\delta_c = 0$  and  $\delta_c = 0.5$ , respectively. In this way, we avoid the singular points in Eq.(49) while giving accurate enough results.
- [147] Ankur Gupta and Howard A Stone. Electrical double layers: effects of asymmetry in electrolyte valence on steric effects, dielectric decrement, and ion-ion correlations. *Langmuir*, 34(40):11971–11985, 2018.
- [148] Ankur Gupta, Ananth Govind Rajan, Emily A Carter, and Howard A Stone. Ionic layering and overcharging in electrical double layers in a poisson-boltzmann model. *Physical Review Letters*, 125(18):188004, 2020.
- [149] AA Moya. Low-frequency impedance and harmonic analysis in electrochemical cells with asymmetric contacts. *Journal of The Electrochemical Society*, 163(9):H768, 2016.
- [150] Wei Lai and Sossina M Haile. Impedance spectroscopy as a tool for chemical and electrochemical analysis of mixed conductors: a case study of ceria. *Journal of the American Ceramic Society*, 88(11):2979–2997, 2005.
- [151] AA Moya. Electrochemical impedance of ion-exchange membranes with interfacial charge transfer resistances. *The Journal of Physical Chemistry C*, 120(12):6543–6552, 2016.
- [152] Yawar Abbas, Laura van Smeden, Alwin RM Verschueren, Marcel AG Zevenbergen, and Jos FM Oudenhoven. Modeling electrochemical impedance spectroscopy using time-dependent finite element method. *Sensors*, 24(22):7264, 2024.
- [153] Vitor Maló Machado, João Pereira Fernandes, Maria Eduarda Pedro, and José Brandão Faria. Numerical evaluation of the frequency-dependent impedance of hemispherical ground electrodes through finite element analysis. *Energies*, 17(2):452, 2024.
- [154] Oguz Kagan Coskun, Miguel Muñoz, Saudagar Dongare, William Dean, and Burcu E Gurkan. Understanding the electrode-electrolyte interfaces of ionic liquids and deep eutectic solvents. *Langmuir*, 40(7):3283–3300, 2024.

- [155] Alpha A Lee, Svyatoslav Kondrat, Dominic Vella, and Alain Goriely. Dynamics of ion transport in ionic liquids. *Physical Review Letters*, 115(10):106101, 2015.
- [156] Miaoqi Chu, Mitchell Miller, Travis Douglas, and Pulak Dutta. Ultraslow dynamics at a charged silicon–ionic liquid interface revealed by x-ray reflectivity. *The Journal of Physical Chemistry C*, 121(7):3841–3845, 2017.
- [157] Tyler R Gore, Toby Bond, Wenbin Zhang, Robert WJ Scott, and Ian J Burgess. Hysteresis in the measurement of double-layer capacitance at the gold–ionic liquid interface. *Electrochemistry Communications*, 12(10):1340–1343, 2010.
- [158] Anthony J Lucio and Scott K Shaw. Effects and controls of capacitive hysteresis in ionic liquid electrochemical measurements. *Analyst*, 143(20):4887–4900, 2018.
- [159] Anthony J Lucio, Scott K Shaw, Jie Zhang, and Alan M Bond. Large-amplitude fourier-transformed ac voltammetric study of the capacitive electrochemical behavior of the 1-butyl-3-methylimidazolium tetrafluoroborate–polycrystalline gold electrode interface. *The Journal of Physical Chemistry C*, 121(22):12136–12147, 2017.
- [160] Anthony J Lucio, Scott K Shaw, Jie Zhang, and Alan M Bond. Double-layer capacitance at ionic liquid–boron-doped diamond electrode interfaces studied by fourier transformed alternating current voltammetry. *The Journal of Physical Chemistry C*, 122(22):11777–11788, 2018.
- [161] Michael S Crosser, Morgan A Brown, Paul L McEuen, and Ethan D Minot. Determination of the thermal noise limit of graphene biotransistors. *Nano Letters*, 15(8):5404–5407, 2015.
- [162] Paweł Puczkarski, Qingqing Wu, Hatef Sadeghi, Songjun Hou, Amin Karimi, Yuewen Sheng, Jamie H Warner, Colin J Lambert, G Andrew D Briggs, and Jan A Mol. Low-frequency noise in graphene tunnel junctions. *ACS Nano*, 12(9):9451–9460, 2018.
- [163] Da Zhang, Paul Solomon, Shi-Li Zhang, and Zhen Zhang. Correlation of low-frequency noise to the dynamic properties of the sensing surface in electrolytes. *ACS Sensors*, 2(8):1160–1166, 2017.
- [164] Francesco MD Pellegrino, Giuseppe Falci, and Elisabetta Paladino. Charge carrier density noise in graphene: effect of localized/delocalized traps. *Journal of Statistical Mechanics: Theory and Experiment*, 2019(9):094015, 2019.

- [165] Phaedon Avouris and Fengnian Xia. Graphene applications in electronics and photonics. *Mrs Bulletin*, 37(12):1225–1234, 2012.
- [166] Guangyu Xu, Yuegang Zhang, Xiangfeng Duan, Alexander A Balandin, and Kang L Wang. Variability effects in graphene: Challenges and opportunities for device engineering and applications. *Proceedings of the IEEE*, 101(7):1670–1688, 2013.
- [167] Fei Liu, Mingqiang Bao, Hyung-jun Kim, Kang L Wang, Chao Li, Xiaolei Liu, and Chongwu Zhou. Giant random telegraph signals in the carbon nanotubes as a single defect probe. *Applied Physics Letters*, 86(16):163102, 2005.
- [168] Alexander A Balandin. Low-frequency 1/f noise in graphene devices. *Nature Nanotechnology*, 8(8):549–555, 2013.